
Site U1353¹

Expedition 317 Scientists²

Chapter contents

Background and objectives	1
Operations	2
Lithostratigraphy	3
Biostratigraphy	10
Paleomagnetism	14
Physical properties	16
Geochemistry and microbiology	19
Heat flow	22
Downhole logging	23
Stratigraphic correlation	25
References	26
Figures	27
Tables	82

Background and objectives

Hole U1353A

Position: 44°46.1079'S, 171°40.4368'E
Start hole: 0230 h, 22 December 2009
End hole: 1115 h, 22 December 2009
Time on hole (d): 0.36
Seafloor (drill pipe measurement from rig floor, m DRF): 95.5
(APC mudline)
Distance between rig floor and sea level (m): 11.3
Water depth (drill pipe measurement from sea level, m): 84.2
Total depth (drill pipe measurement from rig floor, m DRF):
151.5
Total penetration (m DSF): 56.0
Total length of cored section (m): 56.0
Total core recovered (m): 56.38
Core recovery (%): 101
Total number of cores: 8

Hole U1353B

Position: 44°46.1203'S, 171°40.4407'E
Start hole: 1115 h, 22 December 2009
End hole: 2050 h, 26 December 2009
Time on hole (d): 4.40
Seafloor (drill pipe measurement from rig floor, m DRF): 96.0
(APC mudline)
Distance between rig floor and sea level (m): 11.3
Water depth (drill pipe measurement from sea level, m): 84.7
Total depth (drill pipe measurement from rig floor, m DRF):
710.3
Total penetration (m DSF): 614.3
Total length of cored section (m): 614.3
Total core recovered (m): 211.48
Core recovery (%): 34
Total number of cores: 98

Hole U1353C

Position: 44°46.0982'S, 171°40.4380'E
Start hole: 2050 h, 26 December 2009
End hole: 2100 h, 28 December 2009
Time on hole (d): 2.01

¹Expedition 317 Scientists, 2011. Site U1353. In Fulthorpe, C.S., Hoyanagi, K., Blum, P., and the Expedition 317 Scientists, *Proc. IODP, 317*: Tokyo (Integrated Ocean Drilling Program Management International, Inc.).

doi:10.2204/iodp.proc.317.105.2011

²Expedition 317 Scientists' addresses.



Seafloor (drill pipe measurement from rig floor, m DRF): 96.0 (by proxy, Hole U1353B)
 Distance between rig floor and sea level (m): 11.3
 Water depth (drill pipe measurement from sea level, m): 84.7
 Total depth (drill pipe measurement from rig floor, m DRF): 625.0
 Total penetration (m DSF): 529.0
 Total length of cored section (m): 0
 Total core recovered (m): 0
 Core recovery (%): 0
 Total number of cores: 0

Integrated Ocean Drilling Program (IODP) Site U1353 (proposed Site CB-01A) is located on the middle shelf (85 m water depth) within the Canterbury Bight and is the most landward shelf site of the Canterbury Basin drilling transect. Site U1353 is located on dip seismic Profile EW00-01-66 and crossing strike Profile EW00-01-01 (Figs. [F1](#), [F2](#))

The philosophy behind the transect approach is discussed in “[Background and objectives](#)” in the “Site U1351” chapter. Site U1353 was considered the most challenging site, both because the water depth at this site was the shallowest of all Expedition 317 sites and also because the lithologies at this inboard setting were expected to be the coarsest grained. Site U1353 was therefore drilled, in accordance with the proposed drilling strategy, after the drillers had gained experience in shallow-water (122 m) drilling at Site U1351 and at slope Site U1352.

Site U1353 penetrates a middle Miocene to Holocene section containing seismic sequence boundaries U5–U19 (Lu and Fulthorpe, 2004). All sequence boundaries were penetrated landward of their rollovers or paleoshelf edges with the goal of recovering proximal facies, yielding evidence of shallow-water deposition, and providing optimal paleowater depths from benthic foraminiferal biofacies.

The principal objectives at Site U1353 were

1. To sample facies landward of rollovers of progradational seismic sequence boundaries U5–U19 and in particular to use benthic foraminiferal biofacies to estimate paleowater depths both above and below sequence boundaries in order to calculate eustatic amplitudes using two-dimensional backstripping; and
2. To investigate the facies, paleoenvironments, and depositional processes associated with the sequence stratigraphic model in a proximal setting on a prograding continental margin where sequence architecture is well constrained by seismic imaging.

Operations

Transit to Site U1353

After an 18 nmi transit from Site U1352, the R/V *JOIDES Resolution* was positioned over Site U1353 at 2320 h (all times are ship local time, Universal Time Coordinated [UTC] + 13 h) on 21 December 2009. At 2346 h, the positioning beacon (FSI BAP-547W, SN 1025, 14.0 kHz, 200 dB) was deployed. The position reference was a combination of Global Positioning System (GPS) and an acoustic beacon on the seafloor, weighted heavily toward the acoustic beacon (80%).

Site U1353 overview

Three holes were cored or drilled at Site U1353 (Table [T1](#)). The first hole was cored with the advanced piston corer (APC) system to 56 m drilling depth below seafloor (DSF) to provide sufficient samples for microbiology, chemistry, and geotechnical studies. The second hole was cored with the APC/extended core barrel (XCB) systems to the target depth of 614 m DSF. The third hole was drilled as a dedicated logging hole to 529 m DSF with a center bit installed in the APC/XCB bottom-hole assembly (BHA).

At 84.2 m water depth, Hole U1353A is the shallowest hole drilled for science by the *JOIDES Resolution*. The only holes cored in shallower water by the *JOIDES Resolution* were located in the Eniwetok Lagoon during Ocean Drilling Program (ODP) Leg 143. Holes 870A and 870B were cored to 48.7 and 49.8 m DSF, respectively, with a total recovery for both holes of 0.6 m. Both holes were drilled to test the dynamic positioning (DP) system and were not drilled for scientific objectives.

Core recovery at Site U1353 was 100% for the APC system and 5% for the XCB system. The total cored interval for Site U1353 was 670.3 m, with 267.86 m (40%) of recovered core samples.

Hole U1353A

Rig floor operations commenced at 2320 h on 21 December when the vessel shifted to auto-DP control. The BHA was made up with an APC/XCB bit, and operations in Hole U1353A began at 0230 h on 22 December with the establishment of the mudline at 91.5 m drilling depth below rig floor (DRF; 84.2 meters below sea level [mbsl]). APC coring continued through Core 317-U1353A-8H to 56.0 m DSF using nonmagnetic coring assemblies. Orientation was taken on the first six cores. The third-generation advanced piston corer temperature tool (APCT-3) was deployed once (Core 317-U1353A-5H) without success. The type of formation encountered proved too

difficult for our temperature measurement tools. Contamination testing was done on all cores with microspheres. Overall recovery for Hole U1353A was 56.38 m over an interval of 56 m (101%). The drill string was pulled back to the seafloor, and the bit cleared the seabed at 1115 h on 22 December.

Hole U1353B

The vessel was offset 20 m south of Hole U1353A, and coring in Hole U1353B began at 1115 h on 22 December. Hole U1353B was piston cored to 80.2 m DSF, with a total recovery of 80.74 m (101%). Because of the rough piston coring conditions noted in Hole U1353A, orientation and temperature measurement tools were not deployed in this hole. In an effort to maximize recovery and make progress in the hole, the XCB coring system was deployed intermittently from Cores 317-U1353B-14X through 60H (80.2–257.7 m DSF). In this interval, 69.7 m was cored in 9 XCB deployments, recovering 2.53 m of core (4%), and 107.8 m was cored in 38 APC deployments, recovering 107.6 m (100%). The superior recovery with the APC was not without penalty. Almost all of the piston cores were partial strokes (average = 3.7 m). Because the bit was advanced by recovery, the rate of penetration was very slow. Many cores had shattered core liners, and piston seals and core catchers were damaged. In addition, the recovered material included a large amount (>50%) of reworked or caved material.

Below 257.7 m DSF, Cores 317-U1353B-61X through 98X were taken to a total depth of 614.3 m DSF, recovering 20.55 m (6%).

The drill string was tripped back to 250 m DRF, and a 12 bbl, 14 ppg cement plug was pumped according to IODP policies for drilling on a continental shelf. The drill string was tripped back to just above the seafloor, and the bit cleared the seafloor at 2050 h on 26 December, ending Hole U1353B. A total of 211.48 m of core was recovered over an interval of 614.3 m (average recovery of 34%).

Hole U1353C

The ship was offset 20 m north of Hole U1353A, and drilling in Hole U1353C, a dedicated logging hole, began at 2050 h on 26 December. The hole was drilled to 626 m DSF, swept clean with a 50 bbl high-viscosity mud sweep, and displaced with 300 bbl of high-viscosity 10.5 ppg mud. The drill string was tripped out of the hole to 202 m DRF. The triple combination (triple combo) logging tool string was rigged up without nuclear sources (neutron porosity and gamma ray density) to minimize operational

risk. The tool string was run into the hole, tagging the bottom at 621 m wireline log depth below rig floor (WRF); the hole was logged up from there. The logging string was pulled to the surface and rigged down, and the Formation MicroScanner (FMS)-sonic tool string was assembled and run into the hole to 343 m WRF, where an obstruction was encountered. The hole was logged up from 343 m WRF. A second attempt was made to run down with the FMS-sonic tool string, but the tool string was only able to reach ~300 m WRF. Hole conditions while the tool was logged upward continued to deteriorate until the hole collapsed completely below 202 m WRF. The drillers worked to free both the drill string and the logging string, and eventually the logging string partially reentered the drill string. The drill string and the logging line were pulled up onto the rig floor using T-bars from ~200 m DRF. Hole U1353C could not be cemented with the logging tools stuck in the drill string, and the hole completely collapsed as the BHA was pulled clear of the hole, making it impossible to cement. The logging tools were rigged down on the rig floor. The BHA was broken down and secured at 2100 h on 28 December, ending Hole U1353C and operations at Site U1353.

Lithostratigraphy

Site U1353 is located landward of the last glacial low-stand shoreline, ~20 km inboard of Site U1351. Three holes were drilled at this site to a total depth of 605 m core depth below seafloor (CSF-A; unless otherwise noted, all depths in this section are reported in m CSF-A). Holes U1353A and U1353B were drilled to 56 and 614 m, respectively, and designated logging Hole U1353C was drilled to 529 m. This location allowed for sampling shelf sediments of Holocene–Miocene age. The described succession was divided into two lithologic units.

Core recovery varied at Site U1353 as a function of drilling technique and lithology. Core recovery of Unit I in Hole U1353A averaged 101%. Core recovery in Hole U1353B was 78% for Unit I and 42% for Unit II using a combination of APC and XCB coring methods. Overall core recovery was 40%. These rates are deceptively high because a majority of the recovered sediment was downhole contamination (cave-in and flow-in; see below). Core recovery dropped considerably below Core 317-U1353B-60H when the XCB was deployed.

The description of Unit I is based on Holes U1353A and U1353B. Hole U1353A was sampled for whole-round geochemical and geotechnical analyses, but most of the core was available for sedimentologic de-

scription. The two holes are offset ~20 m from each other (Fig. F3). Throughout the uppermost 56 m they exhibit similar lithologies (Fig. F4) but slightly different stratigraphies. This observation emphasizes the fact that the shelf environment drilled at Site U1353 is dynamic and exhibits localized spatial variability in sediment deposition and preservation.

Cores recovered from Holes U1353A and U1353B show a downhole transition from a heterolithic upper section with abrupt contacts (Unit I) to a more featureless sedimentary mud-dominated section with depth (Unit II). These changes suggest progressive but gradual changes in sedimentary styles as the margin evolved (Figs. F5, F6).

An excellent Holocene–middle Pleistocene record was recovered at Site U1353. Additionally, some of the older early Pleistocene–Miocene seismic reflectors in the offshore Canterbury Basin, which at this site occur at relatively shallow depths, were penetrated. Poor core recovery from the early Pleistocene–Miocene section hindered lithostratigraphic interpretation in deeper parts of the hole.

The core-based lithologic unit descriptions below are based primarily on sedimentologic features observed in the core, including sedimentary texture and structures and smear slide and thin section observations (Table T2). We integrated these observations with X-ray diffraction (XRD) data from the dominant lithology in each core, physical property data from whole-round analyses and downhole logging (see “Physical properties” and “Downhole logging”), and paleontology (see “Biostratigraphy”) and correlated them with seismic reflection profiles.

In many instances, intervals of shell hash or sand at the tops of cores were considered to represent downhole contamination by cave-in (Fig. F7; see “Lithostratigraphy” in the “Site U1351” chapter). In addition, similar shell-hash lithologies encountered at the base of many cores were also considered a form of contamination, perhaps caused by sediment being sucked into the base of the cores (flow-in). We estimate that, of the 42% core recovery in Unit II, only a third (~15%) was actually in situ sediment.

Description of lithologic units

Unit I

Intervals: Cores 317-U1353A-1H through 8H and 317-U1353B-1H to Section 28H-2, 46 cm

Depths: Hole U1353A: 0–56.03 m and Hole U1353B: 0–151.36 m

Age: Holocene–early Pliocene

Unit I is heterolithic but characterized by its overall muddy character. The dominant lithology is a dark

greenish gray homogeneous mud (Figs. F4A, F8A) with a few percent very fine sand. Shells are either rare and scattered or locally concentrated in layers as thick as 15 cm. Shells are dominated by the gastropod *Stirocolpus* and, to a lesser extent, by *Tawera* and other bivalves. Bioturbation is common and has an ichnofabric index of 1 (no bioturbation) to 4 (heavy bioturbation). Locally, the mud fraction can be clay rich or clay, the latter either forming centimeter-thick sharp-based beds or occurring as mottles within the relatively coarser mud. Both fining-upward (e.g., Sections 317-U1353B-9H-3 and 9H-4) and coarsening-upward (e.g., Section 19H-3) trends were observed in transitions between intervals of mud and sandy mud.

Subordinate lithologies include

1. Centimeter- to decimeter-thick beds of greenish gray and dark greenish gray very fine sandy shelly mud shell layers to shell hash (Figs. F4B–F4C, F8B–F8C) mixed with siliciclastic materials (fine to medium sand) and abundant *Stirocolpus*, *Tawera*, echinoid spines, barnacle plates, bivalves, gastropods, and rare pebbles of graywacke sandstone as large as 1.5 cm in diameter. The sandy shelly mud and shell hash often occur as centimeter- to decimeter-thick beds at the top of the core, where they may represent cave-in;
2. Very dark greenish gray, well-sorted, very fine to fine (mostly very fine), highly micaceous sand with rare broken shells (Fig. F4D). The sand typically has a soft and soupy appearance in the core and may have been partially fluidized during drilling. Bedding relationships are not always preserved, and the limited number of upper contacts makes bed thickness estimates difficult; and
3. Sandy marl (Fig. F4E) that occurs as a rather thick, presumably Holocene record in the uppermost part of the hole (Cores 317-U1353A-1H and 2H and 317-U1353B-1H and 2H). The sandy marl consists of dark greenish gray, micaceous, homogeneous very fine to fine sandy marl as thick as 8 m and a similar greenish gray, moderately sorted very fine to fine sandy marl to calcareous sandy mud with common to rare shell fragments that occurs below Core 317-U1353B-8H (Fig. F8C).

A considerable amount of potential caved material was recovered in Hole U1353B below Section 317-U1353B-5H-1 (27.7 m). Cores are typically capped by a shell-hash lithology in the top few decimeters before transitioning, often through a soupy, mud-rich interval, into what is considered to be in situ sediment. Despite cave-in and flow-in, a discernible stratigraphy of mud with subordinate clay, sand, sandy marl, and sandy mud predominates.

Muddy shell hash or shelly mud cave-in first occurs at the top of Cores 317-U1353B-5H, 6H, and 7H and again in Core 12H. These occurrences may represent in situ sediments. Below this depth, the first example of definitely caved, washed, mud-free shell material occurs at the top of Core 317-U1353B-17H (Fig. F7B). The composition of the washed shell-hash intervals changes downhole. Species of the family *Turritelidae* are abundant in the upper intervals, whereas below Core 317-U1353B-26H the shells appear coarser and are dominated by bivalve fragments. Graywacke and quartz pebbles are often present in the shell-hash intervals (Fig. F7), as are irregular pieces of cemented shelly sandstone and limestone.

The mineralogy and component types of the sediments, as estimated from smear slides (see “[Site U1353 core descriptions](#)”), are similar to those observed at Site U1351, mainly quartz and feldspar, with lesser dense minerals (e.g., epidote group, amphibole group, zircon, sheet silicates [biotite, muscovite, and chlorite], and rock fragments) (Fig. F9). The exception is that the rock fragments in the detrital fraction include metasedimentary as well as low-grade metamorphic fragments (phyllite) to schist. During the course of routine foraminiferal examination of core catcher samples, sand-sized garnet grains were observed and collected in Sample 317-U1353A-2H-CC, but these were not encountered in core examinations.

The authigenic components include pyrite and other opaque minerals that commonly occur as microscopic spheroids (e.g., mainly foraminifers, nannofossils, and sponge spicules, both siliceous and calcareous). The biogenic components are the same as those observed at Site U1351, including didemnid ascidian spicules, which are very common in the top part of the succession and have a highly variable abundance below Core 317-U1353B-28H.

Mineralogy determined from XRD analyses generally agrees with smear slide composition, especially for quartz, clays, hornblende, and calcite (Fig. F10). Unit I XRD mineralogy is highly variable depending on the lithology, which is consistent with the heterolithic nature of the unit. Quartz, calcite, total clays, micas (muscovite/biotite), chlorite, plagioclase, alkali feldspars, hornblende, and pyrite occur throughout Unit I, but their concentrations are quite variable. Dolomite and siderite are possibly present in a few of the analyzed samples, but the peak heights for these samples are generally close to the limit of detection. Total clays are highest overall in homogeneous mud and lowest in calcite-rich intervals and calcareous sandy mud and sandy marl. Quartz content is highest in well-sorted sand and siltier mud. Calcite content is inversely related to total clays,

with the highest content in calcareous mud/marl and the lowest in homogeneous mud. Micas are highly correlated with each other and weakly correlated with total clays and tend to follow the same lithologic associations as total clays. Hornblende and plagioclase are well correlated and roughly follow the same trend and lithologic association as quartz. Pyrite content is low (many peaks are near detection limits) and highly variable, with a weak positive correlation with calcite and an inverse correlation with quartz and clays.

Unit I/II boundary

A pronounced burrowed contact at Section 317-U1353B-28H-2, 46 cm (151.36 m), is taken to represent the base of Unit I (Fig. F11A). Burrows at this surface (Option A) are filled with sandy marl from the overlying lithology and extend 20 cm into the underlying mud. Sharp-based clay beds occur for a few meters below this to Section 317-U1353B-29H-4, 58 cm (155.46 m), but for convenience and correlation purposes we consider the contact at 151.36 m as the most appropriate surface to use for defining the base of Unit I. Other potential basal contacts include the following:

- Option B (Section 317-U1353B-24H-2, 121 cm [137.07 m]), where a silty mud with common shells occurs above a bioturbated mud (Fig. F11B). Marl and clay beds, however, occur below this interval, and, because this surface is not as pronounced as the contact at 151.36 m, we prefer to retain the latter as the most appropriate boundary (Fig. F11A); and
- Option C (Section 317-U1353B-34H-2, 32 cm [178.82 m]), where a folded, clay-rich muddy interval rests sharply on a muddy shelly fine sand (Fig. F11C).

Unit II

Interval: Sections 317-U1353B-28H-2, 46 cm, through 98X-CC

Depth: 151.36–604.65 m

Age: early Pliocene–middle to early Miocene

Although Unit II is also characterized by its muddy nature, it is differentiated from Unit I by its general lithologic uniformity. It lacks the clay interbeds and greenish sandy mud and marl lithotypes present in Unit I, and beds of sand (or sandstone) are not common. The few occurrences of sand in Unit II could potentially be caved artifacts.

The dominant lithology of Unit II consists of two similar, rather homogeneous muddy sediment types (Fig. F12A–F12B). One is a dark greenish gray, micaeous very fine sandy mud. In this lithology, shells

may be present within centimeter-thick diffuse shelly layers. Burrows are common and typically occur as dark gray fine sand-filled structures of a few millimeters to a centimeter in diameter. A second lithology consists of dark greenish gray, gray, and greenish gray mud with minor amounts of very fine to fine (mostly very fine) sand. Both types of sediment have no bioturbation to complete bioturbation (ichnofabric indexes of 1–5). Rare graywacke sandstone pebbles as large as 1.5 cm in diameter occur scattered throughout the sandy mud and mud (Fig. F12C). Where present, shells are represented by partially dissolved specimens and dominated by bivalves and gastropods, including *Ostrea*, *Dosinia*, *Maoricolpus*, and rare scaphopods. No distinct sedimentary structures were observed, but biscuiting throughout this generally poorly recovered unit could have masked them. Rare soft-sediment folding occurs as open folds in interval 317-U1353B-34H-1, 60–85 cm (177.6–177.85 m).

Calcareous sandy cemented zones with abundant shells first appear with cave-in or flow-in material in Sections 317-U1353B-31X-CC, 33H-3, 34H-1, 34H-4, and 34H-CC. Sands with abundant shells were also recovered in situ (Fig. F11C). Thin sections show that these samples consist of sandy limestone with little evidence of bioturbation and contain randomly oriented shell clasts and abundant residual intraparticle porosity. Both of these examples contain glauconite grains and authigenic glauconite infilling foraminifer chambers and borings in shell fragments. Although pyrite infilling of foraminifers is commonly present in the muddy sediments, no examples were observed in thin section. Concretions lower in the section (e.g., Core 317-U1353B-88X) are similar to those found at Site U1351, being bioturbated, matrix rich, sandy, slightly fossiliferous marlstone.

Sand occurs sporadically throughout Unit II as a minor component and consists of very dark greenish gray shelly muddy fine sand, often with calcareous concretions as large as 4 cm in diameter. They form beds as thick as 15 cm.

Shell-hash units that occur at the tops of cores are thought to represent downhole cave-in, as noted in Unit I. These layers occur commonly as deep as Core 317-U1353B-60H but are less common in deeper intervals.

All of the minerals observed in Unit I are present in Unit II, but hornblende and green ferromagnesian mineral concentrations are substantially lower in the uppermost part of Unit II and are not observed below 365 m in XRD data (Figs. F9, F10). Micrite occurs

in many samples below Core 317-U1353B-29H, and well-crystallized rhombs of carbonate are very common in occasional samples (e.g., Cores 47H and 76X).

Correlation with wireline logs

Gamma ray and resistivity logs were acquired in Hole U1353C, a designated logging hole, prior to hole abandonment. Caliper data from Hole U1353C indicate that the hole was enlarged, but the caliper made contact throughout the entire section and the logging data are likely of acceptable quality (see “Downhole logging”).

The computed gamma ray (CGR) log from Hole U1353C was used to examine downhole changes in lithology and was compared with the CGR log from Hole U1351B (Fig. F13). As noted in the “Site U1351” chapter, gamma ray values for Canterbury Basin sites are likely influenced by changes in both clay mineral content and bulk mineralogy (e.g., feldspar, mica, and chlorite) content. As in Hole U1351B, sandy layers of meter-scale thickness described in the cored interval of Hole U1353B correspond to low peaks in CGR (e.g., Sections 317-U1353B-28H-1, 130 cm, to 28H-2, 150 cm), indicating that low gamma ray values (low clay mineral content) can be used as a proxy for coarser grained sediment.

Within the uppermost 100–250 m in Hole U1353C (~100–300 m in Hole U1351B), large-scale increases and decreases in gamma ray values are interpreted as broad-scale fining- and coarsening-upward intervals (Fig. F13). The variable character of the gamma ray log in this interval is similar to that seen in Hole U1351B, with high-amplitude (~70 gAPI) swings over <10 m vertical distances. This variability can likely be attributed to textural changes (probably layer thickness of intercalated sand and mud) and is consistent with the heterolithic nature of Unit I.

Although the uppermost 250 m in Hole U1353C has a variable gamma log over relatively short vertical distances, the interval below has more gradual trends that are very similar to those in Hole U1351B below 300 m (equivalent to lithologic Unit II at both sites). The characteristics of the gamma ray log are consistent with the limited lithologic variability of Unit II in adjacent Hole U1353B. A number of distinctive increasing–decreasing (likely fining–coarsening) trends in gamma ray values (e.g., 370–480 m in Hole U1353C) can be correlated between the two sites, which suggests that both sites experienced comparable large-scale changes in sedimentation influenced by eustasy, climate, or sediment supply. No-

table differences between the two sites within this depth interval include the lack in Hole U1353C of a slight overall fining-upward trend observed between 300 and 550 m in Hole U1351B and generally lower mean gamma ray values in Hole U1353C (~50 gAPI versus ~60 gAPI in Hole U1351B), which likely indicate lower clay mineral contents at the more proximal shallow-water location of Site U1353.

Downhole trends in sediment composition and mineralogy

Mineralogical and compositional trends are gradational from Unit I to Unit II, but each unit has a notably different character. Unit I mineralogy is highly variable depending on lithology, which is consistent with the heterolithic nature of the unit. Quartz, calcite, total clays, micas (muscovite/biotite), chlorite, plagioclase, alkali feldspars, hornblende, and pyrite occur throughout Unit I, but their concentrations are quite variable (Figs. F9, F10). Dolomite and siderite were occasionally observed, but peak intensities are close to the limit of detection (see XRD in “Supplementary material”). Siliceous bioclast concentrations do not exceed 1%.

Although no discernible downhole trends in mineralogy are apparent in Unit I, recognizable changes in mineral content occur in Unit II below 260 m. Quartz and total clay content are generally inversely correlated, with the lowest quartz (highest clay) content between ~151 and 260 m. Total clay content based on XRD analyses is highest in homogeneous mud, especially in the uppermost 50 m of this unit. Quartz peak intensities are highest in cores that are predominantly very fine, well-sorted sandy mud and muddy sand. Calcite is again inversely correlated with total clays and quartz, and abundance is highest in shell-rich muddy sand and muddy sandstone. As at other sites, the depth trends in calcite follow smear slide and bulk CaCO₃ concentrations. Micas are highly correlated with each other and generally follow the same depth trend as plagioclase.

A notable decrease in clay and an increase in quartz and sheet silicates (especially chlorite) occurs from the top of the unit to ~260 m, below which the mean values remain relatively constant, with variance that is less than that observed in Unit I. An abrupt change in mineralogy, as observed in smear slides and by XRD analyses, occurs at ~260 m between Cores 317-U1353B-61X and 62X, the point at which layers with high carbonate concentrations no longer occur (apart from outliers, which are all related to diagenetic effects—e.g., rhombs observed in Core 317-U1353B-76X and concretions). In addition to low carbonate concentrations, the sediments be-

low this interval, with the exception of lithified intervals, also have extremely low ferromagnesian mineral concentrations as well as higher dense mineral concentrations. Nannofossil and planktonic foraminifer abundances also are extremely rare below this depth (see “Biostratigraphy”).

Description of lithologic surfaces and associated sediment facies

The description of lithologic surfaces and their associated packages as Types A, B, and C follows that of Site U1352 (see “Lithostratigraphy” in the “Site U1352” chapter). Because of time restrictions on board ship, surfaces were only examined close to the predicted depths of seismic sequence boundaries; therefore, the lithologic surfaces identified here are implicitly linked to the predicted occurrences of sequence boundaries identified on the seismic (Lu and Fulthorpe, 2004). A similar approach was used on board ODP Legs 150 and 174A, the objectives of which were also the study of sea level changes. Post-cruise study will attempt to clarify the exact relationship of all lithologic surfaces and facies associations to sea level changes and seismic stratigraphy. The numbering system used in the site chapters, tables, and summary diagrams comprises a hole-specific prefix and a surface designation (e.g., U1353A-S1) that links each surface to a seismic sequence boundary; therefore, these lithologic surfaces and associated sediments are thought to be correlative between sites across the transect. The lithologic surfaces and facies associations identified at this site are designated U1353A-S1 and U1353A-S2 and U1353B-S1 to U1353B-S10 (Table T2).

Surfaces U1353A-S1 and U1353B-S1

Both recovered intervals show a ~4 m thick, very dark gray, micaceous, well-sorted very fine grained sand bed. The sand is present from Sections 317-U1353A-3H-4 through 3H-6 (13.80–18.05 m) and from Sections 317-U1353B-2H-4, 45 cm, through 2H-7 (12.95–16.79 m). Surfaces U1353A-S1 and U1353B-S1 are tentatively placed at the top of the sand. Surfaces U1353A-S1 and U1353B-S1 separate the sand from the dark greenish gray calcareous sandy mud above, comprising a Type A contact and associated facies. The sediment beneath the sand in both holes is gray mud with rare shells and shell fragments.

Surfaces U1353A-S2 and U1353B-S2

Holes U1353A and U1353B contain 6 and 8 m thick fine sand beds of Type A, respectively. The intervals are Sections 317-U1353A-5H-2 through 5H-CC

(27.97–34.15 m) and 317-U1353B-4H-1, 95 cm, through 5H-6 (26.95–35.58 m). The upper contact of the sand bed is sharp in Hole U1353B, but the lower contact was not recovered in either hole. Surfaces U1353A-S2 and U1353B-S2 are tentatively placed at the top of the sand at ~27 m (Table T2). The sand is similar to that associated with U1351A-S1 and U1351B-S1, but the sediment above contains abundant shells (*Chlamys delicatula* and *Stirocolpus*) and broken bivalves and gastropods. The gray mud beneath contains rare shells and shell fragments (mostly *Stirocolpus*).

Surface U1353B-S3

Surface U1353B-S3 is positioned at Section 317-U1353B-9H-3, 88 cm (60.68 m), between green calcareous mud and gray mud. The sediments beneath in Cores 9H and 10H (62–67.56 m) are also typical of a Type A contact and facies association. The repetitive stratal relations (gray mud beneath green calcareous shelly mud) found in Cores 9H and 10H are similar to those found in Hole U1351B, where several depositional events are present within a 10 m interval.

Surface U1353B-S6

Surface U1353B-S6 is possibly located at Section 317-U1353B-23H-2, 140 cm (133.10 m), at the base of a series of shelly mud beds with gradational upper and lower contacts. This identification is largely motivated by biostratigraphic results that indicate a hiatus in Core 23H between the Pleistocene (1.69–1.73 Ma) and Pliocene (>2.78 Ma) between 121.16 and 135.71 m (see “[Biostratigraphy](#)”).

Surface U1353B-S7

A typical Type A contact and facies association defines U1353B-S7 at Section 317-U1353B-28H-2, 40 cm (151.3 m). This is the Unit I/II boundary (Fig. F11A).

Surfaces U1353B-S8 and U1353B-S9

These surfaces are positioned at the base of a sandy marl bed (Section 317-U1353B-34H-2, 50 cm [179.0 m]) and a slump and shelly mud interval (base of Section 41H-CC [202.84 m]). Downhole gamma ray logs contribute to this interpretation by revealing a dramatic increase from 20 to 65 counts per second (cps) at 180 m that correlates to a decrease in the resistivity logs and a similar increase at 205 m (see “[Downhole logging](#)”). These trends suggest that the surfaces occur near a transition between sandy and muddy lithologies and potentially represent either a Type A or B contact and facies association.

Surface U1353B-S10

This surface is tentatively positioned at 252.6 m at the top of gray sandy mud that grades upward to a shelly muddy sand bed (Section 317-U1353B-57H-1, 100 cm [252.6 m]). This designation is largely motivated by biostratigraphic results that indicate a potential highstand in this interval. A sand bed is also present in Section 56H-1 (250.2–251.6 m), which contains abundant fragments of bivalves, scaphopods, and barnacles. This interval is unusual in that it also contains a graywacke pebble and large fragments of *Crassostrea*?

Discussion and interpretation

Interpretation of Unit I

Unit I represents a heterolithic assemblage that was likely influenced by fluctuating sea level during deposition. The Type 1 and Type 2 cycles, as described in “[Lithostratigraphy](#)” in the “Site U1351” chapter, may also exist at Site U1353 but are not as prominent. Such cycles occur in the uppermost 30 m of Holes U1353A and U1353B, but poor recovery below hampers further definition of them below this depth.

The dominant homogeneous mud is interpreted as a shelf facies. Given its uniform nature and lack of sedimentary structures, it is not easy to interpret purely from a sedimentologic perspective. The macrofauna from these muds suggests deposition in fluctuating inner to outer shelf settings. Benthic foraminifers indicate that water depth fluctuated throughout deposition, ranging from subtidal to outer shelf (see “[Biostratigraphy](#)”). The muddy character suggests that the site was largely removed from major sources of sediment. Interbedded gray clay beds may represent episodic fluxes of fine-grained sediment derived from fluvial or glacial discharges. These conclusions are similar to our interpretation of the muds of Unit I at Site U1351 (see “[Lithostratigraphy](#)” in the “Site U1351” chapter).

Similarly, the sandy intervals probably represent transgressive or regressive periods. The green shelly mud may represent periods of late highstand and regression, when more calcareous sediment was deposited and perhaps when terrigenous sediment diminished. The gray sandy intervals are not particularly well recovered, and their top and bottom contact relationships are not preserved in core, being either soupy or nonrecovered. They contain scattered shells, are well sorted, and have a composition consistent with derivation from Torlesse graywacke. We suggest that they represent either transgressive shoreface deposits or sediment deposited immediately after the transgression period (see Browne and

Naish, 2003). Shell-hash intervals were likely formed in a shoreface setting through to beach and were probably also a transgressive shoreface deposit.

Interpretation of Unit I/II boundary

The three boundary options (A–C) described in “**Unit I/II boundary**” may be equivalent to some of the four boundary options described in “**Lithostratigraphy**” in the “Site U1351” chapter; however, our ability to further test this hypothesis is limited because of poor core recovery at Site U1353.

Smear slide and coulometry data show a peak in carbonate percentage from 140 to 150 m associated with the sediments overlying the Unit I/II boundary. In Unit I, homogeneous gray mud has a variable carbonate composition, but below the boundary the mud only rarely contains calcareous material. The variability in carbonate content in the uppermost 100 m of the succession (Figs. F9, F10) is associated with other lithologies, such as greenish gray sand or sandy mud or shell beds. Smear slide and XRD data also indicate a reduction in ferromagnesian minerals at ~152 m (Figs. F9, F10).

Placing the boundary at Section 317-U1353B-28H-2, 46 cm (151.36 m), would be consistent with a similar occurrence of clay beds below the Unit I boundary and within Unit II at Site U1351 (see “**Lithostratigraphy**” in the “Site U1351” chapter).

Interpretation of Unit II

Poor core recovery and moderate to intense drilling disturbance in Unit II at Site U1353 precludes detailed interpretation of its generally texturally uniform muddy character. Lithologies other than muds that would provide useful information regarding environments of deposition were not recovered. In addition, the generally poor preservation of fossils in Unit II (foraminifers and nannofossils) hinders detailed depositional interpretation. Planktonic foraminifers are absent below Core 317-U1353B-60X. Benthic foraminifers show a generally shallow but variable subtidal to outer shelf marine character (see “**Biostratigraphy**”). A trend like that in Unit II in Hole U1351B, where planktonic foraminifers show a downhole increase in abundance and a change from a continental shelf environment to a more open ocean continental slope setting, was not observed in planktonic foraminifers at Site U1353 (see “**Biostratigraphy**”). Nannofossils are not present in many samples (especially between Cores 317-U1353B-89X and 97X, with the exception of Core 90X). Macrofaunas indicate a range of inner shelf to outer shelf depositional settings.

These observations, together with the general mud-rich nature of the unit, suggest a relatively quiet depositional setting on a shelf below a fair-weather wave base. The lack of abundant carbonaceous debris may suggest that the setting was more likely a middle to outer shelf setting removed from major sources of sediment supply. Similar conditions occur on the modern shelf, where much of the Holocene sediment is palimpsest with little terrigenous sediment reaching the middle to outer portions of the shelf (Herzer, 1981). The relatively consistent mineralogy for this unit attests to sediment supply from a single source. Infrequent sand beds and deviations in mineralogy, as well as shelly layers within the mud and sandy mud, may represent occasional storm deposition or derivation of sand from a coastal source (beach or river). The presence of rare graywacke pebbles may also represent storm-related offshore transport of coarse material.

The gross lithology of Unit II is similar to that observed in the Tokama Siltstone on land (Carter, 2007), in Unit II at other sites, and at ODP Site 1119 and likely represents an equivalent sedimentary package. Texturally, the generally uniform nature of the sandy mud and mud lithologies in Unit II is similar to the mud/mudstone of the above-mentioned units.

We suggest that Unit II at Site U1353 represents an extraneritic and/or outer shelf to uppermost bathyal setting based largely on planktonic foraminifers. Equivalent units at Site U1351 were interpreted to have been deposited from contour currents derived from the south. Site U1353 is landward of Site U1351 and would have been in a shallower setting, but it may also have been influenced by similar northward-flowing contour parallel currents in the form of sediment drifts. However, Unit II at Site U1353 had a greater sediment input from source areas to the west, as indicated by its sandier content, discrete shelly layers, and rare graywacke pebble clasts.

Significant hiatuses are recognizable from fossil group ages (see “**Biostratigraphy**”), but these were not often recovered in the core, implying considerable periods of erosion and missing sections that were likely caused by sea level and/or tectonic fluctuations that affected the shelf environment.

Interpretation of lithologic surfaces and associated sediment facies

Surfaces U1353A-S1 and U1353A-S2 and U1353B-S1 to U1353B-S4

These surfaces are well-defined Type A and Type B contacts and associated facies and are tentatively

correlated to seismic sequence boundaries U19, U18, U17, and U16 (Table T2). The upper two surfaces in both holes, correlated to U19 and U18, are associated with thick fine sand beds that are continuous in both holes. Similar well-sorted, fine gray sand is associated with U1351B-S2 and correlated to U18 at outer shelf Site U1351. However, the inner shelf sand beds of Site U1353 are thicker (up to 8 m) than those of the outer shelf. Surface U1353B-S3 is recognized by a sharp basal contact at 63 m and correlates with the predicted depth of U17 at 59 m. Poor recovery (Core 317-U1353B-13H included only a core catcher sample and Core 15H had no recovery) prevents lithologic correlation with U16 (72 m). This boundary may occur at the base of a calcareous very fine sandy mud at 80.8 m (Section 317-U1353B-14X-CC). Biostratigraphy shows a hiatus of ~0.8 m.y. from 0.5 to 1.26 Ma between Sections 12X-CC and 14X-CC, which is consistent with U16 near this interval.

Surfaces U1353B-S6 to U1353B-S10

Surface U1353B-S6 is tentatively correlated with U13, which has a predicted depth of 112 m, and U1353B-S7 is tentatively correlated with U12, which has a predicted depth of 151 m. A correlation to U11 cannot be established because of a no-recovery interval at its predicted depth of 171 m. Surfaces U1353B-S8 and U1353B-S9 are tentatively correlated to U10 and U9, which have predicted depths of 192 and 241 m, respectively. However, because of core recovery, sediments and surfaces below 150 m are questionable. Surface U1353B-S10 is tentatively correlated to U8, which has a predicted depth of 290 m (Fig. F14).

Biostratigraphy

Calcareous nannofossils, planktonic and benthic foraminifers, and diatoms from core catcher samples were used to create a shipboard biostratigraphic framework for Site U1353 (Fig. F15). Benthic foraminifers were also used to estimate paleowater depths. All depths in this section are reported in m CSF-A.

Site U1353 contained a Holocene to Miocene succession. Thirteen biostratigraphic events were recognized, mostly in the Pleistocene (Table T3). Pleistocene nannofossil abundances were high, and good preservation allowed for robust age control. Diatoms were sparse to absent at this site. A hiatus was recognized within the middle-early Pleistocene between Samples 317-U1353B-12H-CC and 14X-CC (80.12–80.77 m), where ~0.8 m.y. was missing.

The Pliocene/Pleistocene boundary was biostratigraphically picked between Samples 317-U1353B-21H-CC and 23H-CC (121.16–135.71 m), where part,

if not all, of the upper Pliocene was missing. Biostratigraphic analysis of Site U1353 Pliocene and Miocene sediments was problematic for all microfossil groups because of either low abundances and/or the absence of key biostratigraphic markers. Below Sample 317-U1353B-60H-CC (257.69 m), nannofossil abundances dropped sharply and remained low for the rest of the downhole succession. Planktonic foraminifers were absent in most samples below this level. Shelfal benthic foraminifers were present in abundance throughout this succession but lacked reliable age markers.

Nevertheless, several important datums allowed for biostratigraphic constraint and critical correlation with Sites U1351 and U1352. The boundary between the middle and early Pliocene was recognized on the basis of a nannofossil datum between Samples 317-U1352B-27H-CC and 28H-1, 124 cm (149.68–150.64 m). The presence of an age-diagnostic planktonic foraminifer lower in the succession constrained the interval between 150.64 and 256.04 m to the early Pliocene (3.7–4.3 Ma). The Pliocene/Miocene boundary was not picked biostratigraphically.

Although there was no biostratigraphic evidence for late Miocene sediments at Site U1353, nearby Site U1351 contained an expanded late Miocene section, and seismic mapping supports the presence of a similar thick late Miocene interval at Site U1353. A nannofossil marker in Samples 317-U1353B-89X-CC and 90X-CC (518.66 and 528.87 m, respectively), dated at older than 12.03 Ma, suggested there is a substantial hiatus between Samples 88X-CC and 89X-CC (510.52–518.66 m), although the amount of time missing is unknown. Samples below 90X-CC were barren of calcareous nannofossils and planktonic foraminifers, except in the bottommost core catcher (Sample 98X-CC [604.60 m]), which contained an early to middle Miocene nannofossil assemblage. The reliability of this age is unknown because nannofossil reworking was common at other nearby sites and there was no other microfossil evidence to support the age.

Paleowater depths derived from benthic foraminifers ranged from subtidal to outer shelf throughout the Holocene–Miocene section. Pleistocene water depths generally fluctuated between subtidal to middle shelf, although a deepening to outer shelfal depths (correlated to the interval just above the middle-early Pleistocene hiatus) was noted in Samples 317-U1353B-10H-CC and 11H-CC (67.50–73.19 m). Pliocene water depths were generally subtidal to inner shelf but sometimes reached outer shelf depths in the early Pliocene. Middle-early Miocene water depths could not be interpreted reliably because of the low number of benthic foraminifers, but rare

outer shelf and bathyal marker species were noted in some samples.

Calcareous nannofossils

Nannofossil abundances at Site U1353 ranged from barren to very abundant. Considerably more samples were barren at this site compared to outer shelf Site U1351 (Table T4). Preservation was variable and ranged from poor to good. Calcareous nannofossils provided reliable age control throughout the Pleistocene (Table T3). Below the Pleistocene, as at Sites U1351 and U1352, biostratigraphic markers used in mid- to low-latitude Neogene nannofossil zonation were absent (except *Reticulofenestra pseudoumbilicus*). Other species associated with the *Reticulofenestra* lineage were abundant and provided rough age control for the Pliocene section. Pliocene assemblages at Site U1353 were markedly different from those at Site U1351. Most notable was the absence of the middle to early Miocene and Oligocene reworking that was common in the early Pliocene–late Miocene section at Site U1351. This has significant implications for basinward and shelf-edge parallel sediment transport.

Evidence of sporadic cave-in was found between Samples 317-U1353B-17H-CC and 65X-CC (106.80–290.38 m), most often recognized lithologically as downhole contamination of an upper shell-hash layer. Mud within this shell-hash layer contained Holocene–late Pleistocene species, most notably abundant *Emiliana huxleyi*. Core catcher samples containing caved or mixed assemblages are identified in the comments column in Table T4. To account for suspected downhole contamination, some events were recorded between several core catcher samples. Postcruise analysis of infill samples may better constrain these events.

Relative abundance counts were not carried out on six samples (317-U1353B-35H-CC, 44X-CC, 45H-CC, 46H-CC, 47H-CC, and 51H-CC) because the core catchers were composed of shell hash and a cursory examination of these samples revealed caved assemblages.

Holocene–Pleistocene

Although not identified biostratigraphically, the base of the Holocene was tentatively correlated with a distinct lithologic boundary at Section 317-U1353B-2H-2, 43 cm (8.43 m), where greenish gray marly sands overlie gray calcareous muds. Nannofossil abundances were highly variable in Pleistocene samples and ranged from rare to very abundant. Preservation was generally good, although a few assemblages were moderately preserved.

Samples 317-U1353A-1H-CC through 4H-CC (5.44–26.72 m) were zoned in NN21. The base of this zone was defined by the lowest occurrence (LO) of *Emiliana huxleyi* (0.29 Ma) between Samples 4H-CC and 5H-CC (26.72–34.08 m). This datum was correlated with the same stratigraphic level in Hole U1353B between Samples 317-U1353B-3H-CC and 4H-CC (26.06–27.67 m). Samples between 317-U1353A-5H-CC and 8H-CC (34.08–55.97 m) and 317-U1353B-4H-CC and 10H-CC (27.67–67.50 m) were zoned in NN20 (0.29–0.44 Ma), a gap zone between the LO of *E. huxleyi* and the highest occurrence (HO) of *Pseudoemiliana lacunosa*.

The HO of *P. lacunosa* (0.44 Ma; top of Zone NN19) was identified between Samples 317-U1353B-10H-CC and 11H-CC (67.50–73.19 m). Two datums were observed below this interval between Samples 12H-CC and 14X-CC (80.12–80.77 m): the LO of *Gephyrocapsa omega* (1.01 Ma) and the HO of *Gephyrocapsa* spp. >5.5 μm (1.26 Ma). The close proximity of these datums to the top of Zone NN19 suggests that there is a hiatus of ~0.8 m.y, although more refined post-cruise analysis will be necessary to confirm this.

The HO of *Helicosphaera sellii* (1.34 Ma) was constrained between Samples 317-U1353B-14X-CC and 16X-CC (80.77–97.20 m). The LOs of *Gephyrocapsa* spp. >5.5 μm (1.56 Ma) and *Gephyrocapsa* spp. >4 μm (1.69 Ma) were identified between Samples 16X-CC and 18X-CC (97.20–108.44 m); however, because of the broad sample interval, it was difficult to interpret whether the close proximity of these datums represented a hiatus or a condensed section. The LO of *Gephyrocapsa caribbeanica* (1.73 Ma) was identified between Samples 20H-1, 107 cm, and 21H-CC (118.27–121.16 m).

Pliocene

The Pliocene/Pleistocene boundary was biostratigraphically picked between Samples 317-U1353B-21H-CC and 23H-CC (121.16–135.71 m). Sample 23H-CC contained specimens of *Reticulofenestra ampla*, whose HO is dated at 2.78 Ma (Kameo and Bralower, 2000), suggesting an unconformable boundary and the absence of upper Pliocene sediments. Sporadic occurrences of *R. ampla* were seen in the middle to lower Pleistocene succession but were interpreted as reworked because they occurred in samples with other material that was clearly identified as having been reworked. Below 135.71 m, *R. ampla* was ubiquitous.

Nannofossil abundances in the Pliocene section ranged from barren to few, and preservation ranged from poor to good. Biostratigraphic analyses of the Pliocene and Miocene sections from Site U1353 was problematic for all microfossil groups because of low

abundances and/or the absence of age-diagnostic biostratigraphic markers. In addition, several Pliocene samples contained younger caved-in material (Table T4).

The HO of *Reticulofenestra pseudoumbilicus* (3.70 Ma) was observed between Samples 317-U1353B-27H-CC and 28H-1, 124 cm (149.68–150.64 m). *Helicosphaera sellii* and *H. cf. sellii* were consistently present between Samples 55H-CC and 65X-CC (250.14–290.38 m), suggesting that Samples 28H-1, 124 cm, through 65X-CC (150.64–290.38 m) are most likely correlated with Zones NN15–NN12.

Of particular note is Sample 317-U1353B-56H-CC (251.63 m), which contained very abundant calcareous nannofossils. The high abundance of all calcareous microfossil groups, especially planktonic forms, suggests that the sample may represent a condensed high-stand deposit. A similar peak in planktonic and benthic foraminifer abundance was noted in the same sample. Below this level, the abundances of all microfossil groups were very low for the remainder of the cored section.

The interval between Samples 317-U1353B-66X-CC and 88X-CC (300.33–510.52 m) was dated early Pliocene to late Miocene, although the Miocene/Pliocene boundary could not be picked biostratigraphically. The assigned microfossil age was also supported by the presence of the gastropod *Maorimactra ?chrydaea* (Suter) in Sample 85X-CC (480.64 m). It is a marker species that is younger than 6.5 Ma.

Miocene

Miocene nannofossil abundances were variable, and, apart from four barren samples, abundances generally increased downhole and were common in the lowermost Samples 317-U1353B-97X-CC and 98X-CC (595.20 and 604.60 m, respectively).

Cyclicargolithus floridanus was observed in Samples 317-U1353B-89X-CC (518.66 m) and 90X-CC (528.87 m), indicating an age older than 12.03 Ma (Raffi et al., 2006). This suggests a substantial hiatus between Samples 88X-CC and 89X-CC (510.52–518.66 m), although the amount of time missing is unknown. Based on the presence of several specimens of *Helicosphaera vedderi*, the lowermost cored sample (317-U1353B-98X-CC [604.60 m]) has a middle-late early Miocene age.

Planktonic foraminifers

Holocene to Miocene planktonic foraminiferal biostratigraphy for Site U1353 was based on the examination of core catcher samples from Holes U1353A and U1353B (Tables T5, T6, T7, T8). Absolute ages assigned to biostratigraphic datums follow the refer-

ences in Table T3 in the “Methods” chapter. Planktonic foraminifers were present in most samples in the Holocene–Pliocene succession and were generally well preserved, but samples in the lower part of the cored section were generally barren. For planktonic foraminiferal abundances and our interpretation of oceanicity, see Tables T5 and T6 and Figure F16.

Holocene

Although not identified biostratigraphically, the base of the Holocene was tentatively correlated with a distinct lithologic boundary at Section 317-U1353B-2H-2, 43 cm (8.43 m), a lithologic contrast where greenish gray marly sands overlie gray calcareous muds. Samples from this interval, including mudline Samples 317-U1353A-1H-1, 0–1 cm (0.01 m), and 317-U1353B-1H-1, 0–1 cm (0.01 m), and Samples 317-U1353A-1H-CC (5.44 m) and 317-U1353B-1H-CC (7.94 m), contained temperate planktonic foraminiferal assemblages consistent with present-day assemblages at the site. The underlying Sample 317-U1353A-2H-CC (9.18 m) had fewer temperate planktonic indicators and contained a high-energy, shallow inner shelf benthic foraminiferal fauna, a shallow-water mollusk assemblage, and garnet-bearing sand, which suggest a lowstand near-shore deposit.

Pleistocene

Planktonic foraminiferal assemblages in the Pleistocene sections of Holes U1353A and U1353B were characterized by small, thin-walled neritic forms. Planktonic abundance and diversity were very low (<5%) in the uppermost part of the Pleistocene succession between Samples 317-U1353A-3H-CC and 4H-CC (17.95–26.72 m) and 317-U1353B-2H-CC and 5H-CC (16.90–35.53 m), indicating deposition occurred under sheltered neritic conditions. Abundances were slightly higher in Samples 317-U1353A-5H-CC through 8H-CC (34.08–55.97 m) and 317-U1353B-6H-CC through 8H-CC (43.15–56.84 m), reaching a maximum of 31% in Sample 317-U1353B-7H-CC (48.91 m), where deposition occurred under extraneritic conditions. This was interpreted as a possible highstand. In the lowermost part of the Pleistocene section below this level, abundances were generally <5%, indicating that deposition occurred under sheltered inner neritic conditions.

Planktonic foraminiferal assemblages in the Pleistocene section were largely composed of *Globigerina bulloides*, *Turborotalita quinqueloba*, and related forms. *Globoconella inflata*, *Neogloboquadrina pachyderma*, and *Neogloboquadrina incompta* were also commonly present, and *Orbulina universa*, *Neogloboquadrina dutertrei*, and *Truncorotalia truncatulinoides*

occurred sporadically along with rare *Globigerinita glutinata*. A single specimen of the subtropical species *Globigerinella aequilateralis* was also present in Sample 317-U1353B-7H-CC (48.91 m).

Too few age-diagnostic planktonic foraminifers were found for reliable dating, but the presence of *Truncorotalia truncatulinoides* in Samples 317-U1353A-5H-CC (34.08 m) and 317-U1353B-4H-CC (27.67 m) indicated that the uppermost part of the section was younger than 1.1 Ma. The base of the New Zealand Haweran Stage (0.34 Ma) was not identified with planktonic foraminiferal evidence. It was, however, recognized on the basis of calcareous nannofossil dating between Samples 317-U1353A-5H-CC and 6H-CC, above the Pleistocene (Castlecliffian) benthic foraminiferal marker HO *Siphotextularia wairoana*, which occurs between Samples 317-U1353B-8H-CC and 9H-CC (56.84–61.90 m).

Pliocene

Planktonic foraminifers were present in about half of the Pliocene samples examined between Samples 317-U1353B-21H-CC and 59H-CC (121.16–256.04 m), and abundances seldom reached >5% of the total foraminiferal assemblage. Planktonic assemblages were generally composed of small, thin-walled neritic forms, and diversity was low except in Sample 56X-CC (251.63 m), where nine species were identified. A peak in calcareous nannofossil abundance was noted in the same sample.

Planktonic foraminiferal assemblages in the Pliocene succession were characterized by *Globigerina bulloides* and closely related forms. *Turborotalita quinqueloba* and *Neogloboquadrina incompta* were also present in most of the section. *Globoconella inflata*, *Zeaglobigerina woodi*, and *Neogloboquadrina pachyderma* also occurred sporadically.

The Pliocene section contained few planktonic foraminiferal markers, and the bioevents recognized were poorly constrained because of the sporadic nature of the planktonic foraminiferal record. The HO of the middle Pliocene marker *Zeaglobigerina woodi* (2.7 Ma) was noted between Samples 317-U1353B-24H-CC and 25H-CC (139.67–142.86 m).

Early Pliocene–Miocene

Planktonic foraminifers were extremely rare in the early Pliocene to Miocene section between Samples 317-U1353B-60H-CC and 98X-CC (257.69–604.60 m). Species present in this interval were not age diagnostic. The absence of planktonic foraminifers in most of this interval is an enigma, especially given the abundance and good preservation of predominantly low-energy, inner to middle shelf benthic foraminiferal assemblages.

Although its causal mechanism is unknown, we speculate that the absence of planktonic foraminifers may be due to a predominantly offshore wind pattern.

The LO of *Globoconella inflata* was found between Samples 317-U1353B-59H-CC and 60H-CC (256.04–257.69 m), indicating that the section above this level was no older than 4.3 Ma. Although it was not identified, the base of the Pliocene occurred somewhere between Pliocene Sample 59H-CC (256.04 m) and where Miocene calcareous nannofossils were first noted in Sample 317-U1353B-89X-CC (518.66 m).

Benthic foraminifers

Eighty-three core catcher samples from Holes U1353A and U1353B were examined (Table T9) for benthic foraminifers. Four core catcher samples were not used for age and paleowater depth estimates because they contained caved calcareous nannofossil assemblages (see Table T4, comments column).

Benthic foraminifers were dominant among all microfossils in the 150–1000 μm size fraction, and preservation was good in the Pleistocene and ranged between poor and good in the Pliocene and Miocene. Benthic foraminiferal bioevents useful for age control are listed in Table T3.

Holocene–Miocene

The HO of *Siphotextularia wairoana* (0.34 Ma) was observed between Samples 317-U1353B-8H-CC and 9H-CC (56.84–61.90 m). The HO of *Bolivinita pliozea* (~0.6 Ma) was picked between Samples 317-U1353B-10H-CC and 11H-CC (67.50–73.19 m). These datums are consistent with calcareous nannofossil and planktonic foraminiferal ages.

Paleowater depths

Paleowater depths derived from benthic foraminifers ranged from subtidal to outer shelf environments throughout the Holocene to Miocene section. Pleistocene paleowater depths fluctuated between subtidal and middle shelf water depths, although a notable deepening to outer shelf depths (correlated to the interval just above the middle/early Pleistocene hiatus) was noted in Samples 317-U1353B-10H-CC and 11H-CC (67.50–73.19 m). Pliocene water depths were generally subtidal to inner shelf but ranged down to outer shelf in the early Pliocene. Middle–early Miocene paleowater depths could not be reliably interpreted because of the low numbers of benthic foraminifers, but rare outer shelf and bathyal marker species were noted in some samples. Estimates of paleowater depths are given in Fig. F17.

Depth-zone terminology is given in Figure F7 in the “Methods” chapter.

Holocene–Miocene

Two alternating benthic foraminiferal assemblages were seen in the Pleistocene section between Samples 317-U1353B-1H-CC and 20H-CC (7.94–119.16 m). One assemblage consisted mainly of *Zeaflorilus parri* (shallow inner shelf) and *Elphidium charlottense* (estuarine–subtidal) and was associated with *Quinqueloculina incisa* (inner shelf), suggesting a shallow inner shelf environment. The other assemblage consisted of *Notorotalia zelandica* (inner to middle shelf), *Nonionella flemingi* (mid-outer shelf), and *Anomalinoidea sphericus*, implying a deeper depositional environment down to outer shelf. Water depths fluctuated from subtidal–shallow inner shelf to middle–outer shelf, with higher variability and frequency in the upper part of the section.

The Pliocene/Pleistocene boundary was placed between Samples 317-U1353B-21H-CC and 23H-CC (121.16–135.71 m) on the basis of calcareous nannofossil evidence. In these samples, subtidal to shallow inner shelf species *Elphidium charlottense* and *Haynesina depressula* were present. These species have also been reported in the sheltered, slightly brackish seaward part of enclosed harbors or inlets in shallow, subtidal environments (Hayward et al., 1999).

In the Pliocene–Miocene section between Samples 317-U1353B-25H-CC and 83X-CC (142.86–461.26 m), *Astrononion* spp. and inner to middle shelf species *Notorotalia inornata* and *N. zelandica* were dominant. The genus *Astrononion* has been reported in sheltered inner to middle shelf environments in New Zealand (Hayward et al., 1999).

Inner to middle shelf (and occasionally shallower or deeper) environments were inferred for most of the Pliocene–late Miocene section. The subtidal to shallow inner shelf species *Elphidium charlottense* occurred sporadically in the upper and lower parts of the section, whereas the outer shelf to upper bathyal species *Uvigerina rodleyi*, *Anomalinoidea sphericus*, *Anomalinoidea parvumbilius*, and *Globocassidulina subglobosa* were observed in the middle part of section.

Between Samples 317-U1353B-85X-CC and 90X-CC (480.64–528.87 m), *Notorotalia* spp., *Bolivina* spp., and inner shelf species *N. aucklandica* were abundant, in association with possible outer shelf species *A. parvumbilius*, where deposition occurred under inner to outer shelf water depths. Rare outer shelf and bathyal marker species were also found in some samples from the lower part of the cored section.

Between Samples 317-U1353B-91X-CC and 98X-CC (537.83–604.60 m), paleowater depths were not esti-

mated because of the paucity and/or poor preservation of benthic foraminifers.

Diatoms

All core catcher samples from Hole U1353A (Samples 317-U1353A-1H-CC through 8H-CC [5.44–55.97 m]) were examined for diatoms (Table T10). Diatoms were only found in Sample 1H-CC (5.44 m). This sample included common, moderately preserved extant coastal taxa but no age-diagnostic species.

Hole U1353B core catcher samples were largely devoid of diatoms (Table T10). Sample 317-U1353B-1H-CC (7.94 m) contained common diatoms and an assemblage similar to that recognized in Hole U1353A, indicating marine deposition influenced by coastal upwelling and river input. Other samples had rare diatom valves, but nannofossil evidence suggested these samples contained “caved” material, and thus they were not used for diatom biostratigraphy.

Macrofossils

Macrofossils were examined in cored sediments from all Site U1353 holes. Provisional identification, age, and habitat preference are provided in Table T11.

Paleomagnetism

Paleomagnetic analyses at Site U1353 included routine measurement and partial demagnetization of natural remanent magnetization (NRM) of archive section halves and some discrete samples from the working halves of cores. Rock magnetic experiments were also performed on these discrete samples. All depths in this section are reported in m CSF-A.

Section-half measurements

NRM was measured on archive section halves from Holes U1353A and U1353B before and after alternating-field (AF) demagnetization at 20 mT peak fields. Hole U1353A was short and entirely overlapped by Hole U1353B. Measurements for Hole U1353A were also affected by common flux jumps on the γ -axis; therefore, only results from Hole U1353B are presented in Figure F18.

NRM intensities typically vary between 10^{-2} and 10^{-3} A/m and generally increase with depth, whereas reliable magnetic susceptibility from Whole-Round Multisensor Logger (WRMSL) measurements (loop sensor) ranges from 0 to ~100 instrument units. Several of the highest susceptibility intervals are associated with drilling disturbance and were not measured on the superconducting rock magnetometer (SRM). Drilling disturbance includes cave-in at the

tops of cores (similar to Site U1351) and fluidized sands, which retained no original orientation. Two characteristic and relatively thick sandy layers displaying high susceptibility values occur within the uppermost 40 m of Site U1353 and were not measured on the SRM (Fig. F18). The first 10 cores of Hole U1353B (0–67.6 m) were recovered with non-magnetic core barrels. Declination varies between cores but is consistent, both before and after demagnetization, within individual cores. NRM inclinations for these cores are steep and positive and are inferred to result from an axial drilling overprint without a significant radial overprint (Fig. F19A). AF demagnetization at 20 mT revealed moderately steep negative inclinations and scattered declinations among cores (Fig. F19A), consistent with normal polarity in the southern hemisphere. Cores from Hole U1353B are not azimuthally oriented (due to harsh coring conditions), so declinations could not be corrected.

From Core 317-U1353B-10H (67.6 m) downward, standard (magnetic) steel core barrels were used because of their greater strength. AF demagnetization reduced the intensity of the samples, but declinations are consistently clustered around north and inclinations are steeply positive both before and after demagnetization (Fig. F19B), which is consistent with a pervasive drilling overprint.

Discrete measurements

NRM demagnetization

Stepwise AF demagnetization (to 80 mT) of discrete samples from Hole U1353B revealed a steep component that was removed at or before the 20 mT demagnetization step (Fig. F20). Some samples then show a characteristic component that demagnetizes to the origin (Fig. F20A), whereas demagnetization at 20 mT peak fields reduced the intensities of other samples to the noise limit of the SRM (Fig. F20B–F20C). One sample (~152 m) with relatively high NRM intensity appears to unblock a characteristic downward component after a short, poorly defined, steep component was removed at low fields (Fig. F20D).

IRM acquisition and demagnetization

In order to investigate the magnetic mineralogy of the sediments, a series of isothermal remanent magnetization (IRM) experiments were conducted on the suite of samples for which NRM had been AF demagnetized. IRM acquisition follows a steep curve, with all samples appearing to saturate between 400 and 600 mT applied fields (Fig. F21). Backfield IRM reveals a variable coercivity of remanence within the

sample set. Samples from 46.56 and 152.38 m show higher coercivity (~80 mT), whereas the other three are lower (~40–50 mT).

A 1 T IRM was imparted twice more on this sample set, and the samples were demagnetized with alternating fields (stepwise to 80 mT; Fig. F22A–F22B) and then thermally (stepwise to 500°C; Fig. F22C–F22D). Under AF demagnetization, samples from 46.53 and 152.35 m have a convex-up demagnetization profile and higher median destructive fields (MDFs; 55–60 mT) than the other samples, which have concave-up profiles and MDFs of ~35–40 mT. The remanence of all samples significantly drops from 250° to 390°C. Samples from 46.53 and 152.35 m lose >90% of their remanence by 390°C, whereas the remaining samples lose <80% by this point. Magnetic susceptibility was monitored for all samples after heating to >250°C. An increase in susceptibility was seen at 390°C in all but the sample from 152.35 m, and all samples show a considerable increase in susceptibility at 500°C, after which thermal demagnetization was stopped.

These rock magnetic investigations reveal variations in the magnetic behavior of the discrete samples that reflect variations in magnetic mineralogy and/or grain size. Samples from 46.53 and 152.35 m show high magnetic susceptibility, high coercivity, and correspondingly high MDF and lose a large proportion of their remanence between 250° and 390°C. The remaining samples have lower susceptibility, coercivity, and MDF and lose a smaller percentage (50%–60%) of their remanence over the same interval.

The responses of these two groups of samples reflect lithology (Fig. F22E). Samples at 46.53 and 152.35 m are gray mud, whereas the others are green mud/silt. The rock magnetic parameters of all samples are consistent with the presence of variable concentrations of iron sulfides (particularly the significant drop in remanence at ~300°–340°C). The green mud/silt samples, however, retain a higher percentage of their remanence beyond 360°C and have slightly lower coercivities, suggesting the presence of another magnetic fraction (e.g., magnetite), which could be a product of changing depositional environment or postdepositional processes and would, for example, be consistent with more oxic conditions associated with the green sediments.

Magnetostratigraphy

It was not possible to define a magnetostratigraphy at Site U1353. A pervasive drilling overprint exists in all samples recovered with magnetic core barrels, preventing the identification of a characteristic component. Where nonmagnetic barrels were used with

the APC system (to Core 317-U1353B-10H [67.6 m]), the removal of an unstable, steep positive overprint reveals a characteristic negative component interpreted to represent the Brunhes Chron. This is consistent with biostratigraphic results, which predict the Brunhes/Matuyama boundary to lie between Samples 317-U1353B-12H-CC and 14X-CC. No evidence for reversed characteristic magnetizations was identified at Site U1353B.

Physical properties

Gamma ray attenuation (GRA) densitometer bulk density, magnetic susceptibility (loop sensor; MSL), natural gamma radiation (NGR), and *P*-wave velocity measured with the *P*-wave logger (PWL) were measured on all whole-round sections from Holes U1353A and U1353B. Magnetic susceptibility (point sensor; MSP), discrete *P*-wave velocity measured using the *P*-wave caliper (PWC), and spectrophotometry and colorimetry were measured on all section halves from the same holes. Discrete *P*-wave velocity measured with *P*-wave bayonets (PWB), moisture and density (MAD), and sediment strength were measured only on section halves from Hole U1353B. Unless otherwise noted, all depths in this section are reported in m CSF-A.

Gamma ray attenuation bulk density

GRA bulk density was measured with the densitometer at 2.5 cm intervals (measurement time = 3 s). The raw data range from -0.26 to 2.42 g/cm³ (Fig. F23). Cyclic variations in GRA bulk density may reflect varying concentrations of sands, which may not always be in their stratigraphic location within the section.

A comparison of GRA densitometer data with MAD data from Holes U1353A and U1353B yields an unexpected relationship (Fig. F24). Typically, GRA densities are equal to or lower than MAD densities because of coring disturbance, but at this site GRA density estimates are consistently higher than MAD estimates by ~ 0.08 g/cm³. A calibration problem with the GRA instrument was suspected, and measurement of the water standard after core measurements had been completed seemed to support this conclusion, giving a density of 1.1 g/cm³. However, density measurements of distilled water standards during each run of the actual measurements were only 1.03 ± 0.05 g/cm³ at the time Site U1353 cores were measured. This bias was observed during the entire expedition and is insufficient to account for the total differences between GRA and MAD bulk densities at Site U1353.

An alternative explanation is that MAD densities are too low. However, we could not imagine any mechanism that could cause this. One possibility is that systematic addition of water to the samples after whole-round analysis could have somehow affected MAD results. However, MAD samples were collected both before and after whole-round measurements, and both data sets are consistently lower than GRA densitometer measurements (Fig. F24). Systematically low measurements of MAD sample mass or overestimates of volume in the pycnometer seem unlikely because of regular calibration. To date, a satisfactory explanation has not been put forth.

Magnetic susceptibility

Magnetic susceptibility (MSL) was measured at 2.5 cm intervals (measurement time = 2 s), and magnetic susceptibility (MSP) was measured at 5 cm intervals. MSP measurements were made on all sections unless drilling disruption or surface disruption precluded collection of meaningful results (Fig. F23).

Raw MSL data range from 5.5 to 227 instrument units in Hole U1353A and from 0 to 199 instrument units in Hole U1353B (Fig. F23). The signal was filtered using a Gaussian low-pass filter (30 passes; Fig. F23).

In the uppermost ~ 260 m, where core recovery was greatest, MSL and MSP data are highly variable. In contrast, below ~ 260 m, where core recovery was poor, magnetic susceptibility is much less variable. Overall, magnetic susceptibility decreases downhole, but within this trend several shifts were observed. Major shifts between 75 and 79, 160 and 174, 205 and 217, and 258 and 270 m may reflect the presence of unconformities. Below ~ 575 m, magnetic susceptibility appears to increase slightly. However, the corresponding interval is too short for reliable interpretations.

Two abrupt increases in magnetic susceptibility occur at 13–17 and 27–36 m. These intervals are associated with thick sandier units (see “**Lithostratigraphy**,” Fig. F25). Coeval changes were also observed in NGR (low values likely reflect low clay content), GRA bulk density (lower densities), and *P*-wave velocities (higher velocities) (Figs. F23, F26). Several prominent peaks in magnetic susceptibility occur (e.g., at 26, 36, 43, 49, 57, 62, and 68 m) (Fig. F25). These peaks may be linked to caved shell-hash material at the top of each core liner, as observed previously at Site U1351. These findings suggest that the noisy magnetic susceptibility signal below ~ 100 m may be mainly the result of caved material at the top of cores or sandy material sucked into the bottom parts of core liners (flow-in). High magnetic suscepti-

bility related to shell hash might be caused by fine-grained magnetic minerals, which were found to be associated with these sediments in both smear slides and in association with foraminifer samples, or might be caused by rust or other magnetic minerals used in shipboard operations (Richter et al., 2007).

Natural gamma radiation

NGR was measured on all core sections at 10 cm intervals down to 587 m. However, poor core recovery means that only the record from the uppermost 260 m is usable, with mainly “spot” values available below this depth. Even the upper record contains a coring gap between 80 and 105 m.

NGR values measured over the uppermost 260 m range from ~3 to >80 cps, with higher values associated with muddy lithologies and lower values associated with sands (Fig. F23). No particular trend occurs in the record, which is, however, divided into two portions. The interval between 0 and 80 m exhibits a striking “bimodal” cyclicity between high values that correspond to mud and low values that correspond to sand (see “[Magnetic susceptibility](#)”). Assuming, tentatively, that the first two cycles downward correspond to marine isotope Stages (MIS) 1–5 and 6–7, these last two glacial–interglacial cycles have a combined thickness at Site U1353 of ~30 m (36 m to the base of the inferred MIS 7 sand, minus 6 m of Holocene muddy sand at the top of the section). An alternative interpretation is that the cyclicity in the uppermost 36 m at Site U1353 represents only MIS 1–5, which would imply that MIS 2 and 3 are, unusually, fully manifested in the sand/mud packages present.

The section between 105 and 260 m has a more closely spaced, peaked cyclicity than the cycles above, which is consistent with either lower sedimentation rates, sediment compaction, or both. This part of the section is not entirely continuous, but, allowing for the minor gaps, the cyclicity appears to represent at least an additional eight glacial–interglacial cycles. Because of the coring gap between 80 and 105 m, which also corresponds to a demonstrated hiatus, these cycles cannot yet be correlated with the MIS scale and therefore remain as a “floating” package of cycles of broadly mid-Pleistocene age.

The striking cyclic bimodality of the upper two cycles at Site U1353, noting the associated lithologic variations recorded during core description, are similar to extremely shallow water, near-shoreline sedimentary successions described in early Pleistocene cycles in the Nukumaru coastal succession, Wanganui Basin (Birdgrove and Maxwell motifs of Abbott et al., 2005). These successions are distinguished, in

part, by the position of the shoreface sand within each type of cycle—toward the top of the cycle (“regressive”) for the Birdgrove motif and at the base (“transgressive”) for the Maxwell motif.

P-wave velocities

P-wave velocities were recorded continuously in Holes U1353A and U1353B at 2.5 cm intervals using the PWL. Velocities were also recorded with the PWC in both holes and with the PWB in Hole U1353B (Fig. F26). P-wave measurements yielded unexpectedly good results in the muddy portions of the sediment to below 585 m. This is remarkable because P-wave velocity records from Sites U1351 and U1352 were obtained only in the first ~22.5 and ~20 m of soft sediments, respectively. The long record at Site U1353 is a result of the absence of sediment cracking caused by high gas content that was observed at the previous sites. With this data set, an excellent positive correlation was found between PWL estimates from both holes, and a good correlation was found between PWL, PWC, and PWB estimates in Hole U1353B. Nevertheless, PWB P-wave velocities (Fig. F26B) are generally lower than velocities recorded with the PWL and PWC.

Overall, P-wave velocities increase downhole (from averages of ~1500 m/s to ~1800 m/s) in three major steps at 6, 76–106, and 224–229 m. The steps between 76 and 106 m and between 224 and 229 m might reflect the presence of unconformities.

Two abrupt changes in P-wave velocity to higher values between 14 and 18 m and between 26 and 28 m are associated with thick sand layers (see “[Lithostratigraphy](#)”). A similar pattern was observed in magnetic susceptibility, NGR, and GRA bulk density (Fig. F23).

Spectrophotometry and colorimetry

Spectrophotometric measurements and associated colorimetric calculations were made on section halves at 5 cm intervals at the same positions as MSP measurements. Color data were recorded as L*, a*, and b* variations. Changes in color are more abrupt and pronounced at Site U1353 than at Sites U1351 and U1352 (Fig. F27). This is most conspicuously evident in the uppermost ~250 m of Hole U1353B, where core recovery was greatest (Fig. F28). In particular, two clear, abrupt excursions to lower L* and b* values and higher a* values are evident in the uppermost 36 m of Hole U1353B. These shifts coincide with sandy intervals (see “[Lithostratigraphy](#)”). At the stratigraphic level of these excursions, pronounced changes in magnetic susceptibility and NGR also occur (see “[Magnetic susceptibility](#)”),

with the shift to lower L^* values being coincident with high magnetic susceptibility and low NGR (Fig. F28). Downhole, between ~183 and ~189 m, a similar shift to low L^* and b^* and high a^* values is present, coeval with excursions to minimum values in both magnetic susceptibility and NGR and reflecting the occurrence of gravel (Fig. F28; see also “Lithostratigraphy”). Based on these observations, it is clear that the lithologic factors that determine sediment color, magnetic susceptibility, and NGR do not always produce the same signatures at Site U1353.

Low recovery below ~250 m precludes a determination of long-term trends in color data in the lower part of Hole U1353B, although the variation in values below ~250 m demonstrates that high variability in sediment color is a pervasive feature of the entire cored interval (Fig. F27).

Moisture and density

MAD measurements were expanded somewhat at Hole U1353 to perform a sampling experiment. MAD samples were taken on the catwalk from one end of whole-round core sections (MAD catwalk samples) immediately after the sections were cut. One MAD catwalk sample was taken from each core in the uppermost 54 m of Hole U1353A and from cores in the uppermost 178 m and in the interval of 547–617 m (base of the hole) of Hole U1353B in order to extend the test to lower porosity samples. In Hole U1353A, two subsequent samples were taken on the sampling table, one next to the MAD catwalk sample and one near the location of the thermal conductivity measurement. One sample table sample was taken adjacent to the MAD catwalk sample for Hole U1353B cores. Generally, one or two additional samples were taken per core so that the total number of MAD samples was not much greater than the normal 3–4 samples per complete core or 1 sample per section for poor-recovery sections. Unfortunately, poor-recovery sections characterize the bulk of Hole U1353B below ~80 m.

A comparison of MAD catwalk sample porosity results with those of samples taken from the sampling table reveals that, on average, the results are essentially the same (Fig. F29). In fact, they are correlated with a regression coefficient (R) of 0.96. Although MAD catwalk samples have higher porosities in a few cases (notably those taken in the uppermost 20 m), at least as many samples have higher porosities after arriving on the sample table. It would be good practice to take MAD samples prior to discrete P -wave measurements. In any case, analytical variability in MAD data is not unexpected, and some of the variations may be due to real variations in porosity and lithology over very short distances. In some cases, the

differences between results from the two sampling methods are as high as 4%–5% and, as such, are higher than the expected analysis error of at least 1%–2%.

Porosities decrease much more rapidly at Site U1353 than they do at either Site U1351 in a more distal shelf setting or at Site U1352 in an upper slope environment (Fig. F30). With the exception of grain density, curve fitting revealed an excellent relation between these physical properties and depth of burial (Fig. F30). The higher rate of compaction in the uppermost 20 m reflects faster compaction, where the grains move from loose packing toward closest packing, which takes relatively little overburden to achieve (e.g., Bond and Kominz, 1984). Bulk density increases linearly with depth, whereas grain density does not show any statistically significant change with depth. Correlations of porosity and void ratio with depth are stronger as exponential curves:

$$\rho_b = 1.933 + 0.49z \quad (R = 0.75),$$

$$\rho_g = 2.75 + 0.02z \quad (R = 0.09),$$

$$\phi = 47.7e^{-(z/1.386)} \quad (R = 0.81),$$

and

$$v = 0.91e^{-(z/0.82)} \quad (R = 0.75),$$

where

ρ_b = bulk density in g/cm^3 ,

ρ_g = grain density,

ϕ = porosity in percent,

v = void ratio, and

z = depth in kilometers.

Porosity and density trends shift to higher and lower values, respectively, across an interval of poor recovery at ~90 m. This corresponds quite well to a hiatus indicated by biostratigraphic datums at 80 m (Fig. F30). A second hiatus at ~120 m is less well represented in the porosity and bulk density trends. A slight increase in bulk density and a corresponding decrease in porosity occur at the lithologic Unit I/II boundary at ~151 m (see also Fig. F24; see “Lithostratigraphy”).

Sediment strength

Sediment strength measurements were conducted on working section halves from Hole U1353B using automated vane shear (AVS) and fall cone penetrometer (FCP) testing systems (Fig. F31). A comparison of both measurement methods is shown in the crossplot in Figure F31C.

Shear strength indicates that sediments range from very soft (0–20 kN/m²) to very stiff (150–300 kN/m²). Vane shear and fall cone shear strength correlate well in very soft and soft sediments, but AVS values are about three times lower in firm to very stiff sediments (standard deviation = 28.3 kPa) than FCP values (standard deviation = 83.9 kN/m²). A similar pattern was observed at Sites U1351 and U1352. These findings suggest that the applicability of vane shear in firm to very stiff sediments is limited and that vane shear tests underestimate the strength of stiffer sediments. Overall, vane shear and fall cone strength data from Hole U1353B are positively correlated (Fig. F31A–F31B). Between 0 and ~250 m, shear strength increases generally, indicating a change from very soft to firm sediments. The generally lower sediment strength below ~250 m in cores from Hole U1353B coincides with the change from APC to XCB drilling.

A change in sediment strength to lower values between 14 and 18 m is consistent with sharp changes in magnetic susceptibility, NGR, GRA bulk density, and *P*-wave velocity and may suggest the presence of an unconformity (Figs. F23, F26). The pronounced cyclicity observed in the upper portion of Site U1351 was not observed at Site U1353.

Geochemistry and microbiology

Organic geochemistry

Shipboard organic geochemical studies of cores from Holes U1353A and U1353B included monitoring hydrocarbon gases, carbonate carbon, organic carbon, and total nitrogen (TN) and characterizing organic matter with the source rock analyzer (SRA). The procedures used in these studies are summarized in “Geochemistry and microbiology” in the “Methods” chapter. All depths in this section are reported in m CSF-A.

Volatile gases

All cores recovered from Holes U1353A and U1353B were monitored for gaseous hydrocarbons using the headspace (HS) gas technique (Table T12). No significant amounts of hydrocarbons above background laboratory air (1.7–2.4 ppmv) were detected in the uppermost 350 m. Three samples from deeper in Hole U1353B contain 5–32 ppmv methane but no higher hydrocarbons (Fig. F32).

Small amounts of gas were recovered from air enclosed in the core liners of four cores from Holes U1353A and U1353B (Table T13). These samples were reported as core void gas (VAC) samples, but they did not come from actual gas voids within the cores. Two of these samples (Sections 317-U1353B-

9H-4 [61.75 m] and 10H-4 [67.35 m]) contain methane slightly above background levels, one (Section 10H-3 [65.87 m]) contains higher amounts of methane with a trace of ethane, and one (Section 317-U1353A-5H-5 [32.93 m]) contains 717 ppmv of methane with hydrocarbons to C₄ and significantly more CO₂ than is found in air. The C₁/C₂ ratios of the two samples that contain ethane are 163 and 284, respectively.

Carbon and elemental analyses

The results of inorganic carbon (IC), carbonate, total carbon (TC), total organic carbon by difference (TOC_{DIFF}), TN, and TOC_{DIFF}/TN analyses on selected sediment samples from Hole U1353B are given in Table T14. In total, 82 sediment samples were analyzed. TC, TN, TOC, and calcium carbonate contents are plotted against burial depth in Figure F33. Calcium carbonate contents range from 2 to 29 wt% in Pleistocene–Holocene shelf sediments at burial depths <70 m (Fig. F33A). Below 100 m there is a background of low calcium carbonate (0.5–2 wt%) with occasional high values (10–57 wt%). Between 150 and 250 m, carbonate values scatter widely between 0.3 and 57 wt% and then decrease slightly to values ranging between 0.4 and 8 wt% below 270 m, the only exception being Sample 317-U1353B-92X-CC (547.1 m), which has a carbonate content of 39 wt%. TC has a profile remarkably similar to that of carbonate content, with average values generally decreasing downhole and frequent scatter as high as 7.3 wt% above 250 m (Fig. F33B). TC values below 250 m are more uniform and average ~0.3 wt% (with the exception of the above-mentioned sample at 547.1 m). TN amounts are very low and range from 0.003 to 0.08 wt%, with an apparent decrease with depth (Fig. F33C).

TOC generally decreases with depth (Fig. F33D–F33E). Surface sediments are characterized by organic carbon contents of ~0.8 wt% (TOC_{DIFF}) and decrease to ~0.1–0.2 wt% in the deeper layers below 250 m. TOC values determined by the source rock analyzer (TOC_{SRA}) are systematically higher than corresponding values determined by the difference method (TOC_{DIFF}) (Fig. F33E). A cross-plot of TC from the elemental analyzer and the sum of TOC_{SRA} plus IC from the coulometer confirms this observation (Fig. F34). The ratio of TOC_{DIFF}/TN decreases with depth, reflecting the faster decrease with depth of TOC compared to TN (Fig. F33F).

Organic matter pyrolysis

All of the samples used for CNS analysis were also characterized by SRA pyrolysis (Table T15; Figs. F35,

F36). S_1 and S_2 rapidly decrease with depth from 0 to 60 m with ranges of ~0.05–0.25 and 0.1–1.2 mg/g, respectively (Fig. **F35A–F35B**). Below 60 m, the decrease is more gradual, and values are ~0.05 and 0.1–0.2 mg/g, respectively. S_3 decreases with depth in the uppermost 250 m with a range of 0.05–3.8 mg/g (Fig. **F35C**). Pyrolysis carbon necessarily mirrors S_1 and S_2 and decreases with depth from 0.1 mg/g at the sediment surface to 0.01–0.02 mg/g below 400 m (Fig. **F35D**). The hydrogen index ranges from 17 to 127 mg/g C, with higher values in the 0–250 m depth interval (Fig. **F36A**). The oxygen index ranges from 5 to 240 mg/g C, with no apparent trend (Fig. **F36B**). Average T_{\max} values decrease, with temperatures of 415°–420°C in the 0–8.2 m depth interval and 370°–422°C at the bottom of Hole U1353B (Fig. **F36C**). Production index values show a reverse trend and increase downhole from ~18% in near-surface sediments to 30%–34% at depths of 500–600 m (Fig. **F36D**).

A modified van Krevelen diagram (Fig. **F37**) indicates poor-quality organic matter at Site U1353, with most samples clustering near the Type IV kerogen line, similar to Site U1351.

Preliminary interpretation of organic matter

Organic matter content appears to decrease with depth over the uppermost 100 m and remains relatively low throughout the remainder of the sampled section. This probably represents active biological oxidation and roughly correlates with intervals of increased alkalinity and decreased sulfate (see “**Inorganic geochemistry**”). Pyrolysis results suggest a largely terrestrial plant origin for organic matter, but $\text{TOC}_{\text{DIFF}}/\text{TN}$ values suggest some marine influence.

Inorganic geochemistry

A total of 53 interstitial water samples (Tables **T16**, **T17**) were collected and analyzed at Site U1353. Thirty-five samples were taken to 56 m in Hole U1353A, which was dedicated mainly to whole-round sampling for geochemistry and microbiology. Two samples were taken from each of Cores 317-U1353B-9H, 10H, and 11H. Below Core 11H (72 m), sample spacing was largely dictated by core recovery. Only one whole-round core sample for interstitial water analyses was collected below 318 m (Section 317-U1353B-96X-1 [585.8 m]). Interstitial water chemistry is plotted versus depth in Figures **F38**, **F39**, **F40**, **F41**, and **F42**.

Salinity, chloride, sodium, and pH

Salinities in samples near the seafloor are slightly lower than normal seawater at 3.4 and rapidly de-

cline to 2.4 at 38.6 m (Fig. **F38A**). Thereafter, salinity remains relatively constant at 2.4–2.5 to 63.4 m and then increases gradually to 3.4 at 178.4 m. Below this sample, salinity remains constant to 318.5 m, but the deepest sample has a somewhat elevated salinity at 3.8 (Fig. **F38A**). Chloride (Fig. **F38B**) and sodium (Fig. **F38C**) almost exactly parallel salinity measurements. Measured pH values range between ~7.2 and 8.0 with no depth trend (Fig. **F38D**).

Calcium, magnesium, and strontium

Calcium and magnesium both decrease from the surface sediments to the salinity minimum at ~47 m and then increase below this depth (Fig. **F39A–F39B**). Calcium increases to >15 mM below 150 m, considerably above seawater values. In contrast, the magnesium increase below the salinity minimum is only to ~44 mM, showing a net depletion relative to seawater. The Mg/Ca ratio decreases from 5 in the surface sediments to 2.4 in the deepest sample (Fig. **F39C**). Strontium increases in the uppermost 150 m, reaching 0.44 mM, and then decreases to 0.26 mM at 319 m (Fig. **F39D**). In the deepest section of Site U1353, strontium increases again to 0.53 mM. The Sr/Ca ratio initially increases from seawater values of ~0.01 to 0.03 at 60 m. It then decreases from a maximum of 0.032 at 115 m to 0.016 at 319 m (Fig. **F39E**). The deepest sample has an elevated Sr/Ca ratio of 0.03.

Alkalinity, sulfate, ammonium, phosphate, and dissolved silica

Alkalinity increases relatively steeply from 3.2 mM at 1.2 m to 6.5 mM at 6.7 m. It then fluctuates between 5.5 and 6.3 mM to 60 m (Fig. **F39F**). Alkalinity then slowly decreases to ~2.3 mM at 115 m and below. The decline in sulfate appears to be more related to the salinity decrease than to sulfate reduction. After dropping to a minimum of 15.5 mM at 44.1 m, sulfate increases slowly to ~24 mM at 115 m and remains relatively constant to 319 m (Fig. **F40A**).

Ammonium increases from 0.13 mM at 1.2 m to 1.2 mM at 29 m and then remains relatively constant to 38.6 m (Fig. **F40B**). Ammonium then decreases to ~0.6 mM at 60 m, below which it remains roughly constant. Phosphate increases from 3.7 μM at 1.2 m to 7.9 μM at 6.7 m and then decreases steadily throughout the rest of the sampled interval to <0.1 μM at 178 m (Fig. **F40C**).

Dissolved silica is present at 196 μM at 1.2 m, increases to 555 μM at 12.2 m, and then fluctuates between 300 and 629 μM to 72 m (Fig. **F40D**). Below 72 m, dissolved silica decreases rapidly and stays relatively constant at <210 μM .

Potassium, barium, lithium, silicon, boron, iron, and manganese

Potassium decreases from ~11 mM, slightly above seawater, to 4.7 mM at 55 m (Fig. F41A). This decrease closely matches the salinity decline. Thereafter, potassium varies little with additional depth.

Barium rapidly increases between 1.2 and 24.1 m from seawater values to a high of 1.4 μM and then remains relatively constant at ~1.1 μM to 253 m (Fig. F41B). Thereafter, barium increases to 3.0 μM , reaching a maximum of 4.0 μM at 586 m in the deepest sample.

Lithium increases throughout the cored interval at Site U1353 from seawater values of ~24 μM in the shallowest samples to a maximum of 112 μM in the deepest sample (Fig. F41C).

Silicon generally shows trends similar to dissolved silica. Silicon fluctuates in the uppermost 72 m before decreasing rapidly to 135 m (Fig. F41D).

Boron concentrations are at seawater values of ~420 μM in the shallowest samples and decrease to 342 μM at 30 m (Fig. F42A) before gradually increasing to a maximum of 614 μM in the deepest sample.

Iron and manganese show similar trends and tightly co-vary (Fig. F42B–F42C). Above 70 m, iron and manganese concentrations are largely scattered between 12 and 39 μM and 5 and 17 μM , respectively. Below 70 m, both iron and manganese have relatively constant values, except manganese is elevated relative to iron in the three deepest samples (Fig. F42B–F42C).

Preliminary interpretation of diagenesis

Interstitial water geochemistry in the uppermost 150 m at Site U1353 is dominated by the salinity minimum at ~50 m (Figs. F38, F43). The presence of this less saline lens can be explained either by the modern intrusion of meteoric water from land or by the historic remains of freshwater that was emplaced when the shelf was emergent and is now being slowly replaced by the downward diffusion of seawater. A slight alkalinity increase in the 0–7 m depth interval probably represents some degree of sulfate reduction. Sulfate is never depleted and methane is not present above background levels. Either methanogenesis did not occur in these sediments, or previously generated methane was lost when the shelf was emergent or was oxidized when sulfate was replenished by diffusion after a subsequent sea level rise.

Alkalinity, sulfate, calcium, and magnesium were normalized to chloride, which is here presumed to be a nonreactive ionic species, so as to evaluate changes due to reaction rather than dilution (Table

T18). The ratio of chloride surface concentration to measured concentration was used as a normalization factor for every data point, assuming that chloride levels should be constant at surface concentrations over the depth interval of Site U1353 when no dilution by fresher water had taken place. In Figure F44, normalized concentrations are shown along with observed concentrations. Chloride-normalized alkalinity has a somewhat larger increase from 3.2 mM near the seafloor to 9 mM at 54 m. Chloride-normalized sulfate has a depletion of 8 mM from the sediment surface to the concentration minimum over the 38–44 m depth interval. This decrease does not exactly match the alkalinity increase, indicating that sulfate reduction has occurred at Site U1353 and that alkalinity must also be affected by other processes, probably carbonate precipitation and dissolution. Chloride-normalized calcium decreases very slightly in the 0–8 m depth interval but increases in stages below that depth, leveling off at ~16 mM (Fig. F44). The relative increase in chloride-normalized calcium is likely related to the dissolution of calcareous microfossils. In contrast, chloride-normalized magnesium declines steadily over the 10–135 m depth interval, leveling off at ~45 mM.

A small positive increase in boron with increasing depth may indicate the release of a desorbable boron fraction and the degradation of organic matter in the pore waters. The increase in lithium potentially also reflects desorption reactions. The increase in barium at the same time as the decrease in sulfate possibly relates to the dissolution of barite.

Microbiology

Sample collection

Shipboard microbiological studies of cores from Site U1353 included recovering whole-round sediment samples for intact polar lipid analyses and incubation tests, as previously described in “Geochemistry and microbiology” in the “Methods” chapter. Microbiological sediment samples were only taken from the hole dedicated to whole-round sampling (Hole U1353A). Eight whole-round samples were collected for microbiological investigations.

Contamination tracer tests

All whole-round sediment samples were tested for seawater contamination using a particulate tracer. At this site, water-soluble perfluoromethylcyclohexane tracer (PFT) was not employed.

Particulate tracer

Fluorescent microspheres were used as a particulate tracer on all cores from which whole-round samples

were subsequently taken. For each microbiology sample, two subsamples (1 cm³) were collected on the catwalk with a 3 mL cut-off syringe from the periphery and center of the core. A total of 16 samples were collected for contamination tests. Table T19 shows data for potential micrometer-sized particle contamination that could occur during the drilling process. All samples contained large amounts of microspheres on their outside surfaces, showing a heterogeneous distribution of microspheres along the core liner. Five samples (317-U1353A-2H-1 [6.3 m], 3H-1 [10.1 m], 4H-1 [19 m], 5H-1 [27.3 m], and 6H-1 [35 m]; see Table T19) showed high contamination levels (up to 5.8×10^3 beads/cm³) on the center part of the cores, which can be explained by the sampling technique, despite the fact that a 1 cm thick layer was removed during sampling of the inner part of the core on the catwalk. The high water content of cores can sometimes increase the contamination level in the inner part of the cores, particularly in the case of near-surface sediments. Three samples (317-U1353A-1H-1 [0.8 m], 7H-1 [42 m], and 8H-1 [48.8 m]; see Table T19) did not contain any microspheres in the center part of the cores, which indicates that no contamination occurred during the drilling operations.

Heat flow

Geothermal gradient

Only one temperature measurement was made using the APCT-3 in Core 317-U1353A-5H, and its result was poor because the cooling curve was irregular (Fig. F45; Table T20). Accordingly, it was not possible to determine the geothermal gradient and heat flow.

Thermal conductivity

Thermal conductivity was measured in whole-round core sections from Holes U1353A and U1353B using the full-space needle probe method. Measurement frequency was usually more than once per core with five measuring cycles at each point. This included 21 points in Hole U1353A (0.4–53.2 m CSF-A; unless otherwise noted, all depths in this section are reported in m CSF-A) and 75 points in Hole U1353B (0.7–585.5 m) (Table T21). The middle of each section was chosen as the measurement point unless a void or crack was observed (see “Heat flow” in the “Methods” chapter). Few lithologic variations occur in each section at Site U1353, so this sampling procedure was appropriate. Probe V10701 was used, and heating power was kept to ~3 W for the full-space method.

Thermal conductivity data were discarded when (1) contact between the probe and sediment was poor, (2) thermal conductivity was close to that of water (0.6 W/[m·K]) because of sediment dilution during coring, or (3) measurements were taken in caved layers such as shell hash. In most cases, the first two criteria were controlling parameters for monitoring measurement quality. Good results were obtained from 7 points in Hole U1353A and 39 points in Hole U1353B, covering depth intervals of 7.7–31.1 and 5.2–413.5 m, respectively (Table T21). Although the number of measuring cycles was increased to five based on experience gained from Site U1352, many measurements were still discarded because of poor contact caused by loose sediments.

Thermal conductivity measurements at Site U1353 range from 1.122 to 1.840 W/(m·K) (average = 1.546 W/[m·K]) (Table T21). These results are slightly higher than those from Sites U1351 and U1352 for the equivalent depth interval (above ~414 m), probably resulting from the lower porosity at Site U1353 compared to Sites U1351 and U1352. For the uppermost 130 m, thermal conductivity values are also higher at Site U1353 than in the same interval at nearby ODP Site 1119 (Shipboard Scientific Party, 1999). High conductivities at Site U1353 may be due to high concentrations of quartz (6.5–12.5 W/[m·K]) in fine-grained sediment, including the clay-sized fraction (see “Lithostratigraphy”), and/or carbonate cementation (0.5–4.4 W/[m·K]).

Thermal conductivity versus depth data from Holes U1353A and U1353B are consistent (Fig. F46A). Two downhole increasing trends can be recognized: an increasing trend from 0 to 32 m, reaching a peak at ~30 m, and a subsequent drop followed by another increasing trend from 32 to 414 m. The origin of the peak at ~30 m is unclear because bulk density and porosity are fairly constant from 20 to 80 m (see “Physical properties”). However, a similar feature was observed at shelf Site U1351, although the peak at Site U1353 is more pronounced. The following linear trends can be fitted to the thermal conductivity data:

$$\lambda_{0-32}(z) = 1.2165 + 0.0168 \times z \quad (R^2 = 0.4500)$$

and

$$\lambda_{32-414}(z) = 1.2903 + 0.0015 \times z \quad (R^2 = 0.5462),$$

where z is depth (m CSF-A).

Thermal conductivity, in general, correlates negatively with porosity and positively with bulk density

(Fig. F46B–F46C). For sand, these correlations are weaker than for lithologies such as mud.

Downhole logging Operations

Logging operations at Site U1353 began with drilling the dedicated logging Hole U1353C on 26 December 2009. This hole was drilled using the same 11-7/16 inch APC/XCB bit used for Hole U1353B with a center bit installed. The hole was drilled to a total depth of 625 m DRF (529 m DSF), which was reached at 2230 h on 27 December (all times are ship local time, Universal Time Coordinated [UTC] + 13 h). To prepare the hole for logging, the center bit was retrieved and the hole was swept with 50 bbl of high-viscosity mud. The hole was then displaced with 300 bbl of heavy mud (~10.5 ppg), and the bit was raised to the logging depth of 201 m DRF (105 m DSF). Rig up of a modified triple combo tool string began at 0340 h on 28 December. Because of the difficult drilling conditions and poor recovery at this site as well as our experience from logging at the previous sites, no radioactive source was used in this hole. The modified tool string consisted of the Hostile Environment Natural Gamma Ray Sonde (HNGS), the Hostile Environment Litho-Density Sonde (HLDS; without source, for the caliper only), the General Purpose Inclination Tool (GPIT), and the Dual Induction Tool (DIT). The tool string was rigged up by 0410 h and run into the hole at 0416 h at a speed of 3000 ft/h. While the tool was being lowered, natural gamma ray and resistivity data were recorded from the seafloor to a total depth of 622 m WRF, where a first logging pass was started at 0503 h. This repeat pass was completed at 550.1 m WRF, and the tool string was run back down to total depth for a full pass, starting at 0530 h at a speed of 900 ft/h. The caliper was closed at 235 m WRF for reentry into the pipe, and the pass was completed at 0703 h when the seafloor was identified in the gamma ray log at 94.5 m WRF. The tool string was back at the surface at 0750 h and rigged down completely by 0815 h.

The density sonde caliper showed a good borehole with a diameter ranging from 12 to >19.5 inches. We decided that enough daylight remained to run both the FMS-sonic and the Versatile Seismic Imager (VSI) tool strings, so the FMS-sonic was chosen for the second run. By 0850 h, the tool string had been rigged up and run into the hole at a speed of 2500 ft/h to record sonic velocities on the way down. After a difficult exit from the pipe at 201 m WRF, the tool string met with an obstruction at 343 m WRF that could not be passed. After multiple attempts to pass below the obstruction, we decided to begin the first

pass. At 1020 h, the FMS calipers were opened, and a first pass was recorded at a speed of 1000 ft/h between 343 and 235 m WRF. This pass proceeded without additional difficulty, with the exception of an increase in tension between ~291 and 288 m WRF that forced the caliper to be closed. When the tool string was sent down for a second pass, it was not able to reach deeper than 305 m WRF, indicating that the formation was gradually collapsing. The second pass started at 1107 h and was interrupted several times by instances of high wireline tension that required the FMS calipers to be closed. The top of the tool string was brought inside the pipe at 1128 h, but the tool string was raised only ~7 m before high tension indicated that something was impeding its progress. During the following 2 h, efforts to bring the tools back on deck were complicated by the formation apparently closing in on the tool string and the drill pipe. Coordinated pulls on the drill string and on the wireline, along with periods of intense circulation, eventually managed to bring most of the tool string inside the pipe by 1340 h. We then decided to recover the tools using a reverse cut and thread operation, with two T-bars alternately supporting the wirelines while the drill string was tripped back stand by stand. The base of the BHA reached the drill floor at 1750 h, with ~10 m of tool string extending below the bit. Visual inspection immediately confirmed that the two centralizers of the logging string had failed to close properly, likely because formation material had accumulated behind them and prevented their normal collapse. The repeated pull on the wireline during recovery operations eventually bent the centralizers in a way that blocked any further upward motion. The tool string was completely removed from the pipe and rigged down at 1925 h. Further inspection established that no section of the logging string other than the centralizers had suffered any damage.

Data quality

Figures F47, F48, and F49 show a summary of the main logging data recorded in Hole U1353C. These data were converted from the original field records to depth below seafloor and processed to match depths between different logging runs. The resulting depth scale is wireline log matched depth below seafloor (WMSF; see “Downhole logging” in the “Methods” chapter).

The first indicators of the overall quality of the logs are the size and shape of the borehole measured by the calipers. Hole size measured by the HLDS caliper during the triple combo run and by the FMS arms is shown in Figures F47 and F48, respectively. Although both sets of calipers indicate an enlarged and

irregular hole and operations showed that the borehole was gradually collapsing, all calipers maintained mostly good contact with the formation above ~350 m WRF, which suggests that all recorded data should be of good quality. Below this depth, hole size is close to the maximum reach of the HLDS caliper (>17 inches), but the only measurements made (gamma ray and resistivity) are not significantly affected by large hole size. The quality of the resistivity log is indicated by the good overlay between the two resistivity measurements with deep and medium depths of penetration into the formation (Fig. F47).

The reliability of the logs can also be assessed by comparing logging data with core measurements from the same site. Figure F47 shows a comparison of the gamma ray log with NGR track data measured on cores recovered from Hole U1353B, indicating good agreement between the two data sets, particularly in the identification of sand-rich intervals with lower gamma ray readings.

The clear arrivals in the acoustic logging waveforms and the high coherence indicated by distinct red areas in the V_p and V_s tracks in Figure F48 show that the Dipole Sonic Imager (DSI) was able to measure reliable V_p and V_s values. Additional postcruise processing will refine these profiles and characterize some of the high-coherence events that were not labeled automatically at the time of acquisition.

Porosity and density estimation from the resistivity log

In order to provide a measure of porosity and density from the logs obtained without nuclear sources, we used Archie's (1942) relationship to calculate porosity from the phasor deep induction log (IDPH), which is the log least affected by borehole conditions (Schlumberger, 1989), and combined it with MAD grain density data to derive a density profile. Archie (1942) established an empirical relationship between porosity (ϕ), formation resistivity (R), and pore water resistivity (R_w) in sandy formations:

$$\phi = (aR_w/R)^{1/m},$$

where m and a are two empirical parameters that are often called cementation and tortuosity (or Archie) coefficients, respectively. The resistivity of seawater (R_w) was calculated as a function of temperature and salinity, as described by Fofonoff (1985). Pore water salinity was assumed to be 34 ppt (or 3.4%; see "Geochemistry and microbiology"), and temperature was assumed to follow a local linear gradient of 40°C/km, as suggested by in situ measurements at

Site U1352 (see "Heat flow" in the "Site U1352" chapter) and in the Clipper-1 well (Shell BP Todd, 1984). The most realistic value for the cementation coefficient is $a = 1$ because this gives a resistivity equal to formation water resistivity when porosity is 100%. A value of $m = 1.9$ was chosen iteratively to provide the best baseline match with MAD porosity data. Although Archie's relationship was originally defined for sand-rich formations, Jarrard et al. (1989) showed that the effect of clay minerals is moderate, and the relationship is commonly used to estimate porosity in clay-rich formations with poor borehole conditions (Collett, 1998; Jarrard et al., 1989). The resulting porosity log is shown in Figure F47, where it compares well with MAD porosity data. Using MAD grain density, we used this resistivity-derived porosity to calculate a new density curve, which is in good agreement with core measurements (Fig. F47).

Logging stratigraphy

The combined analysis of gamma ray spectroscopy, resistivity, and velocity logs allows for the identification of logging units defined by characteristic trends. Because the FMS-sonic tool string could not record data deeper than 248 m WMSF, identification of the units is based mainly on gamma ray and resistivity data from the first logging run. The combined analysis of these data allows two logging units to be identified.

Logging Unit 1 (105–260 m WMSF) is characterized by an increasing trend in gamma ray from the top of the unit to ~180 m WSF, followed by a mostly decreasing trend to the base of the unit. The similarity between the total gamma ray and the potassium and thorium curves suggests that the increase in total gamma ray is related to variations in mineralogy (Fig. F49). These trends are interrupted by intervals of low gamma ray and high resistivity and velocity that are interpreted as sandy intervals, some of which coincide with actual recovery of sand or even gravel from the same depths in Hole U1353B. Figure F48 shows that some of these intervals are several meters thick (particularly 178–185 and 202–208 m WMSF) with very high velocity values and should be associated with significant seismic reflectors (see "Log-seismic correlation"). The trends and variability in this unit are very similar to those observed at an equivalent depth range in the logs recorded at Site U1351, seaward of this site.

Logging Unit 2 (260–528 m WMSF) is characterized by generally decreasing trends with depth in gamma ray and resistivity, with only limited variability. The top of this unit is also the approximate depth at which core recovery became very low and the FMS-sonic tool string was prevented from going deeper,

indicating a change in the general fabric of the formation.

Core-log correlation

Because Hole U1353C was drilled without coring as a dedicated logging hole, a direct comparison between FMS images recorded in Hole U1353C and core images from Hole U1353B is not possible. However, the proximity of the two holes and the assumption of a flat stratigraphy allow for identification in the electrical images of several features from the cores and from the intervals not recovered.

Figure F50 shows some examples of the diversity of structures at Site U1353. The bottom of lithologic Unit I at ~150 m CSF-A was chosen at a burrowed unconformity at 151.36 m CSF-A (see “**Lithostratigraphy**”) that coincides in Figure F50A with the bottom of a folded or dipping structure in the FMS images. The speckled nature of the FMS images in Figure F50B suggests that at least some of the gravel recovered in Core 317-U1353B-36H was in situ. The fine layering displayed in Figure F50C shows a series of thin beds (a few centimeters thick) that were not recovered below one of the thick sandy intervals that characterize logging Unit 1.

Log-seismic correlation

A depth–traveltime relationship can be determined from the sonic logs and used to correlate features in the logs, recorded in the depth domain, with features in the seismic stratigraphy, recorded in the time domain. A synthetic seismogram was constructed for the interval logged with the FMS-sonic tool string in Hole U1353C (105–249 m WMSF) from the sonic log and the density curve calculated from the resistivity log using Archie’s relationship. Figure F51 shows good correspondence between the synthetic waveform and reflections in the seismic line closest to Site U1353. In particular, seismic sequence boundaries U10–U13, interpreted from seismic data (see “**Seismic stratigraphy**” in the “Expedition 317 summary” chapter), are well resolved in the synthetic seismogram and correspond to distinct features in the sonic, calculated density, and gamma ray logs. U12, U11, and U10 all have similar log characteristics, falling at relatively abrupt transitions from high gamma ray, lower density, and low velocity below to low gamma ray, higher density, and very high velocity above. Based on the time–depth relationship from the synthetic seismogram, these boundaries correspond to lithologic changes from dominantly muddy sediments below to sand-, shell-, and gravel-dominated sediments above (see “**Lithostratigraphy**”). U13 shows the opposite polarity and has a different expression in the logs, located at

a density low with a relatively low velocity value. This suggests that U13 may have been formed by a different process than U12–U10. Additional post-cruise research will refine these correlations by reprocessing the sonic logs and providing a more detailed synthesis of core-log correlations at this site.

Stratigraphic correlation

Holes U1353A and U1353B were drilled ~20 m from each other, with Hole U1353A being dedicated to whole-round sampling for geochemical analyses. Drilling two holes at Site U1353 provides an opportunity for stratigraphic correlation and possible construction of a spliced stratigraphic record with a common core composite depth below seafloor (CCSF) depth scale (see “**Stratigraphic correlation**” in the “Methods” chapter). MSL and NGR data were used to facilitate the correlation of cores at Site U1353. L* colorimetric values and GRA bulk density measurements were also used to cross-check the validity of depth adjustments. A number of key features in the analyzed data are shared by both holes, allowing correlative ties to be made (Fig. F52). The depths of these features (in CSF-A) are often different between the two holes and require depth shifts of individual and/or multiple cores by as much as 1.36 m. Depth adjustments made to cores at Site U1353 are provided in Table T22. The amount of depth adjustment required demonstrates that the stratigraphic record of both holes is characterized by localized differences in the sedimentation history of the two localities (Fig. F52), although we note that depth shifts made to cores at Site U1353 are not as large as those necessary for correlation at Site U1352.

Two sandy units between 13 and 18 m and 28 and 35 m are the key correlatable features in both holes (Fig. F52). The base of the lower sandy unit at ~35 m CCSF coincides with the base of a core in both holes, and the cores immediately below this depth are associated with shell-hash cave-in. The thickness of the sandy units in both holes is different, and it is possible that ~1.9 m of this unit is missing in Hole U1353A. A tentative correlation for the base of the deeper sand unit was thus made at the base of the cores in both holes, but this required that a correlation tie and corresponding depth adjustment be made in the underlying unit close to the shell-hash drilling disturbance. This correlation is marked with a dashed line in Figure F52.

Other anomalous values in both MSL and NGR data (abrupt increases in MSL values and decreases in NGR values), particularly below 37 m, occur as a result of drilling disturbance (i.e., shell-hash cave-in) and likely edge effects, and these features were not

used to aid in correlation. The necessary depth adjustments made to the cores in both holes meant that the core ends and associated artifacts in each hole aligned with each other, and thus it was not possible to remove these intervals during the creation of a spliced record. Indeed, analysis of the composite depth records of both NGR and MSL data for both holes demonstrates that Hole U1353B represents the most relatively complete record and that no part of Hole U1353A is suitable for splicing into the Hole U1353B record to create a composite spliced record for Site U1353.

References

- Abbott, S.T., Naish, T.R., Carter, R.M., and Pillans, B.J., 2005. Sequence stratigraphy of the Nukumaruan strato-type (Pliocene–Pleistocene, c. 2.08–1.63 Ma), Wanganui Basin, New Zealand. *J. R. Soc. N. Z.*, 35(1–2):123–150. [doi:10.1080/03014223.2005.9517779](https://doi.org/10.1080/03014223.2005.9517779)
- Archie, G.E., 1942. The electrical resistivity log as an aid in determining some reservoir characteristics. *J. Pet. Technol.*, 5:1–8.
- Bond, G.C., and Kominz, M.A., 1984. Construction of tectonic subsidence curves for the early Paleozoic miogeocline, southern Canadian Rocky Mountains: implications for subsidence mechanisms, age of breakup, and crustal thinning. *Geol. Soc. Am. Bull.*, 95(2):155–173. [doi:10.1130/0016-7606\(1984\)95<155:COTSCF>2.0.CO;2](https://doi.org/10.1130/0016-7606(1984)95<155:COTSCF>2.0.CO;2)
- Browne, G.H., and Naish, T.R., 2003. Facies development and sequence architecture of a late Quaternary fluvial-marine transition, Canterbury Plains and shelf, New Zealand: implications for forced regressive deposits. *Sediment. Geol.*, 158(1–2):57–86. [doi:10.1016/S0037-0738\(02\)00258-0](https://doi.org/10.1016/S0037-0738(02)00258-0)
- Carter, R.M., 2007. The role of intermediate currents in continental shelf-slope accretion: Canterbury Drifts, SW Pacific Ocean. In Viana, A.R., and Rebesco, M. (Eds.), *Economic and Paleooceanographic Significance of Contourite Deposits*. *Geol. Soc. Spec. Publ.*, 276(1):129–154. [doi:10.1144/GSL.SP.2007.276.01.07](https://doi.org/10.1144/GSL.SP.2007.276.01.07)
- Collett, T.S., 1998. Well log evaluation of gas hydrate saturations. *Trans. SPWLA Annu. Logging Symp.*, 39:MM.
- Fofonoff, N.P., 1985. Physical properties of seawater: a new salinity scale and equation of state for seawater. *J. Geophys. Res.*, [Oceans], 90(C2):3332–3342. [doi:10.1029/JC090iC02p03332](https://doi.org/10.1029/JC090iC02p03332)
- Hayward, B.W., Grenfell, H.R., Reid, C.M., and Hayward, K.A., 1999. Recent New Zealand benthic foraminifera: taxonomy, ecologic distribution, biogeography, and use in paleoenvironmental assessment. *N. Z. Geol. Surv. Bull.*, 75:1–258.
- Herzer, R.H., 1981. Late Quaternary stratigraphy and sedimentation of the Canterbury continental shelf, New Zealand. *N. Z. Oceanogr. Inst. Mem.*, 89:1–71.
- Jarrard, R.D., Dadey, K.A., and Busch, W.H., 1989. Velocity and density of sediments of Eirik Ridge, Labrador Sea: control by porosity and mineralogy. In Srivastava, S.P., Arthur, M.A., Clement, B., et al., *Proc. ODP, Sci. Results*, 105: College Station, TX (Ocean Drilling Program), 811–835. [doi:10.2973/odp.proc.sr.105.146.1989](https://doi.org/10.2973/odp.proc.sr.105.146.1989)
- Kameo, K., and Bralower, T.J., 2000. Neogene calcareous nannofossil biostratigraphy of Sites 998, 999, and 1000, Caribbean Sea. In Leckie, R.M., Sigurdsson, H., Acton, G.D., and Draper, G. (Eds.), *Proc. ODP, Sci. Results*, 165: College Station, TX (Ocean Drilling Program), 3–17. [doi:10.2973/odp.proc.sr.165.012.2000](https://doi.org/10.2973/odp.proc.sr.165.012.2000)
- Lu, H., and Fulthorpe, C.S., 2004. Controls on sequence stratigraphy of a middle Miocene–Holocene, current-swept, passive margin: offshore Canterbury Basin, New Zealand. *Geol. Soc. Am. Bull.*, 116(11):1345–1366. [doi:10.1130/B2525401.1](https://doi.org/10.1130/B2525401.1)
- Raffi, I., Backman, J., Fornaciari, E., Pälike, H., Rio, D., Lourens, L., and Hilgen, F., 2006. A review of calcareous nannofossil astrobiochronology encompassing the past 25 million years. *Quat. Sci. Rev.*, 25(23–24):3113–3137. [doi:10.1016/j.quascirev.2006.07.007](https://doi.org/10.1016/j.quascirev.2006.07.007)
- Richter, C., Acton, G., Endris, C., and Radsted, M., 2007. Handbook for shipboard paleomagnetists. *ODP Tech. Note*, 34. [doi:10.2973/odp.tn.34.2007](https://doi.org/10.2973/odp.tn.34.2007)
- Schlumberger, 1989. *Log Interpretation Principles/Applications*: Houston (Schlumberger Educ. Serv.), SMP-7017.
- Shell BP Todd, 1984. Drilling completion report, Clipper-1. Offshore Canterbury, South Island, New Zealand. PPL38202. *Min. Econ. Dev. N. Z. Pet. Rep.*, PR1036. <https://data.crownminerals.govt.nz/MEDGUEST/system/mainframe.asp>
- Shipboard Scientific Party, 1999. Site 1119: drift accretion on Canterbury Slope. In Carter, R.M., McCave, I.N., Richter, C., Carter, L., et al., *Proc. ODP, Init. Repts.*, 181: College Station, TX (Ocean Drilling Program), 1–112. [doi:10.2973/odp.proc.ir.181.103.2000](https://doi.org/10.2973/odp.proc.ir.181.103.2000)

Publication: 4 January 2011
MS 317-105



Figure F1. A. Dip Profile EW00-01-66 showing Site U1353. B. Crossing strike Profile EW00-01-01. Red = actual penetration, yellow = proposed penetration. CDP = common depth point. MP = Marshall Paraconformity.

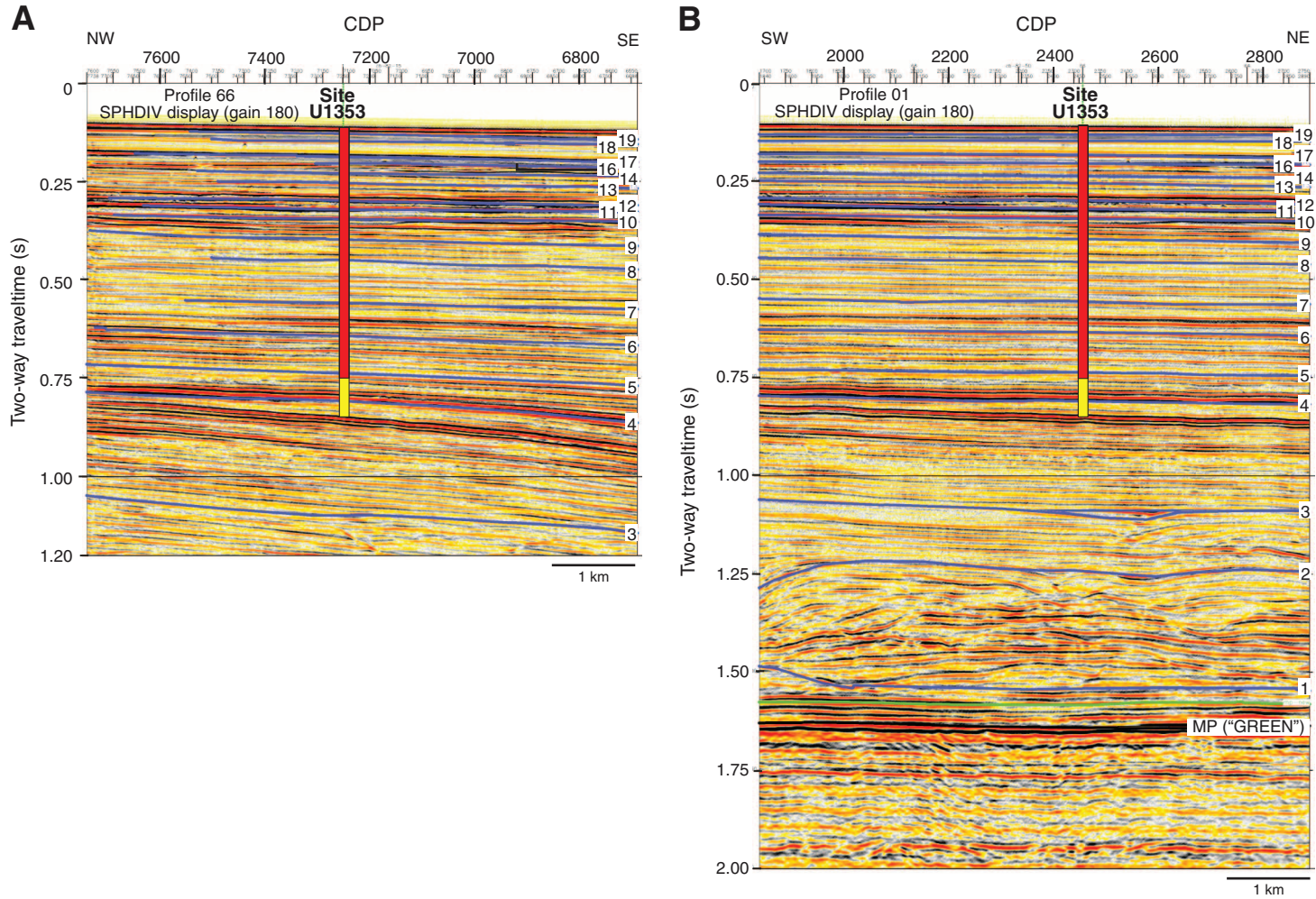


Figure F2. Drilled and proposed Expedition 317 sites, together with EW00-01 high-resolution (frequencies up to 300 Hz) multichannel seismic (MCS) grid (thick straight lines), low-resolution CB-82 commercial MCS grid (thin straight lines), exploration wells Clipper and Resolution, and Ocean Drilling Program (ODP) Site 1119. The EW00-01 survey was designed to provide improved vertical resolution (~5 m in the upper 1 s) to enhance our ability to define high-frequency sedimentary sequences. Also shown is the distribution of seismically resolvable sediment drifts D1–D11, along with D8 and D9 subdrifts. Blue curved lines = crests of drift mounds, dashed blue lines = drifts identified on CB-82 profiles. Dip Profiles EW00-01-66, EW00-01-60, EW00-01-01, EW00-01-07a, and CB-82-25 are also labeled.

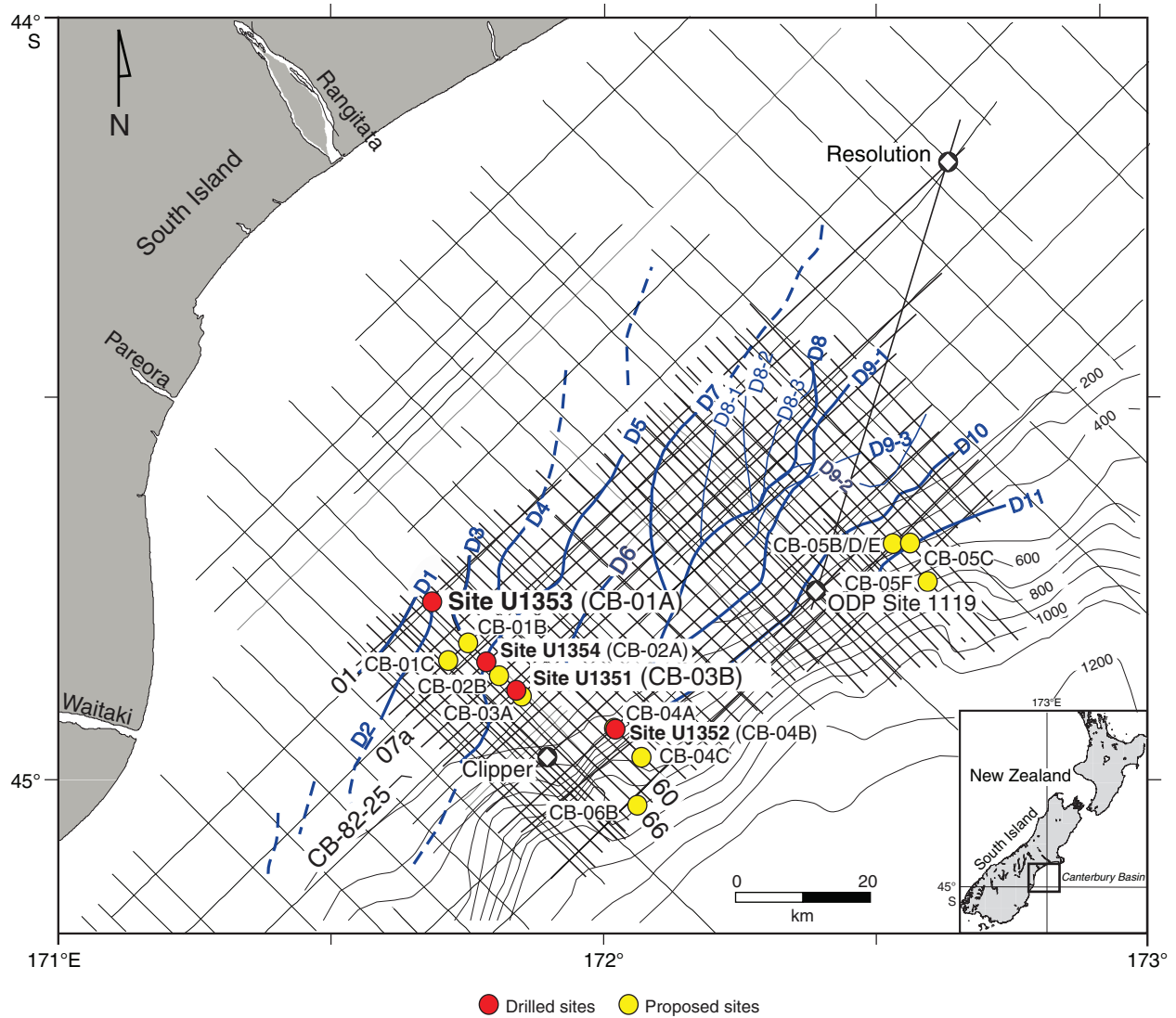


Figure F3. Tentative lithostratigraphic correlation, Holes U1353A and U1353B. Eight correlative lithostratigraphic horizons (connected with gray lines and bands) were selected based on lithology and depth: (1) Holocene dark greenish gray very fine sandy mud/muddy very fine sand (~0–6.30 m in Hole U1353A and ~0–6.40 m in Hole U1353B); (2) muddy sand with shell fragments (~8.95–9.4 m in Hole U1353A and ~8.7–8.95 m in Hole U1353B); (3) ~4 m thick well-sorted very fine sand (~13.95–17.9 m in Hole U1353A and ~12.95–16.9 m in Hole U1353B); (4) sandy mud with common occurrences of fossils, including *Chlamys delicatula*, *Stirocolpus*, and other bivalves and gastropods (~24.3–27.3 m in Hole U1353A and ~24.35–26 m in Hole U1353B); (5) 6.0–7.5 m thick well-sorted very fine sand (28.0–34.1 m in Hole U1353A and ~28.05–35.5 m in Hole U1353B); (6) shelly mud, including *Stirocolpus* and broken gastropods (~39.75 in Hole U1353A and ~39.85 m in Hole U1353B); (7) shelly mud, including *Stirocolpus* and broken gastropods (~45.7 m in Hole U1353A and ~45.2–42.35 m in Hole U1353B); (8) sandy mud with abundant fossils, including *Stirocolpus*, *Tawera*, barnacle plates, and broken shells of gastropods and bivalves (~52.20–53.6 m in Hole U1353A and ~51.95–53.70 m in Hole U1353B).

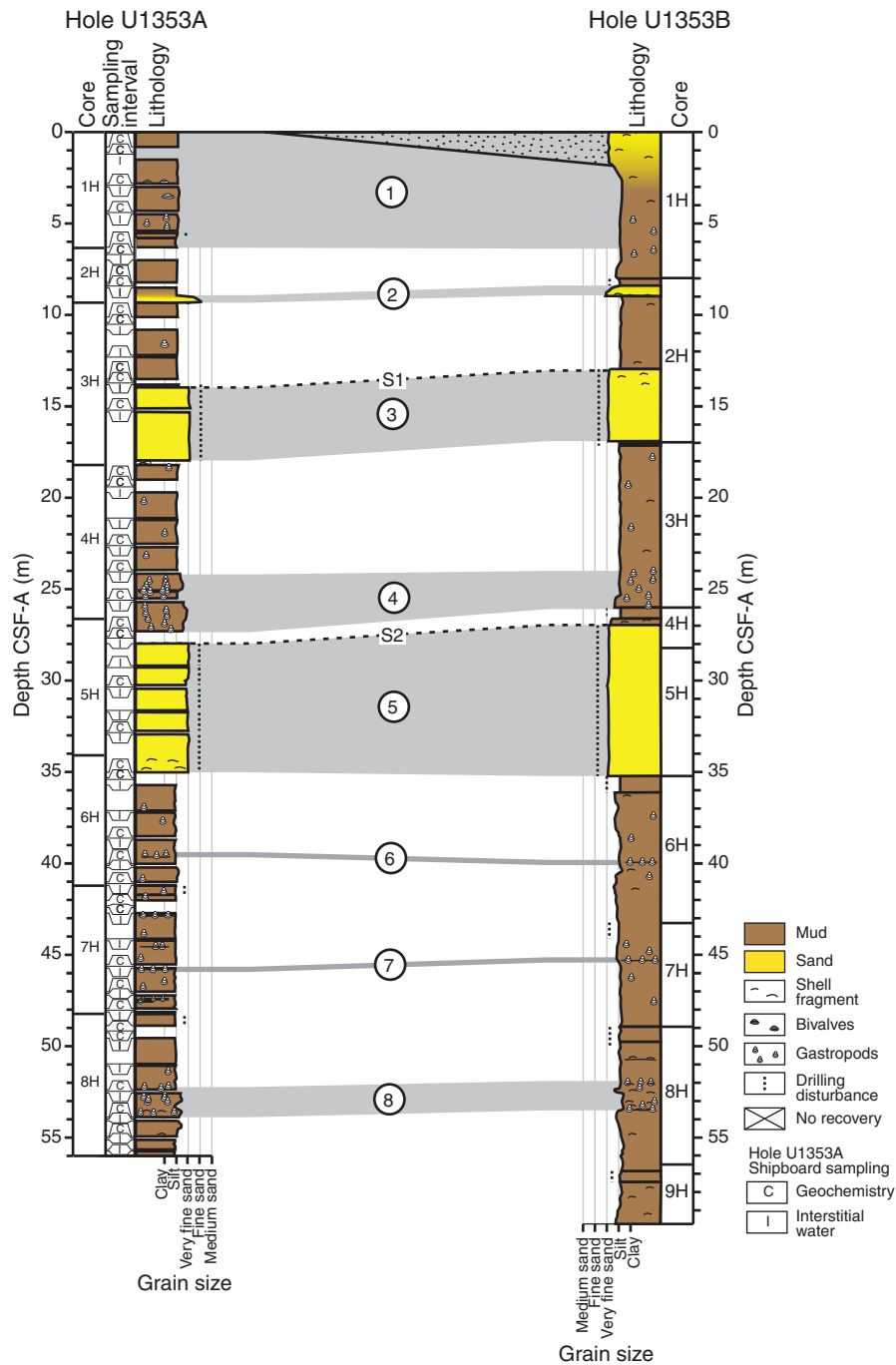


Figure F4. Core photographs of typical lithologies found in the uppermost 60 m of Unit I, Site U1353. A. Homogeneous mud (interval 317-U1353B-3H-3, 0–30 cm). B. Shelly muddy sand (interval 317-U1353B-4H-1, 60–90 cm). C. Shelly sandy mud (interval 317-U1353B-7H-3, 0–30 cm). D. Well-sorted very fine sand with rare shells (interval 317-U1353B-5H-5, 0–30 cm). E. Sandy marl (interval 317-U1353B-1H-4, 0–30 cm). F. Contact between muddy sand above and well-sorted very fine sand below (interval 317-U1353B-2H-4, 35–65 cm). Note that the well-sorted very fine sand (D and lower part of F) is liquefied and structureless.

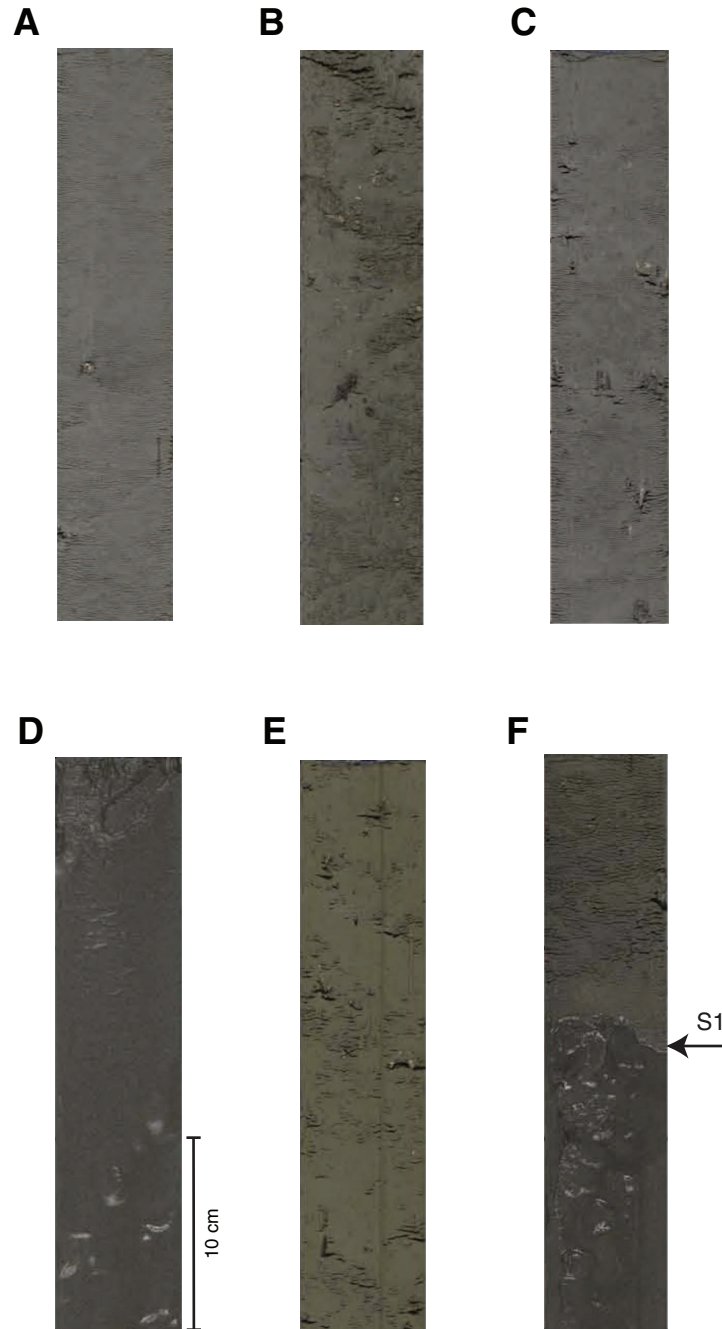


Figure F5. Summary of core recovery, lithology, lithologic units, unit descriptions, physical property data, and gamma ray data from downhole logging, Hole U1353B. NGR = natural gamma radiation. Downhole logging data are plotted on the WMSF depth scale.

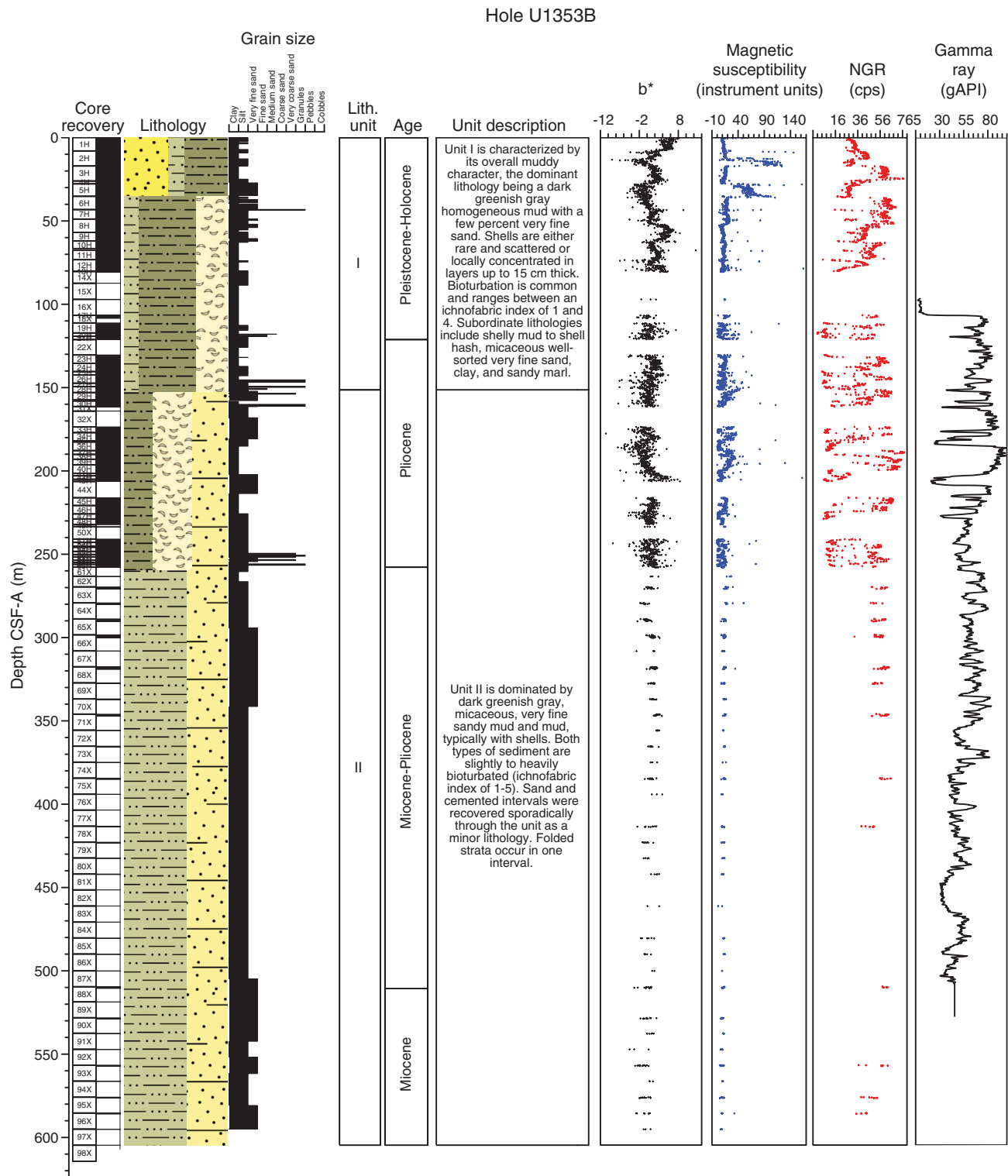


Figure F6. Core recovery and lithology shown as a proportion of the recovered interval (lithology [%] × recovery [%]/100) in Hole U1353B. Depth scale in CSF-A (m) is variable, but for graphical purposes each core is depicted by an equally thick horizontal bar.

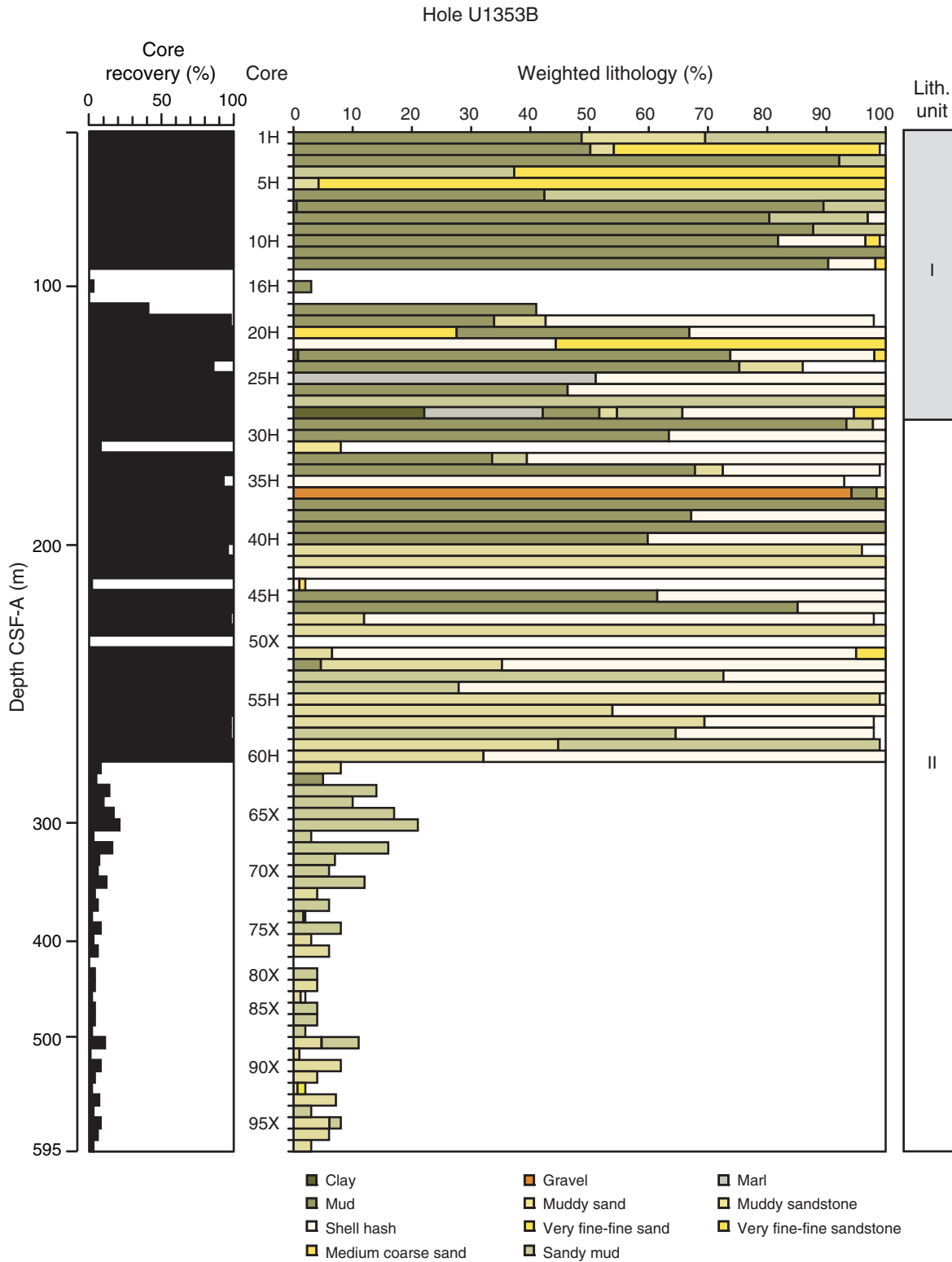


Figure F7. Core photographs of shelly layers thought to be largely cave-in (tops) and flow-in (bases) from drilling disturbance. **A.** Potential in situ shelly layer (interval 317-U1353B-12H-1, 0–60 cm), with disturbed mud below but possibly in situ mud above. **B.** First layer of washed shell material observed, interpreted as cave-in (interval 317-U1353B-17H-CC, 1–18 cm). **C.** Washed shelly material occurring at the top of a core (interval 317-U1353B-19H-1, 34–74 cm). **D.** Washed shelly material occurring at the base of a core (interval 317-U1353B-19H-4, 1–21 cm). **E.** Irregular concretions of sandy shelly limestone occurring within washed shell hash (interval 317-U1353B-36H-2, 91–111 cm). **F.** Large elongate graywacke pebble occurring within washed shell flow-in (interval 317-U1353B-35H-3, 80–110 cm). Smaller quartz pebbles are also present. **G.** Last core in which abundant caved deposits occur (interval 317-U1353B-60H-1, 72–141 cm).

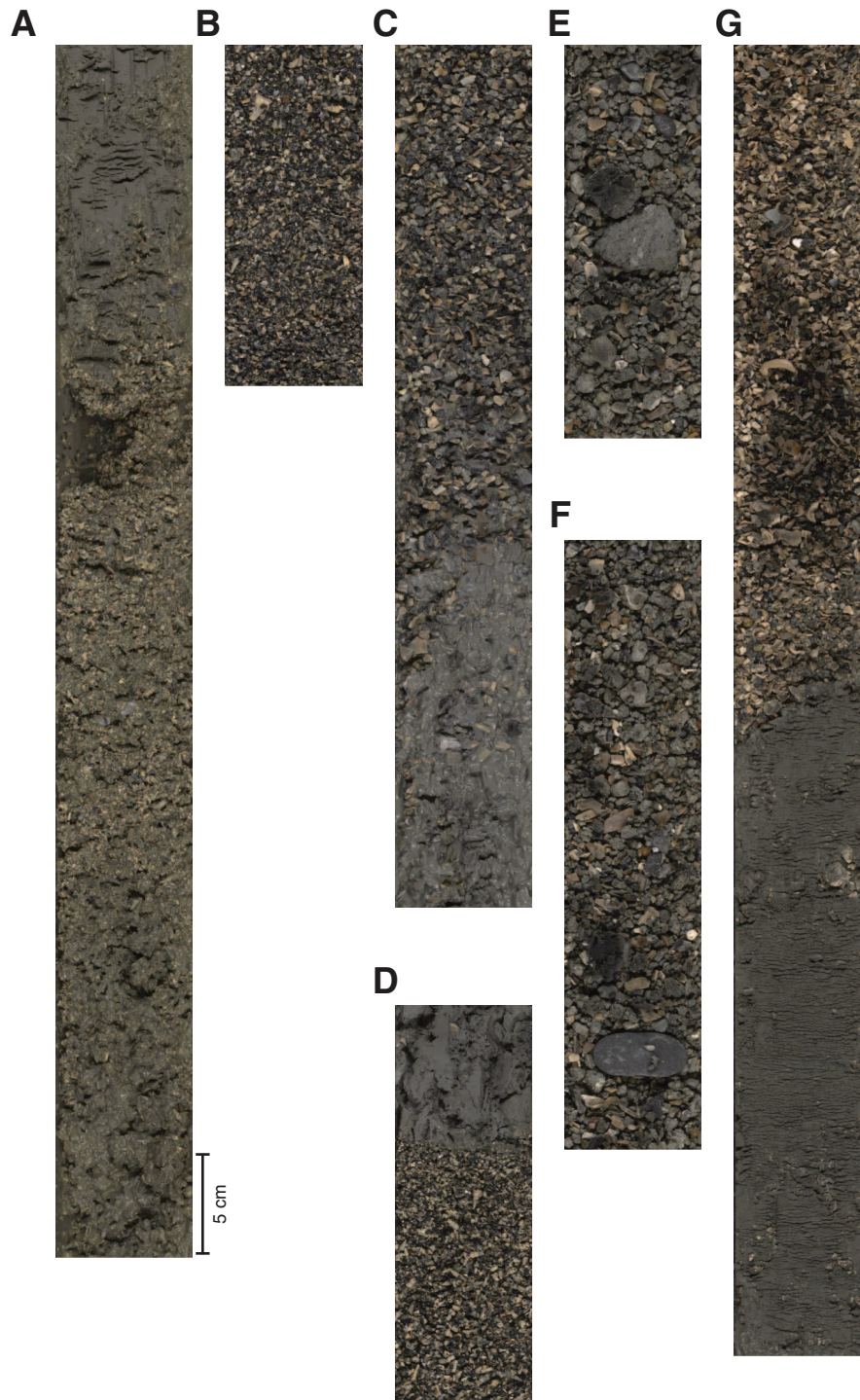


Figure F8. Core photographs of representative lithologies from Unit I in Hole U1353B. **A.** Homogeneous gray mud with rare shell fragments (interval 317-U1353B-10H-2, 80–110 cm). **B.** Core section showing diffuse contact between gray mud overlying green sandy calcareous mud, with scattered shell fragments (interval 317-U1353B-8H-3, 0–80 cm). **C.** Clay-rich calcareous mud (interval 317-U1353B-8H-5, 65–95 cm). **D.** Mud overlain by silty mud with a sharp-based shelly contact (interval 317-U1353B-24H-2, 100–130 cm).





Figure F9. Mineral and component concentrations estimated from smear slide observations, Holes U1353A and U1353B.

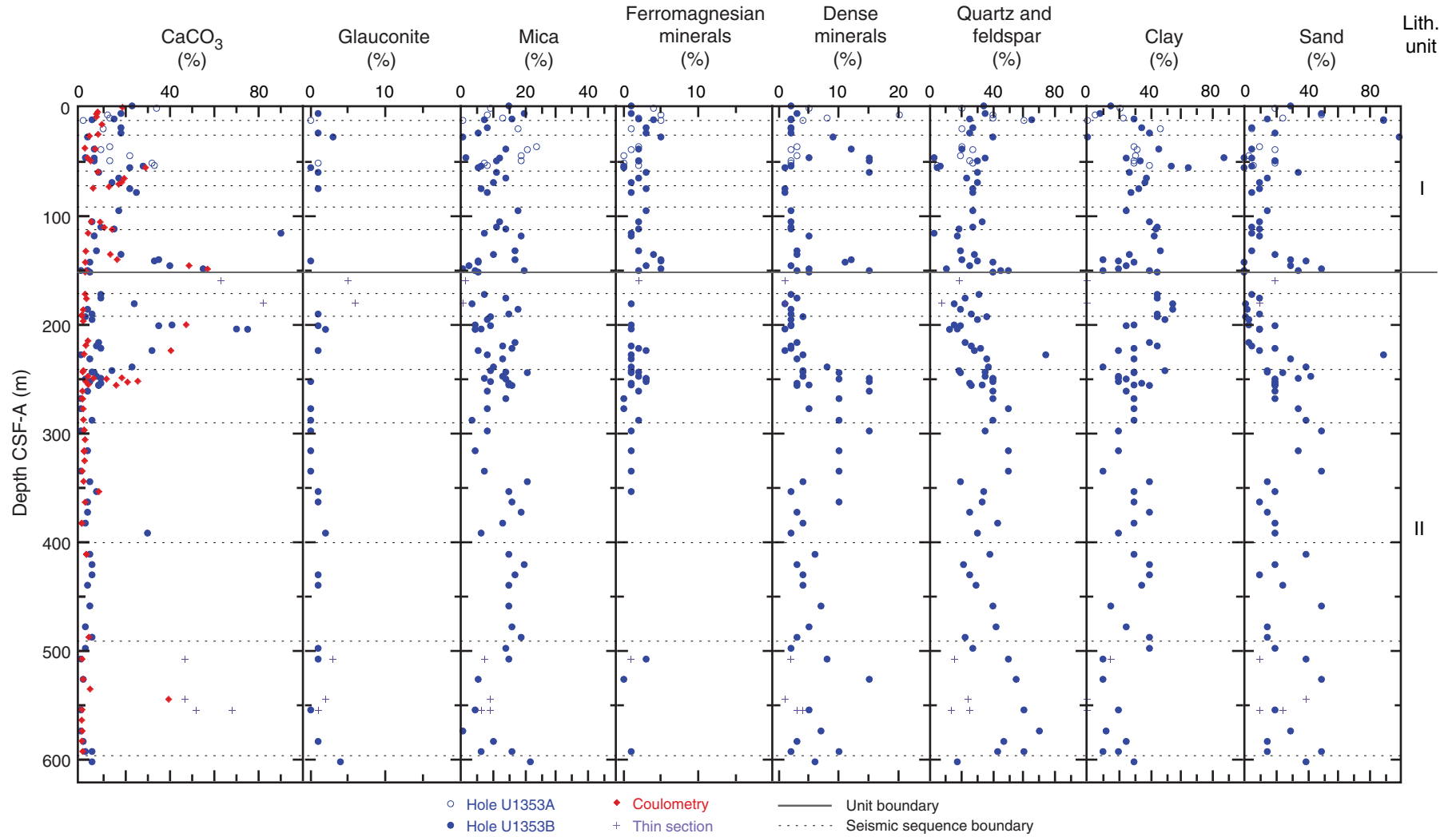




Figure F10. Relative maximum peak intensities in XRD analyses for common minerals, Hole U1353B. CaCO₃ estimates are plotted against data from coulometry analyses for comparison. Horizontal line = Unit I/II boundary (151 m).

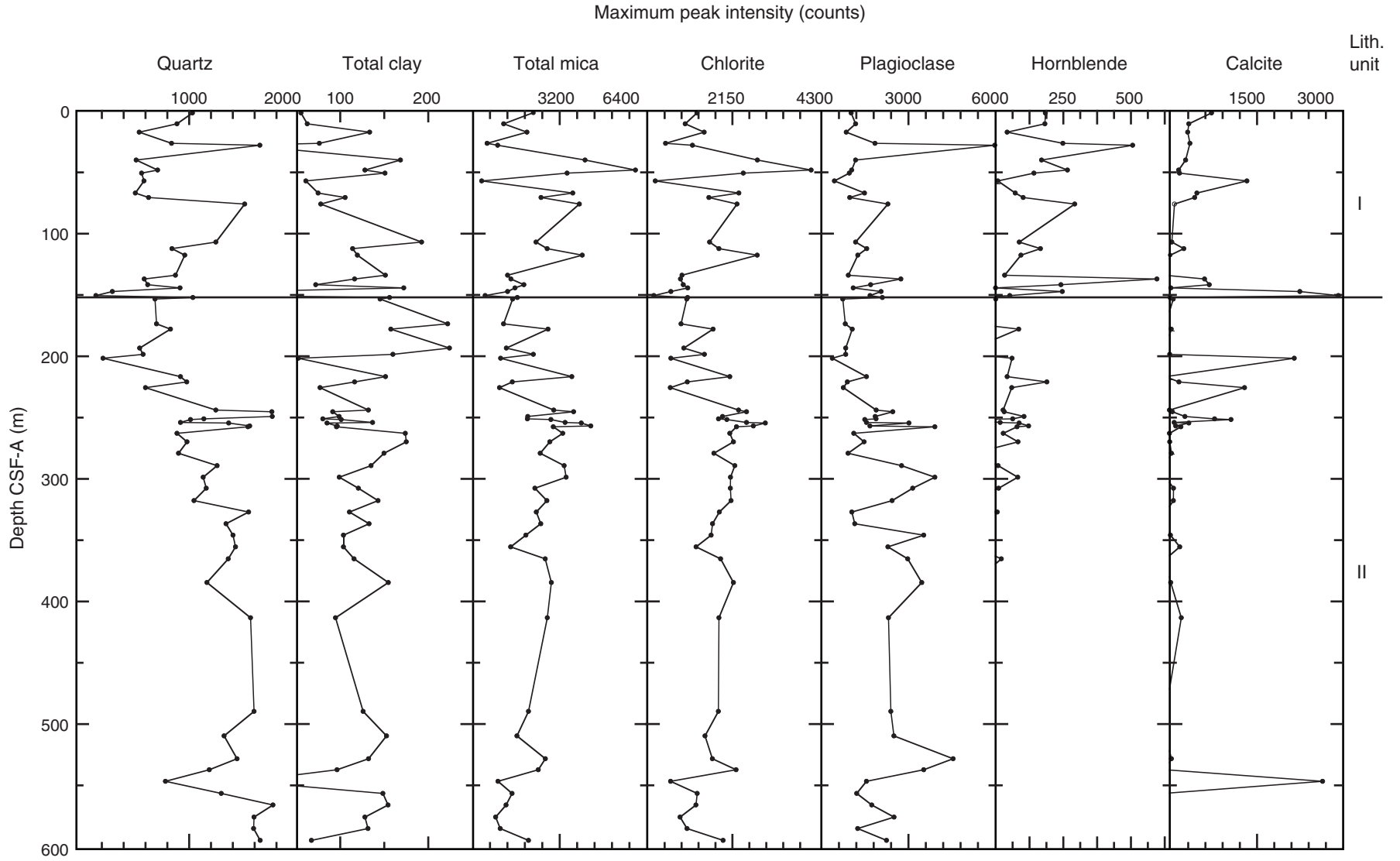


Figure F11. Core photographs showing Unit I/II boundary options. **A.** Option A (preferred) (Section 317-U1353B-28H-2, 46 cm [151.36 m]), where a pronounced burrowed contact is taken to represent the base of Unit I. Burrows at this contact are filled with sandy marl from the overlying lithology and extend 20 cm into the underlying mud. **B.** Option B (Section 317-U1353B-24H-2, 121 cm [137.07 m]), where a silty mud with common shells occurs above a bioturbated mud. **C.** Option C (Section 317-U1353B-34H-2, 32 cm [178.82 m]), where a folded clay-rich muddy interval rests sharply on a muddy shelly fine sand.

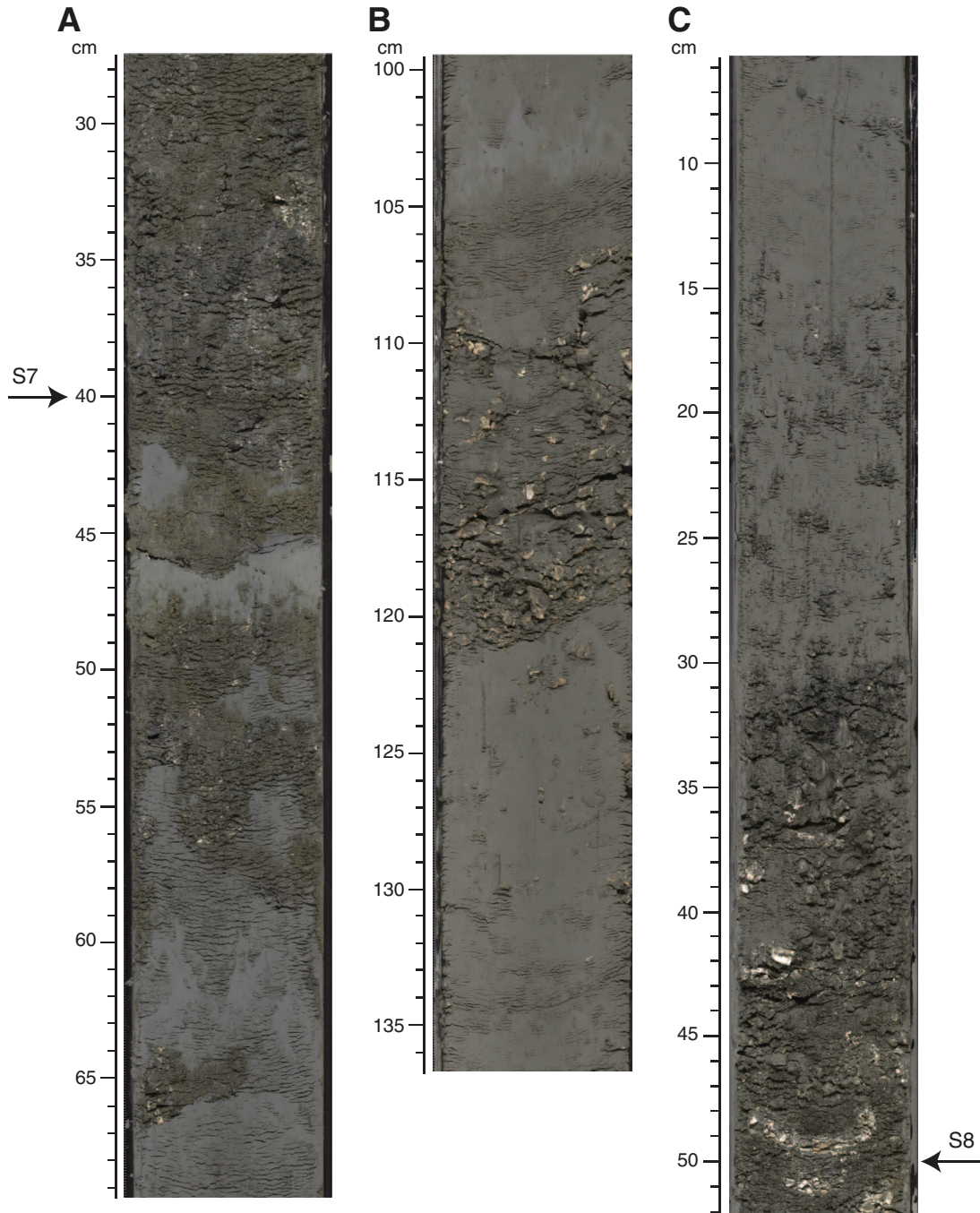


Figure F12. Core photographs of representative lithologies from Unit II, Hole U1353B. **A.** Very fine micaceous sandy mud lacking shells (interval 317-U1353B-63X-1, 20–50 cm). **B.** Moderately sorted, muddy sand with abundant shells (bivalves and scaphopods) and a graywacke clast (interval 317-U1353B-68X-1, 10–40 cm). **C.** Very fine micaceous sandy mud with shells (interval 317-U1353B-56H-1, 80–110 cm). **D.** Muddy sand with cemented nodules (interval 317-U1353B-93X-1, 35–65 cm).

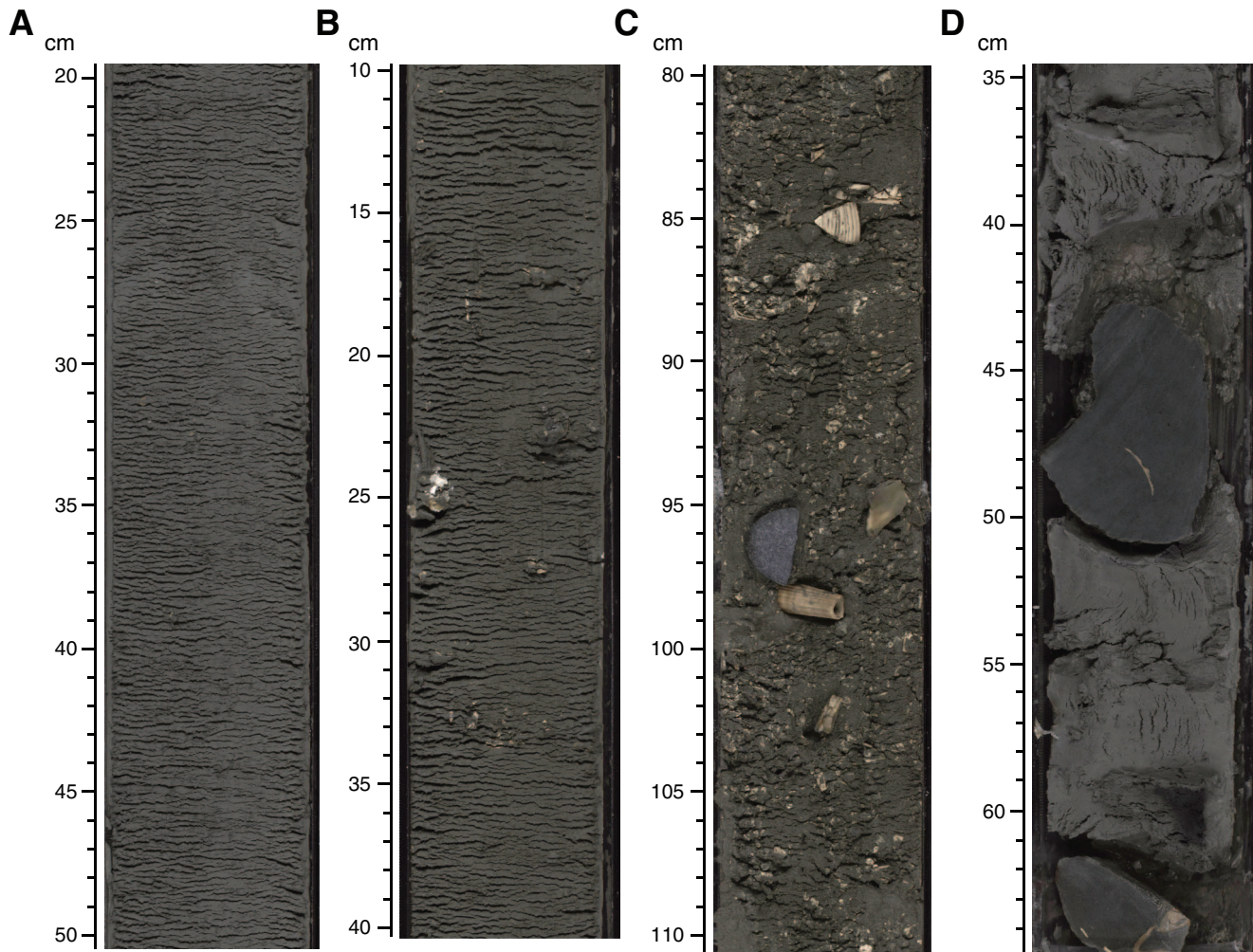


Figure F13. Correlation of computed gamma ray (CGR) logging data from Holes U1353C and U1351B. Dashed lines = tie points between similar features, arrows = potential coarsening- and fining-upward trends.

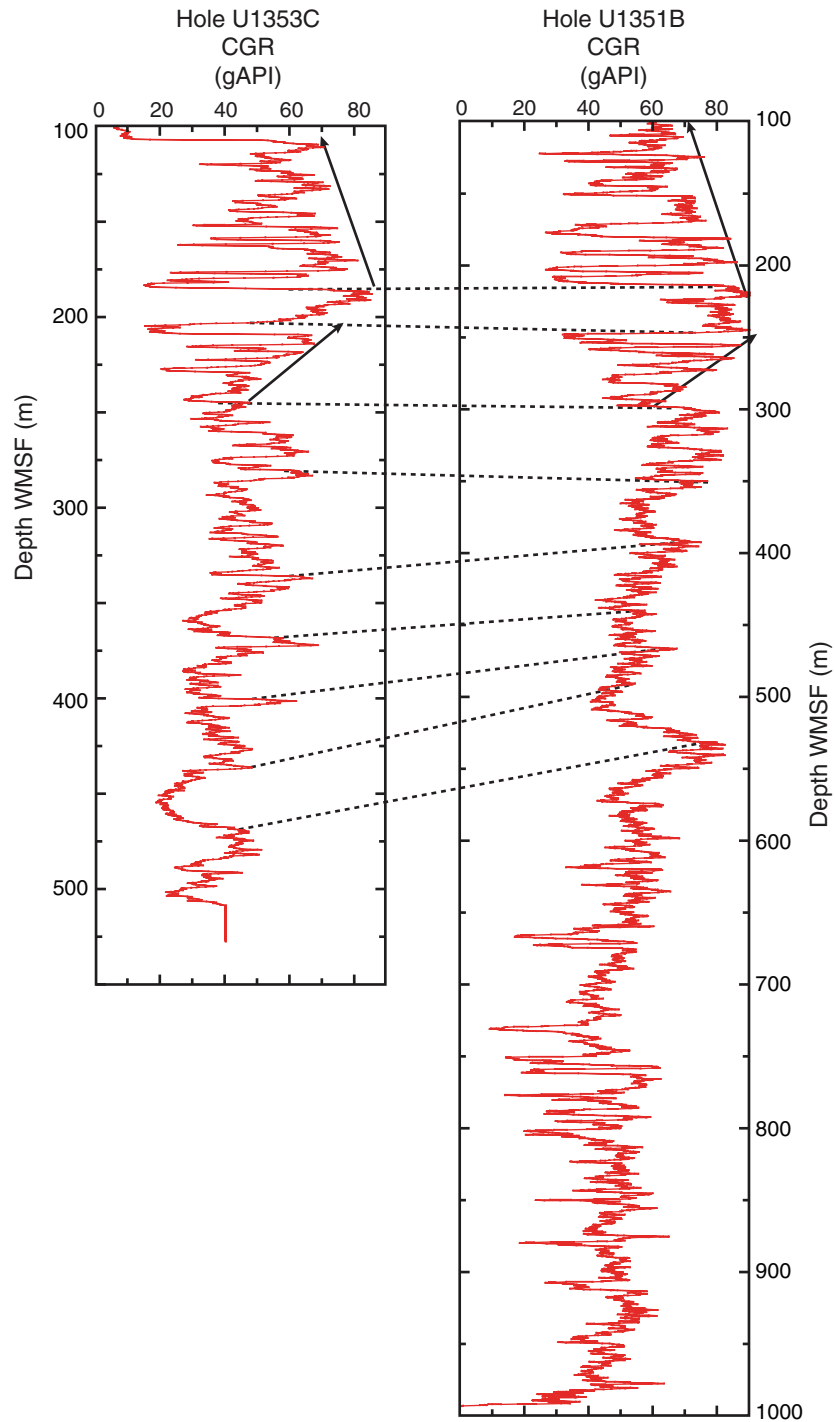


Figure F14. Core photographs showing transition from gray mud into mud with abundant shells and shell fragments of shallow-water origin that characterize the interval from 250 to 254 m (317-U1353B-56H-1, 80–142 cm; 57H-1, 59–100 cm; 57H-2, 28–80 cm; and 58H-1, 45–76 cm). Surface U1353B-S10 is tentatively placed between a gray mud and shelly mud at Section 317-U1353B-57H-1, 99 cm.

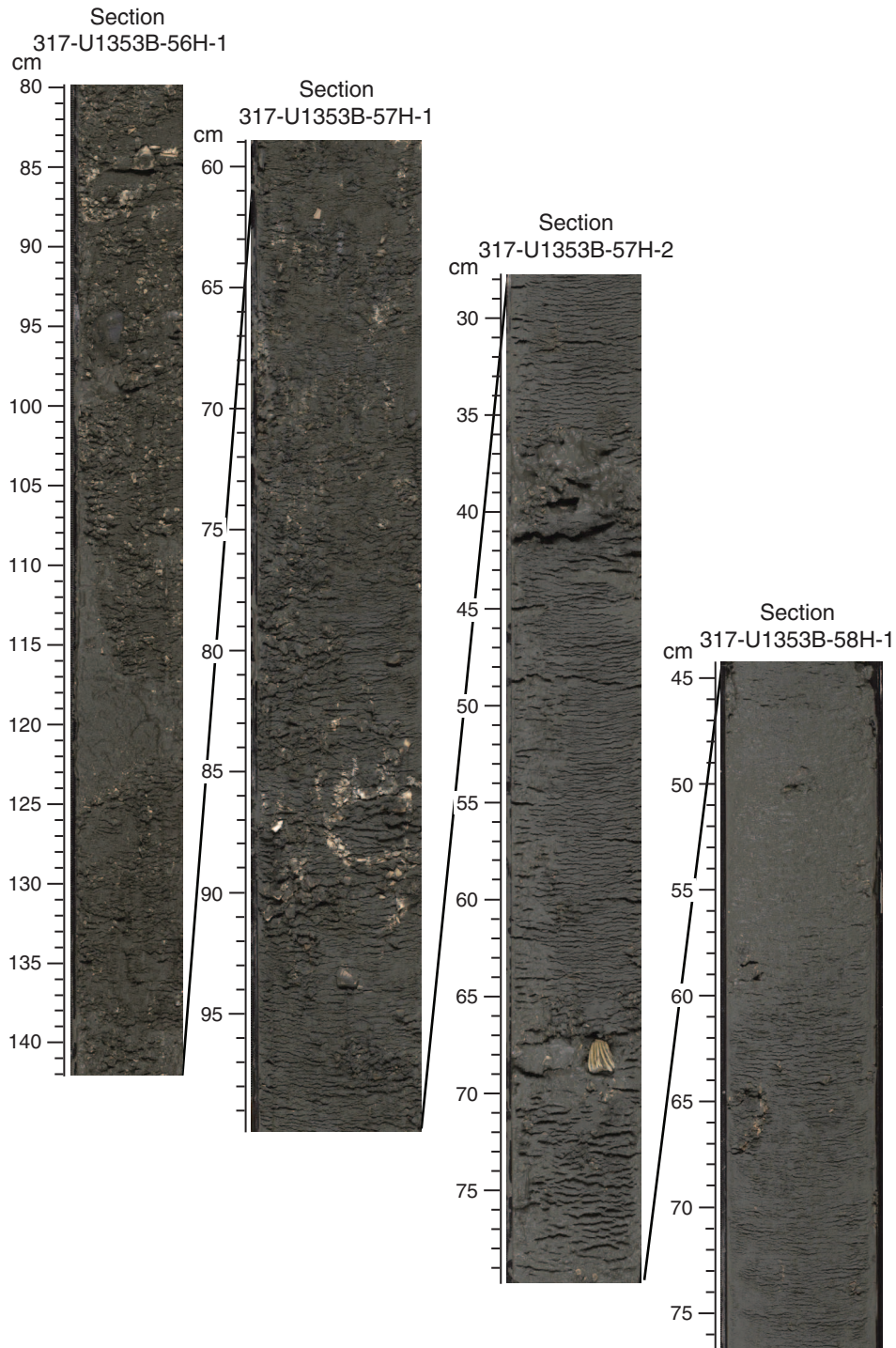


Figure F15. Core recovery, epochs, calcareous nannofossil (NN) zones, and New Zealand (NZ) stage correlation for planktonic foraminifers and bolboforms (PF) and benthic foraminifers (BF), Site U1353. Solid wavy lines = hiatuses between biozones, dashed wavy lines = hiatuses within biozones. ND = not determined. See Figure F6 in the “Methods” chapter for NZ stage abbreviations.

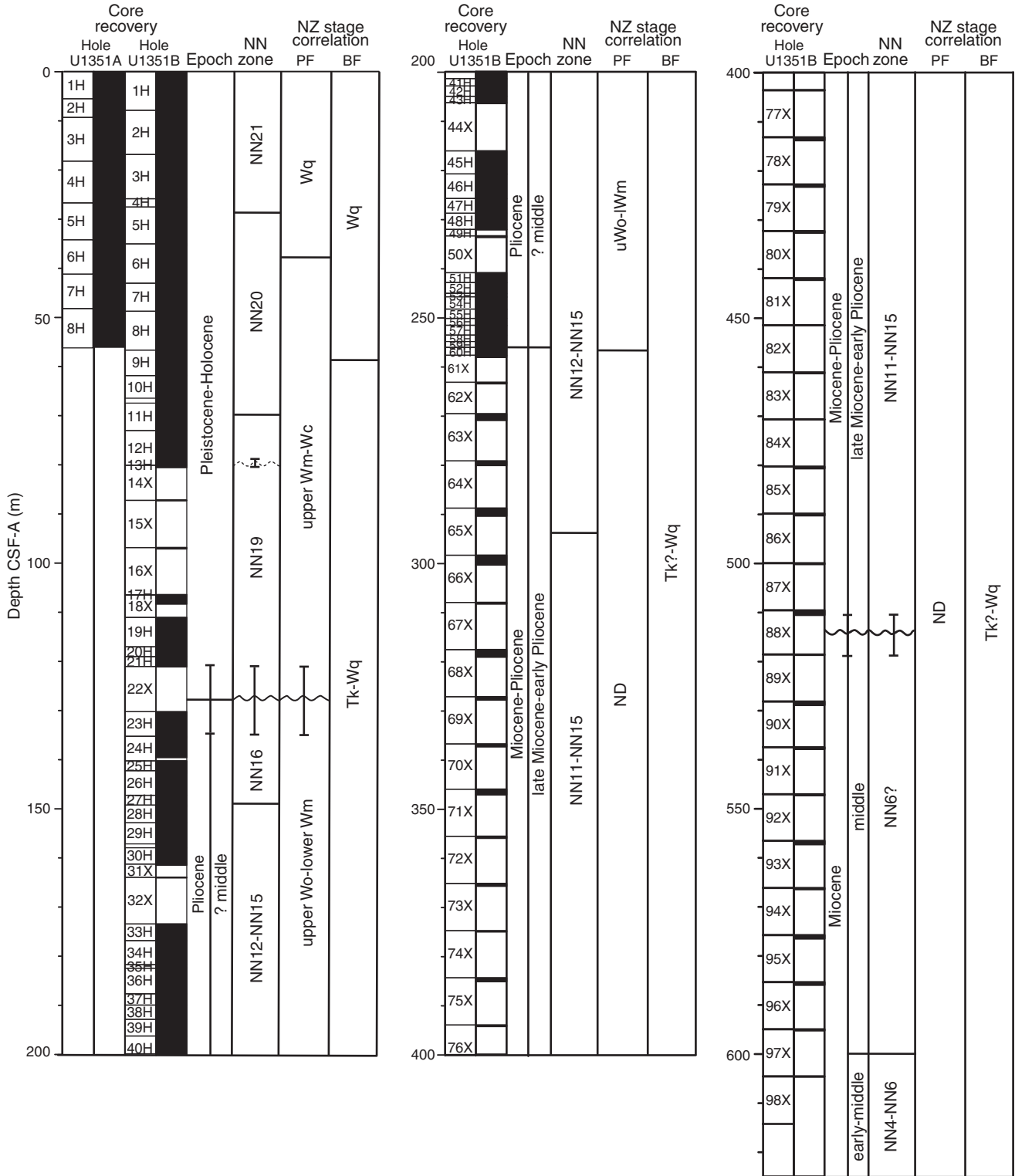


Figure F16. Planktonic foraminiferal abundance relative to total foraminifers and oceanicity, Site U1353. See Figure F7 in the “Methods” chapter.

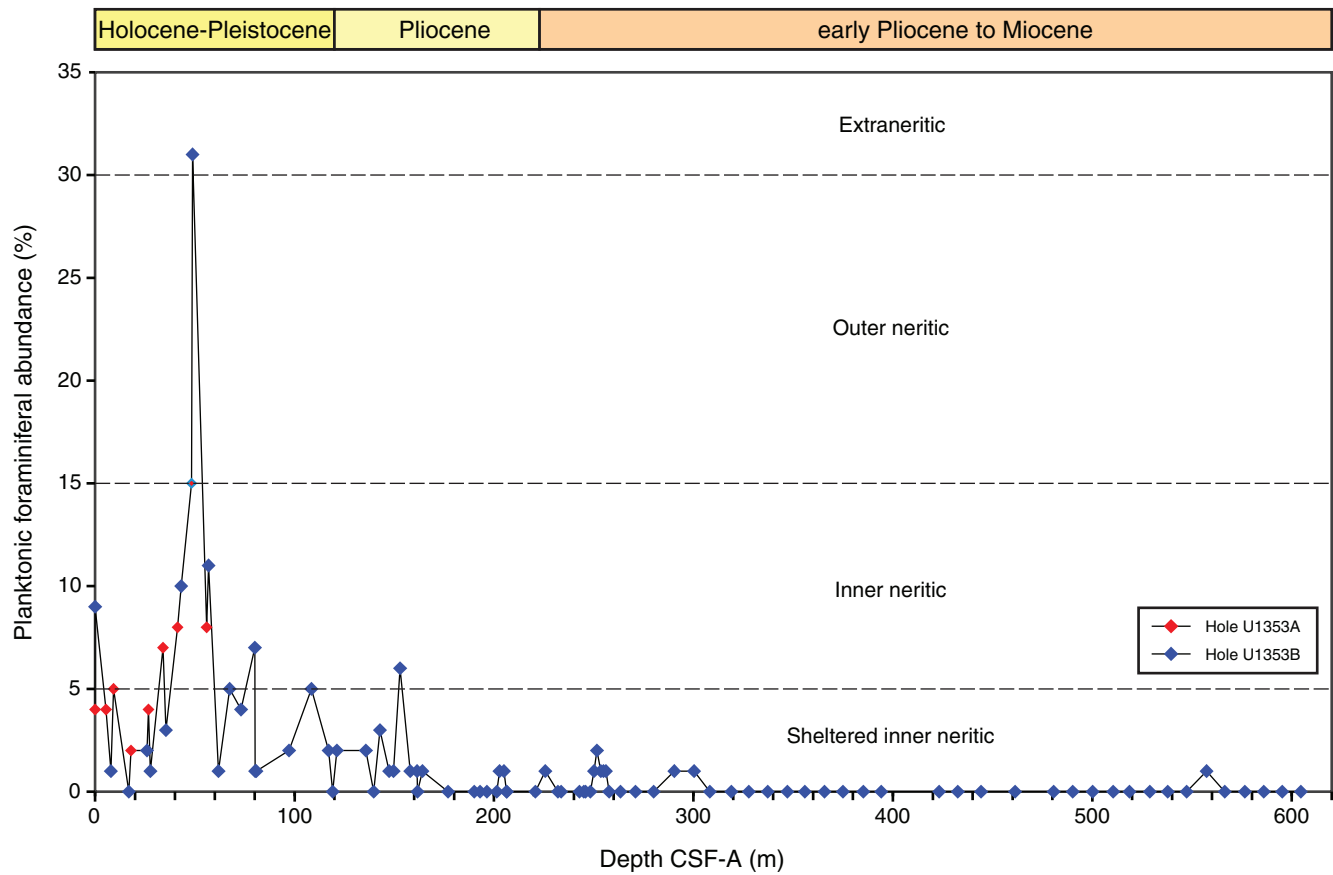


Figure F17. Paleodepth interpretation from benthic foraminifers, Site U1353.

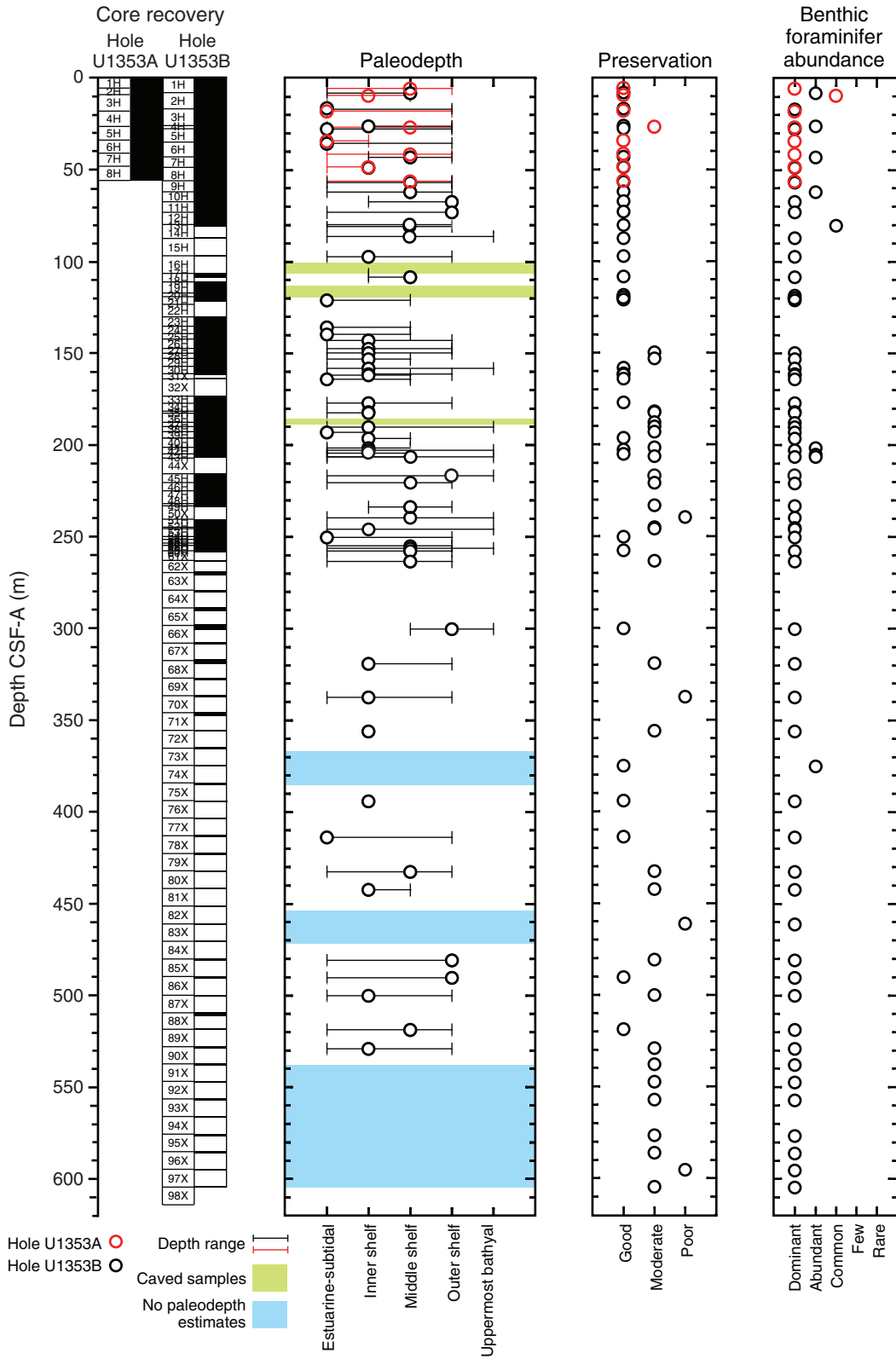


Figure F18. Natural remanent magnetization (NRM) paleomagnetic record, Hole U1353B. Whole-round magnetic susceptibility (loop sensor) is also shown. Horizontal shaded bars indicate distinct thick sand layers with high magnetic susceptibility. Solid horizontal line indicates a change in coring system. APC = advanced piston corer, XCB = extended core barrel.

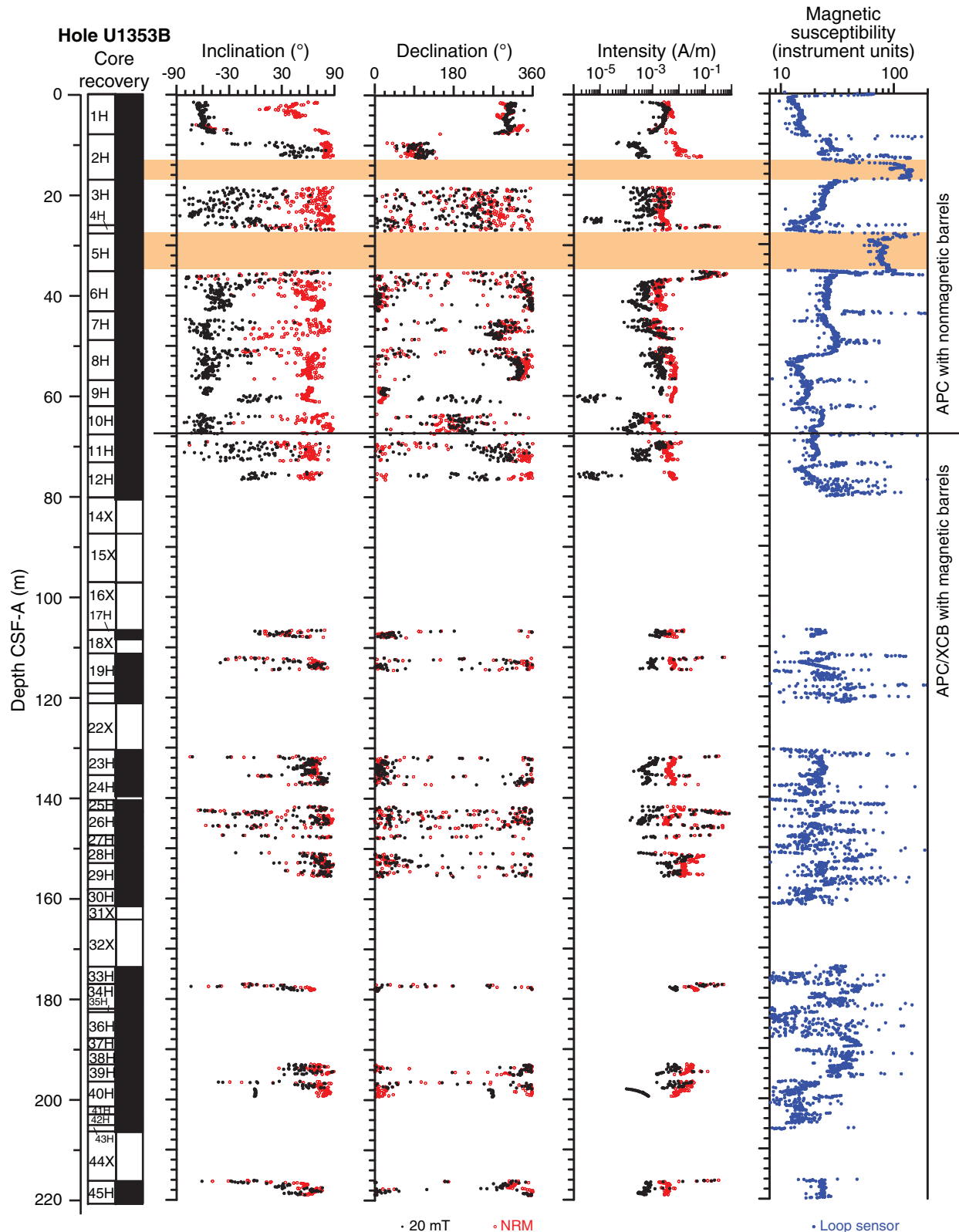


Figure F19. Comparison of natural remanent magnetization orientation before (NRM) and after (20 mT) peak field AF demagnetization. **A.** Nonmagnetic core barrels. **B.** Standard (magnetic) core barrels. Red circles = positive downward orientations, open circles = negative upward directions. Histograms show inclination in 10° bins. Note that these cores were not oriented with the Flexit tool. APC = advanced piston corer.

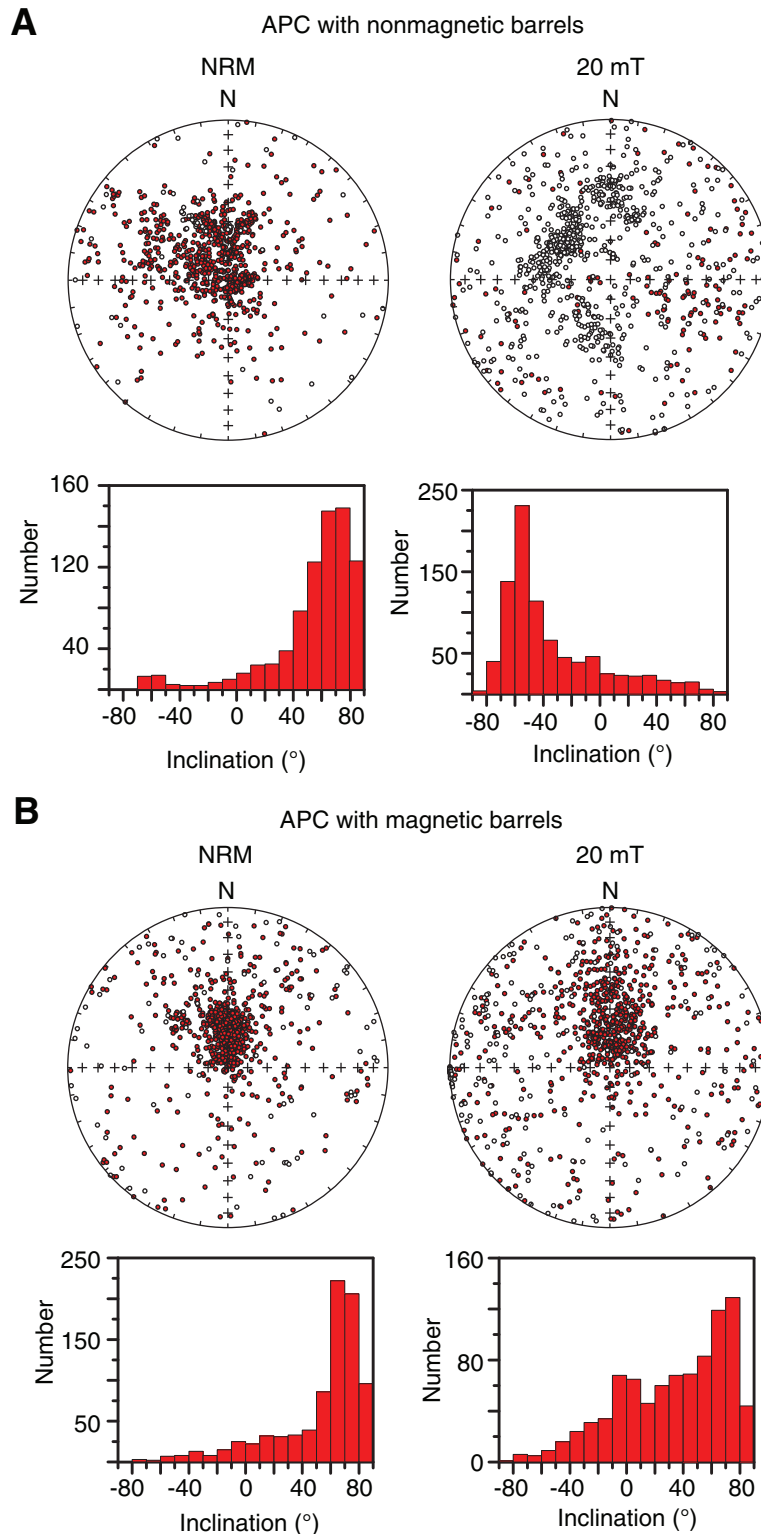


Figure F20. Orthogonal AF demagnetization plots of samples from Hole U1353B. White circles = projection on the vertical plane, black circles = projection on the horizontal plane. NRM = natural remanent magnetization. **A.** Sample 317-U1353B-1H-3, 107 cm (4.07 m). **B.** Sample 317-U1353B-2H-2, 96 cm (10.85 m). **C.** Sample 317-U1353B-12H-3, 23 cm (75.41 m). **D.** Sample 317-U1353B-28H-3, 18 cm (152.38 m).

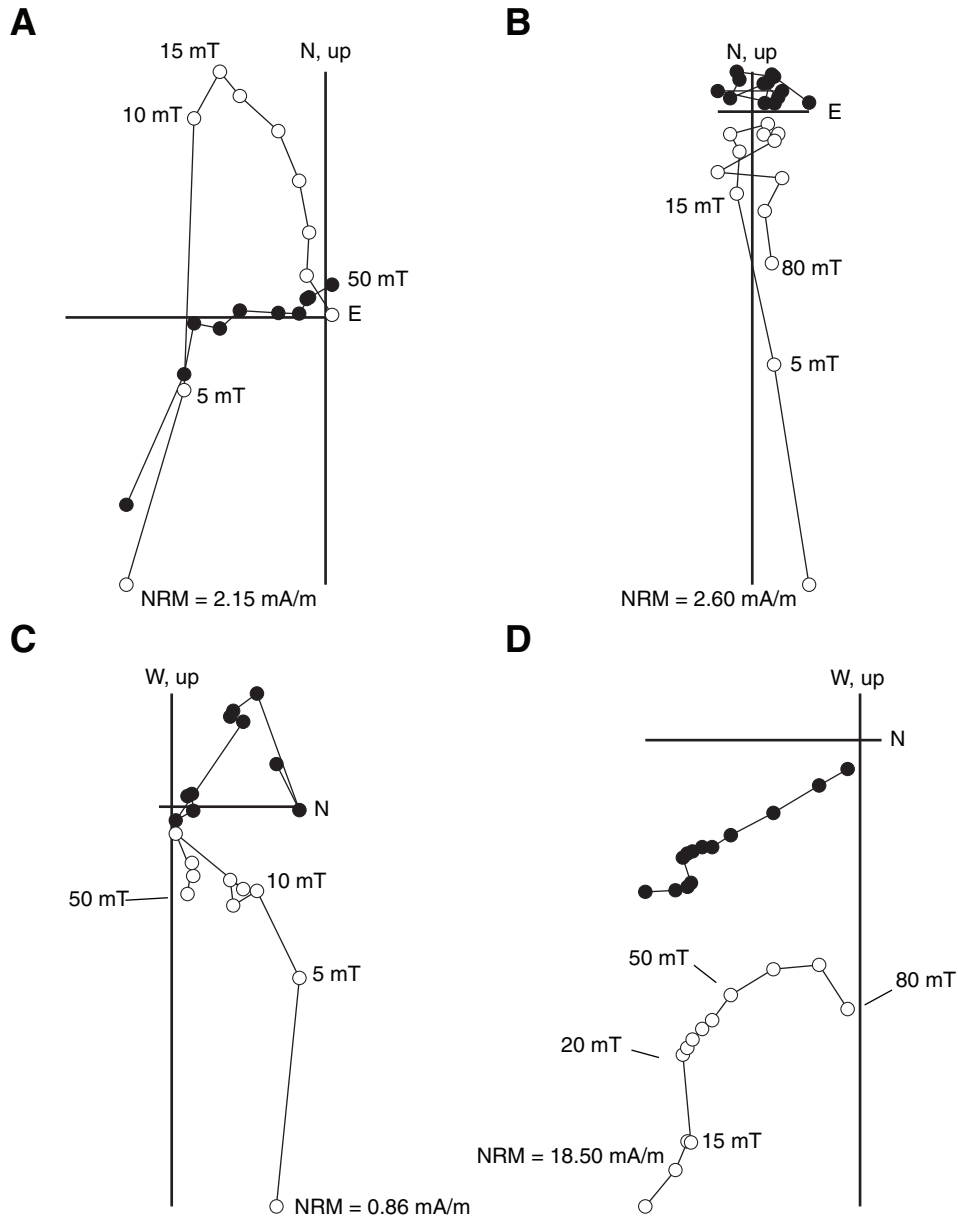


Figure F21. IRM and backfield acquisition curves for 10 discrete samples from Hole U1353B. Samples reach saturation between 400 and 600 mT, and coercivity of remanence (B_{cr}) ranges between 40 and 80 mT.

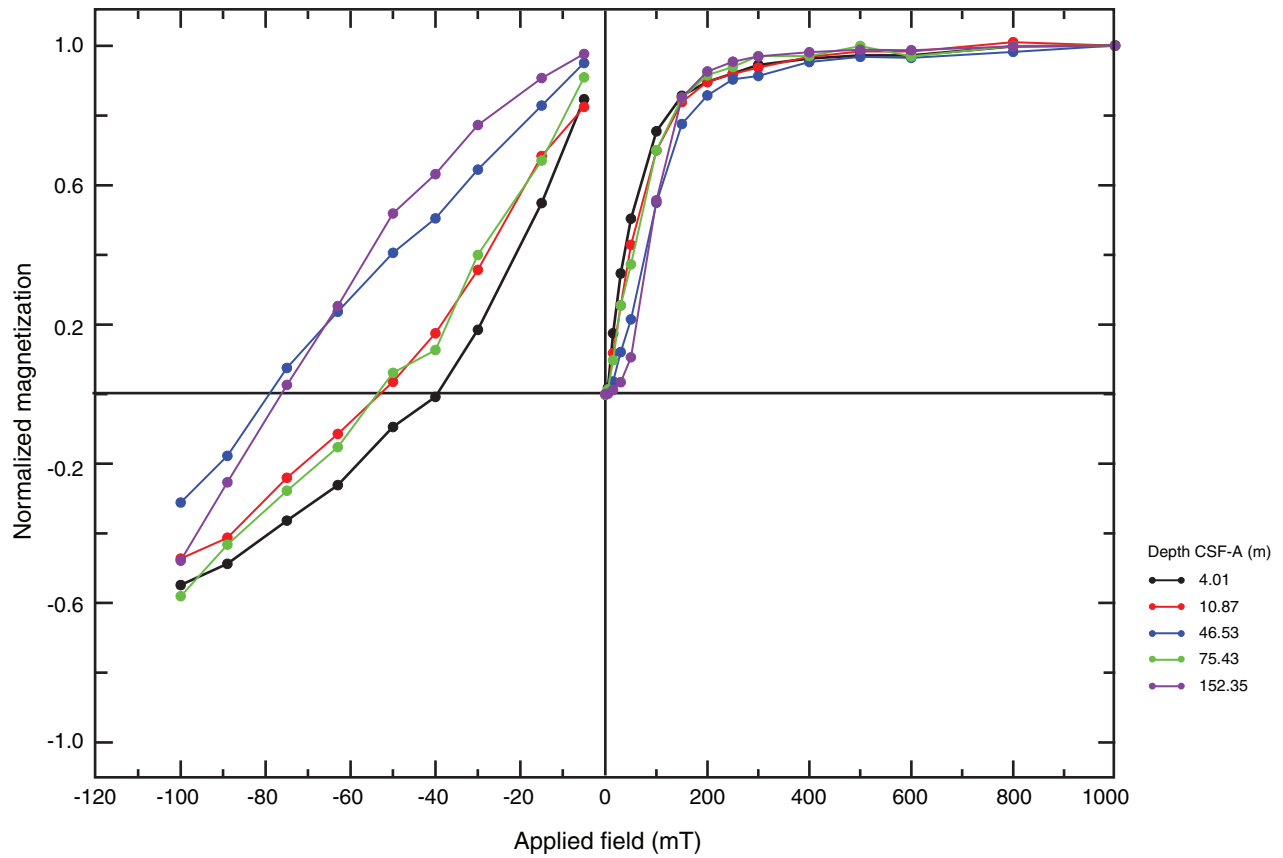


Figure F22. A. AF demagnetization of isothermal remanent magnetization (IRM) at 1 T for samples from Hole U1353B. B. Same as A but with intensities normalized to IRM at 1 T. C. Thermal demagnetization of IRM at 1 T for samples from Hole U1353B. D. Same as C but with intensities normalized to IRM at 1 T. E. Photograph of the measured cubes showing color differences related to lithology.

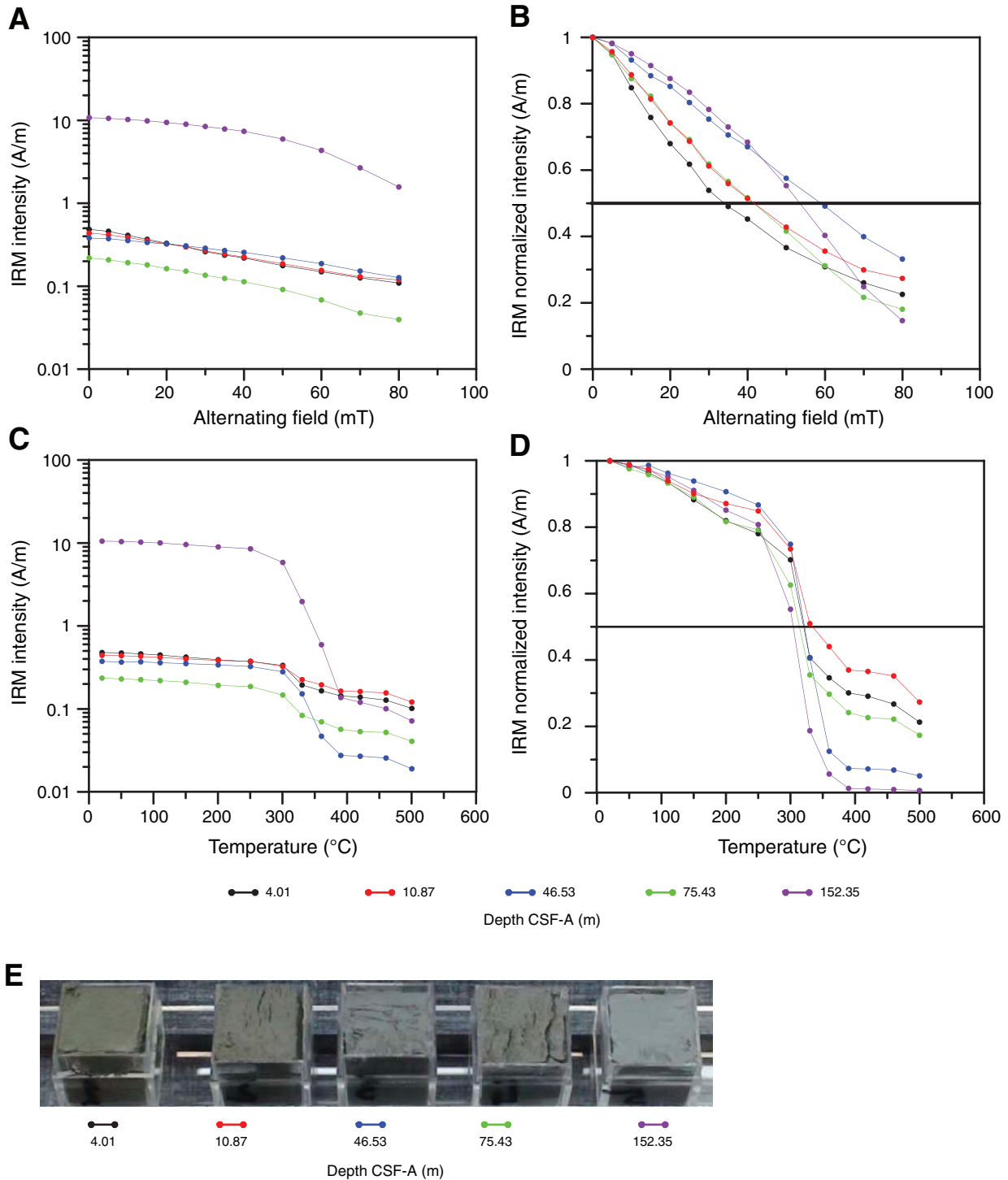


Figure F23. Raw and Gaussian low-pass filtered data for magnetic susceptibility (loop and point sensors), natural gamma radiation (NGR), gamma ray attenuation (GRA) bulk density, and color reflectance parameter b^* , Hole U1353B. Extreme high and low values, interpreted as noise, are not shown.

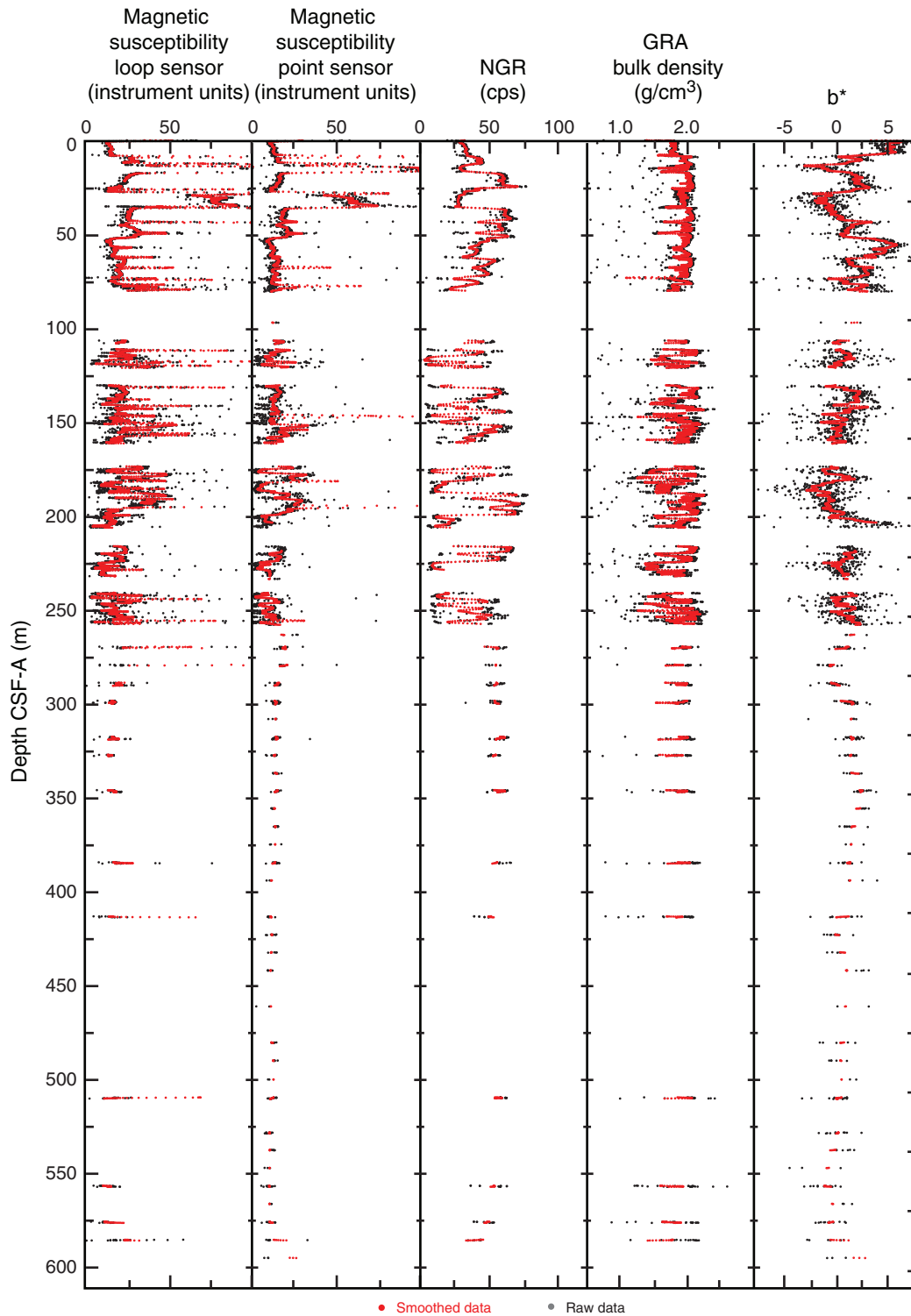


Figure F24. A. Gamma ray attenuation (GRA) bulk density from the overlapping portions of Holes U1353A and U1353B compared to moisture and density (MAD) bulk density estimates. B. GRA bulk density and MAD bulk density, Hole U1353B.

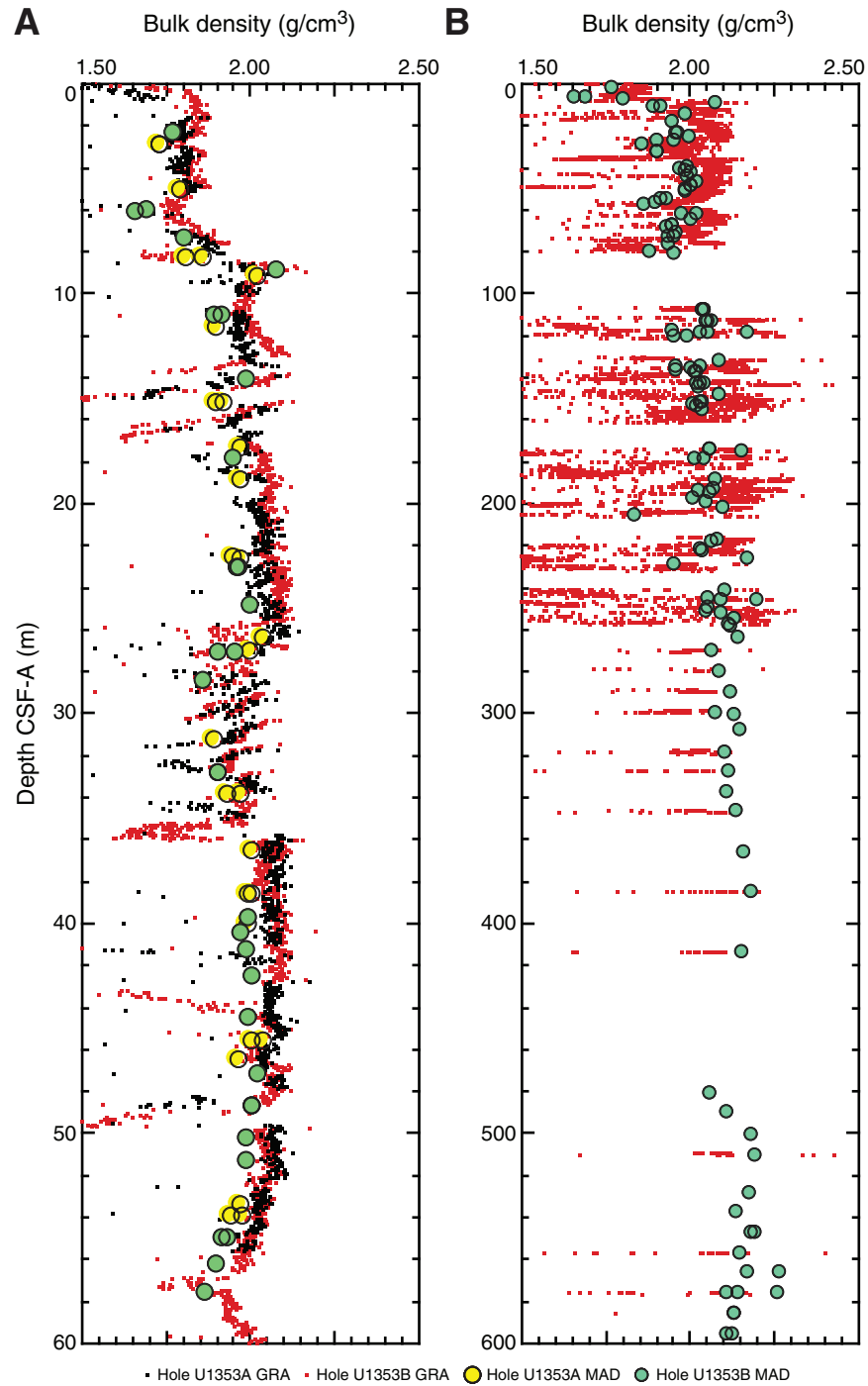


Figure F25. (A) Magnetic susceptibility (loop sensor) and (B) natural gamma radiation (NGR) in the uppermost 80 m of Holes U1353A and U1353B.

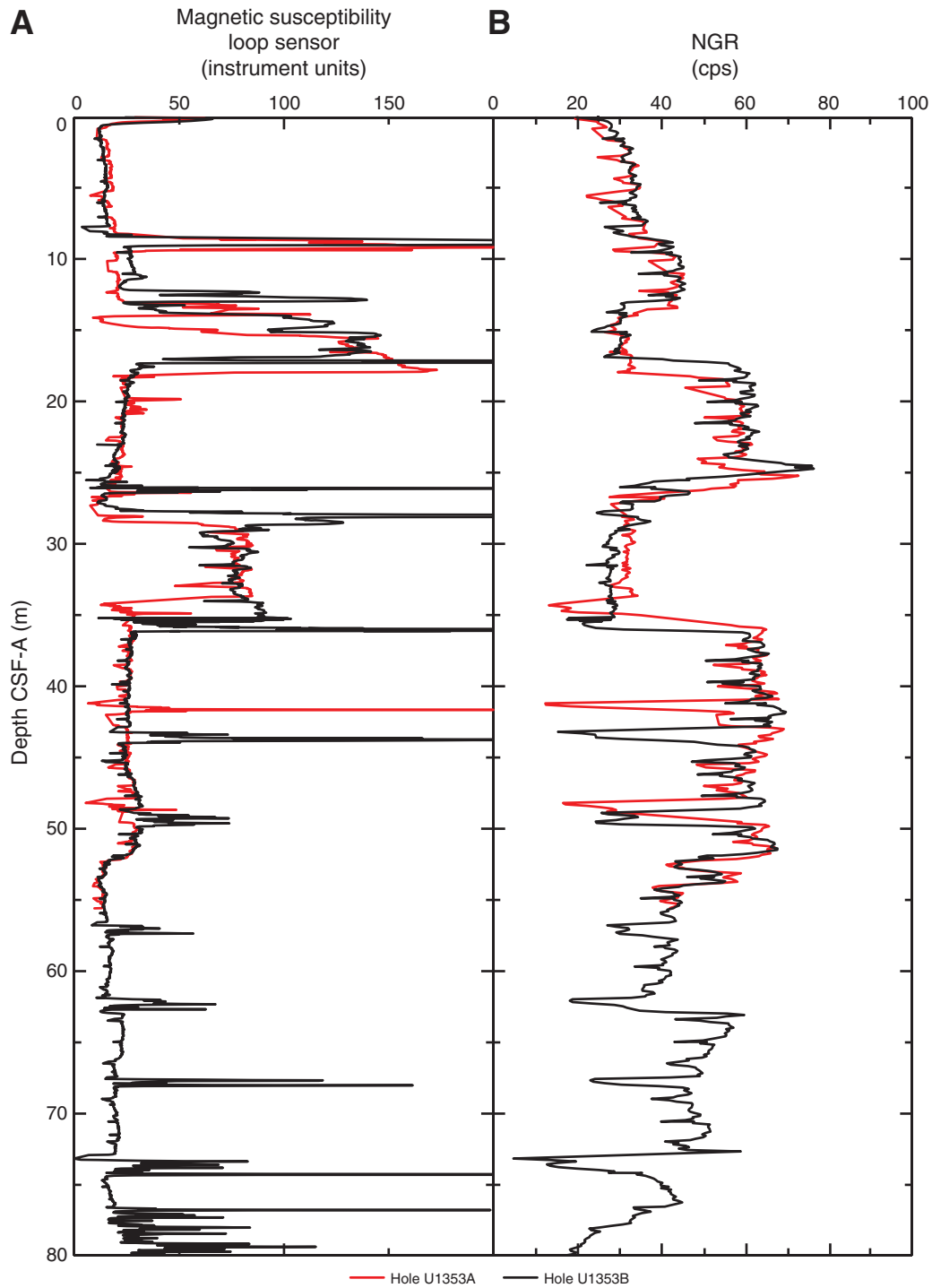


Figure F26. A. Whole-round *P*-wave velocity, Holes U1353A and U1353B. B. Section-half *P*-wave velocities (*x*-, *y*-, and *z*-axes), Hole U1353B. PWL = *P*-wave logger, PWC = *P*-wave caliper, PWB = *P*-wave bayonets.

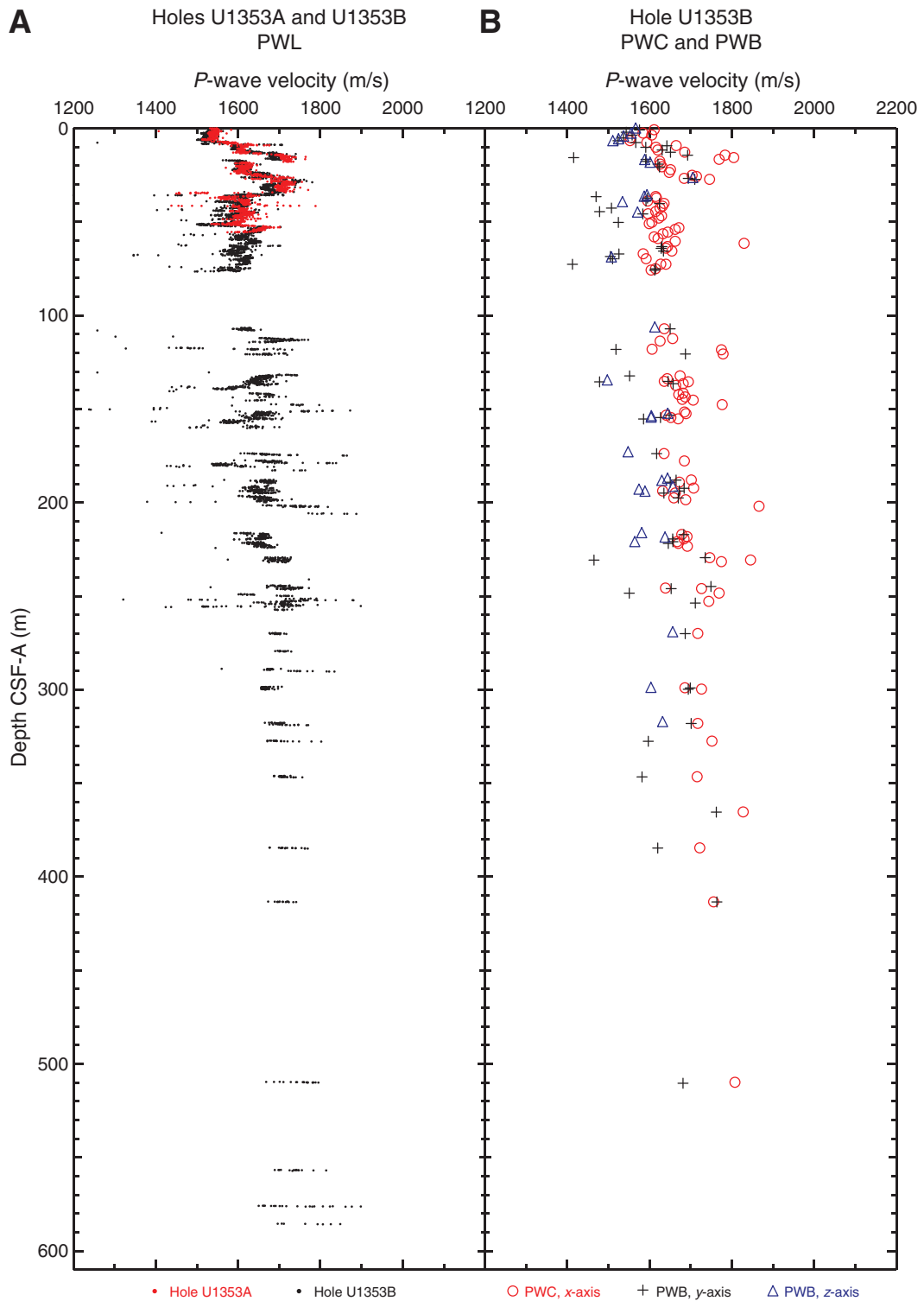


Figure F27. L*a*b* color parameters, Hole U1353B. Smoothed data for all plotted parameters were generated by applying a 30-pass Gaussian filter to the raw data.

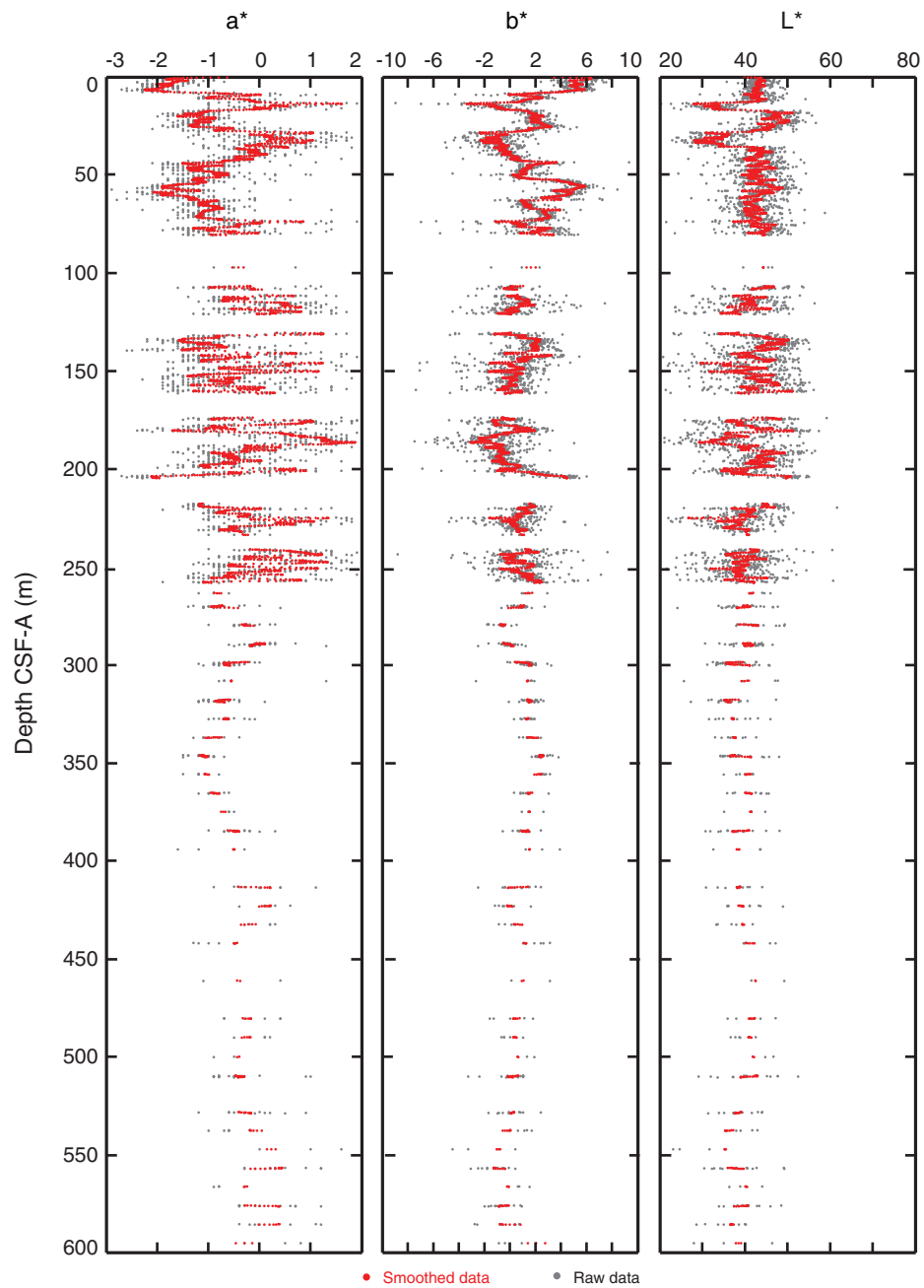


Figure F28. $L^*a^*b^*$ color parameters for the uppermost 250 m of Hole U1353B, plotted alongside magnetic susceptibility (loop and point sensors) and natural gamma radiation (NGR). Blue shaded bars indicate intervals where L^* and b^* values decrease pronouncedly and a^* values increase. The two intervals where this occurs between 13 and 36 m are associated with low NGR and high magnetic susceptibility and are sandy, whereas the interval between 183 and 189 m is associated with both low NGR and low magnetic susceptibility and is coincident with a gravel unit (see text for discussion).

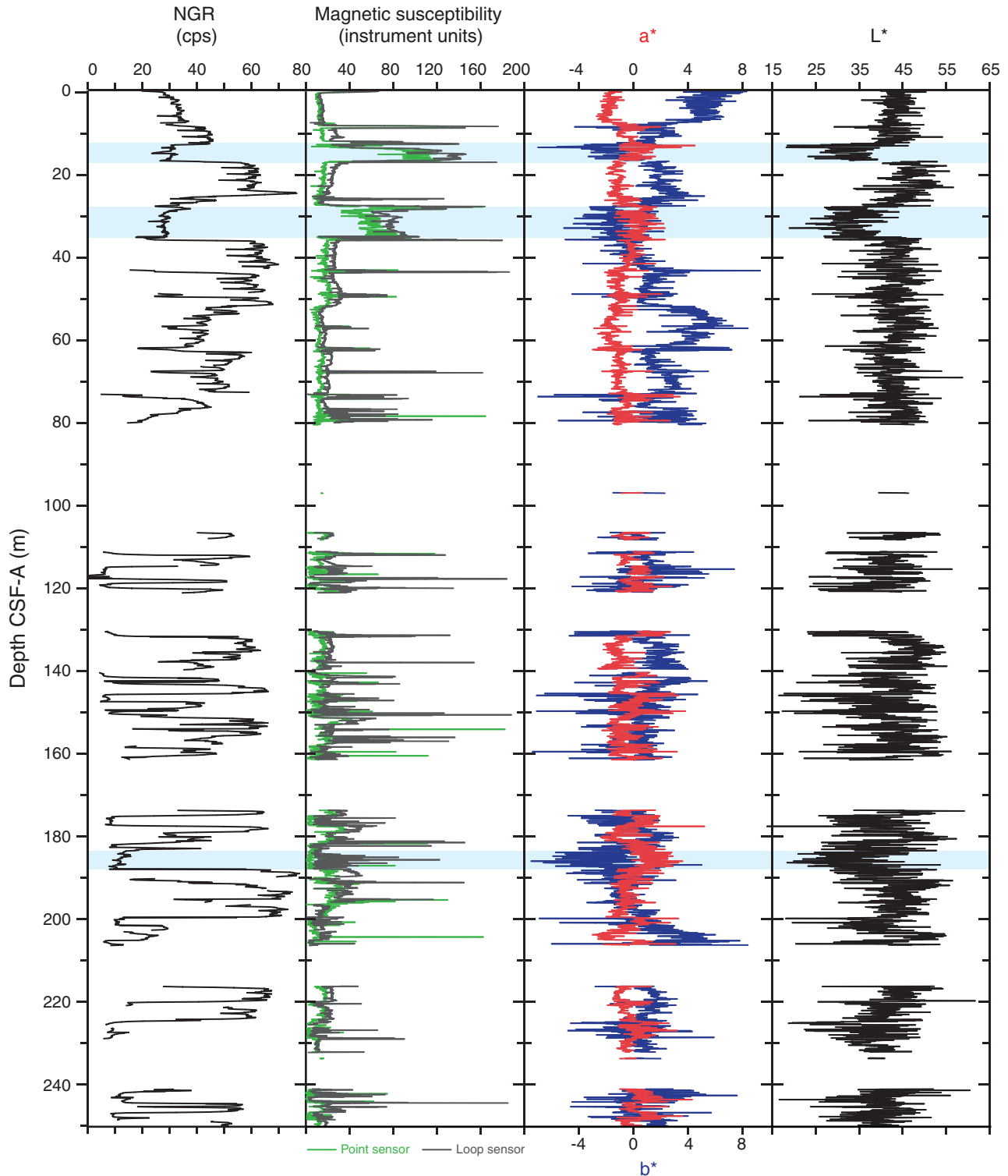


Figure F29. Comparison of porosity from MAD catwalk samples and adjacent samples taken at the sample table in the normal manner. **A.** Cross-plot of results from the two sampling methods. Samples below the line had more water on the sample table, whereas those above the line had more water when collected immediately on the catwalk. **B.** Results from the two sampling methods plotted as a function of depth. Blue = catwalk samples, red = sample table samples. Note the scale break between 200 and 540 m.

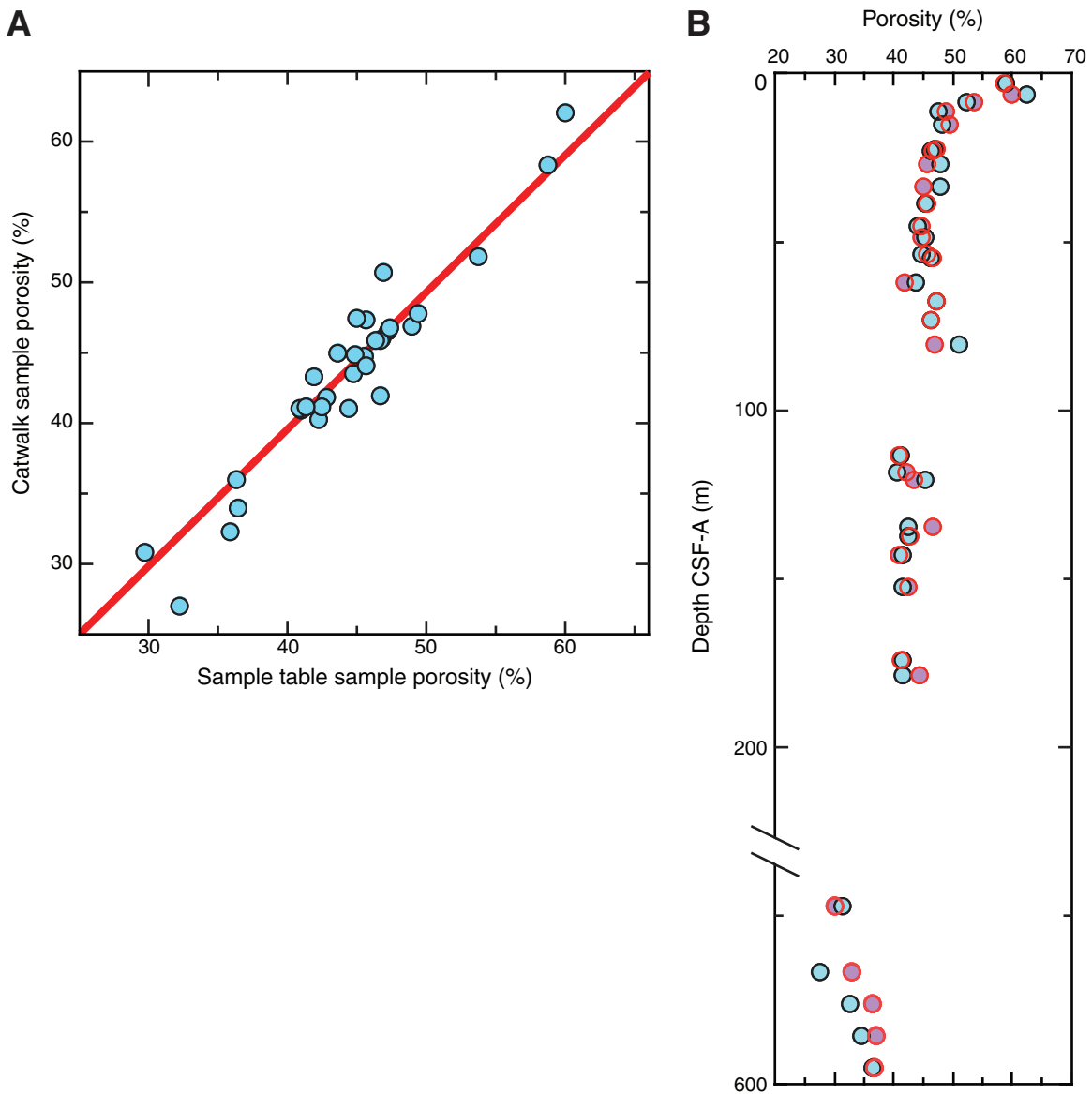


Figure F30. Bulk density, grain density, porosity, and void ratio, Holes U1353A (red-rimmed circles) and U1353B (black-rimmed circles), plotted together as a function of depth (blue line). Black dashed line = lithologic Unit I/II boundary, gray dashed lines = unconformities identified by biostratigraphy.

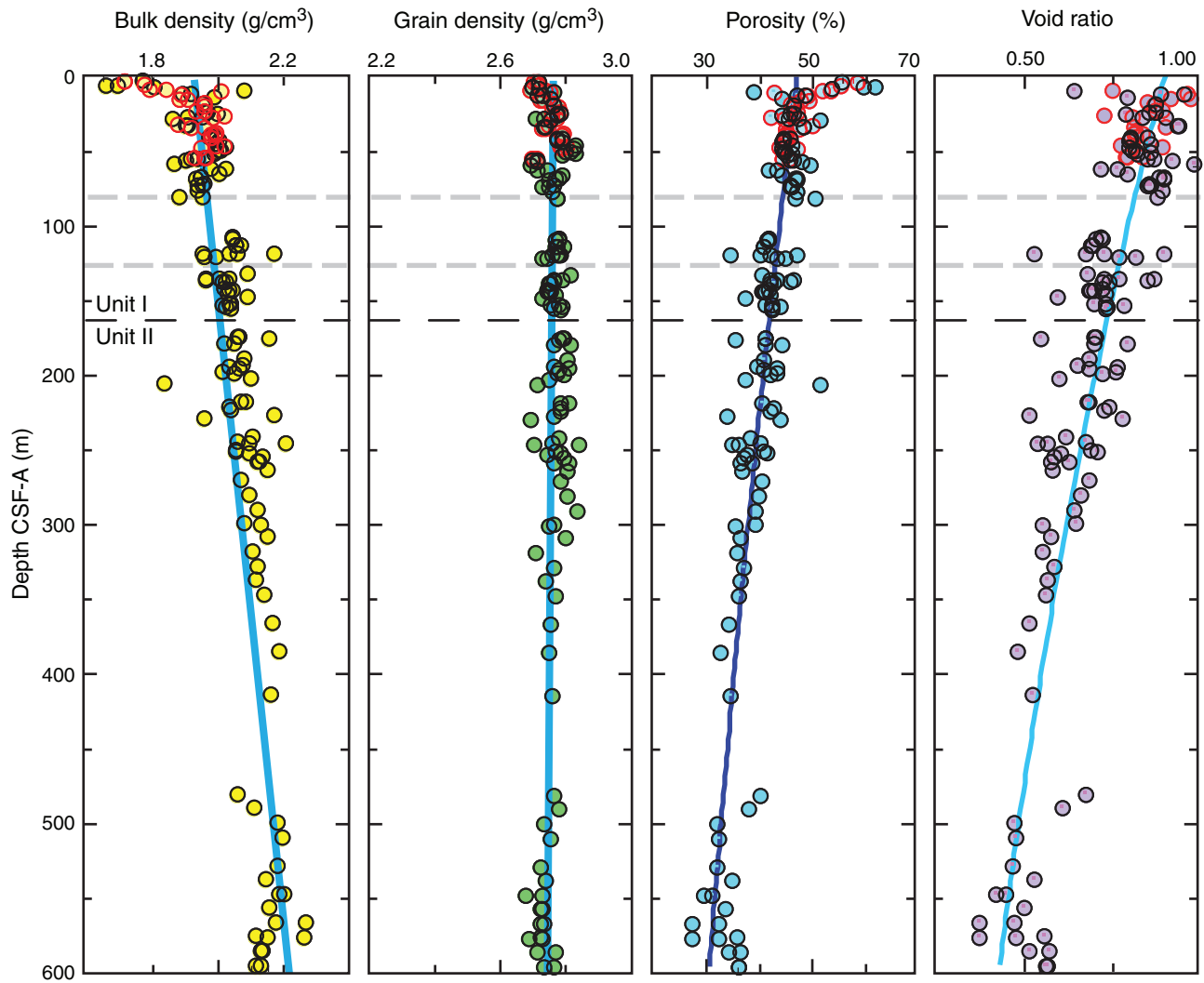


Figure F31. (A) Automated vane shear (AVS) and (B) fall cone penetrometer (FCP) shear strength with (C) cross-plot of AVS and FCP data, Hole U1353B. AVS test results are given as a function of pressure in pascals (kPa = kN/m²), whereas FCP test results are given in terms of newtons of kN/m².

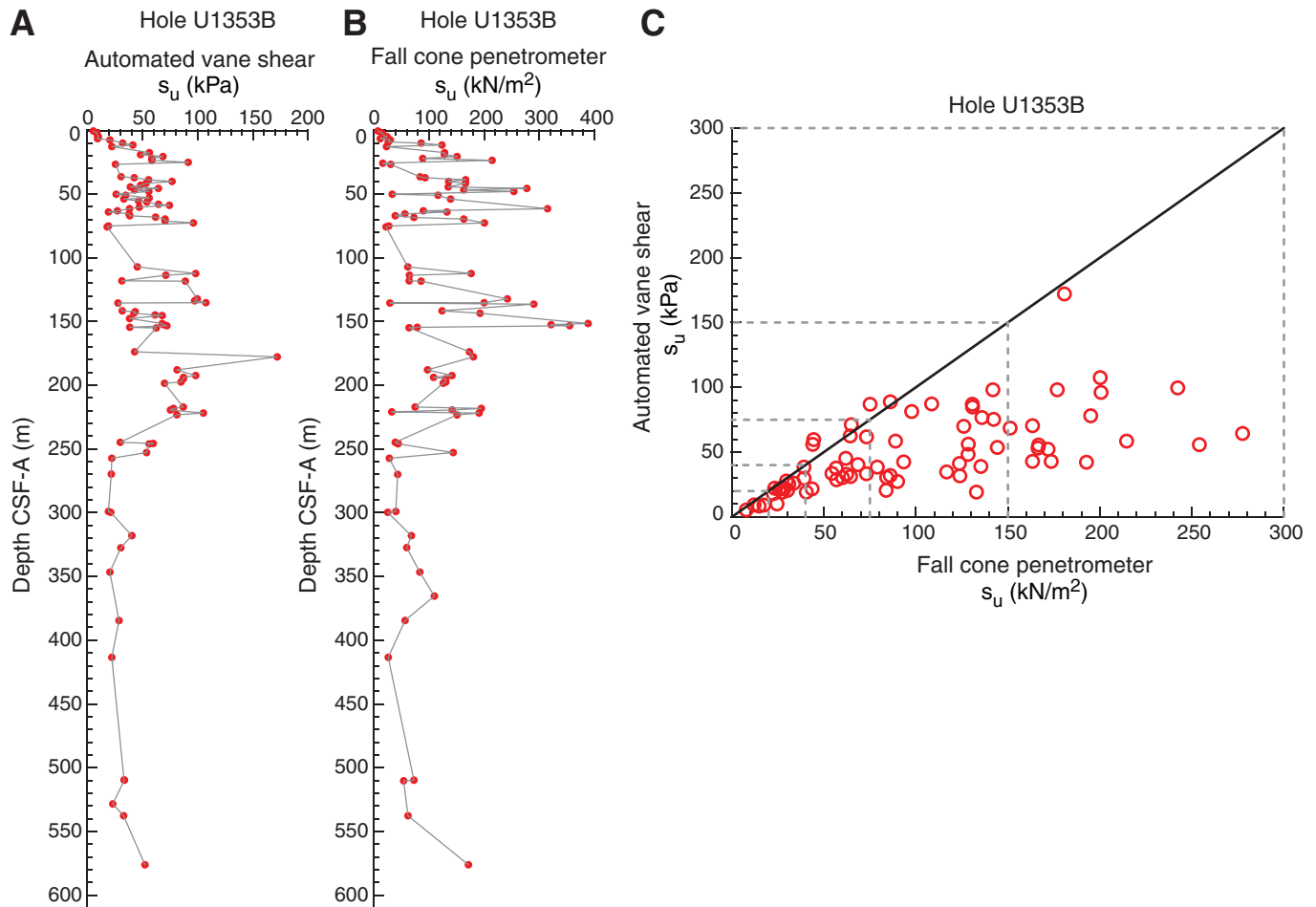


Figure F32. Plots of methane (C_1) concentrations (parts per million by volume [ppmv]) in headspace (HS) gas vs. depth, Holes U1353A (red) and U1353B (black).

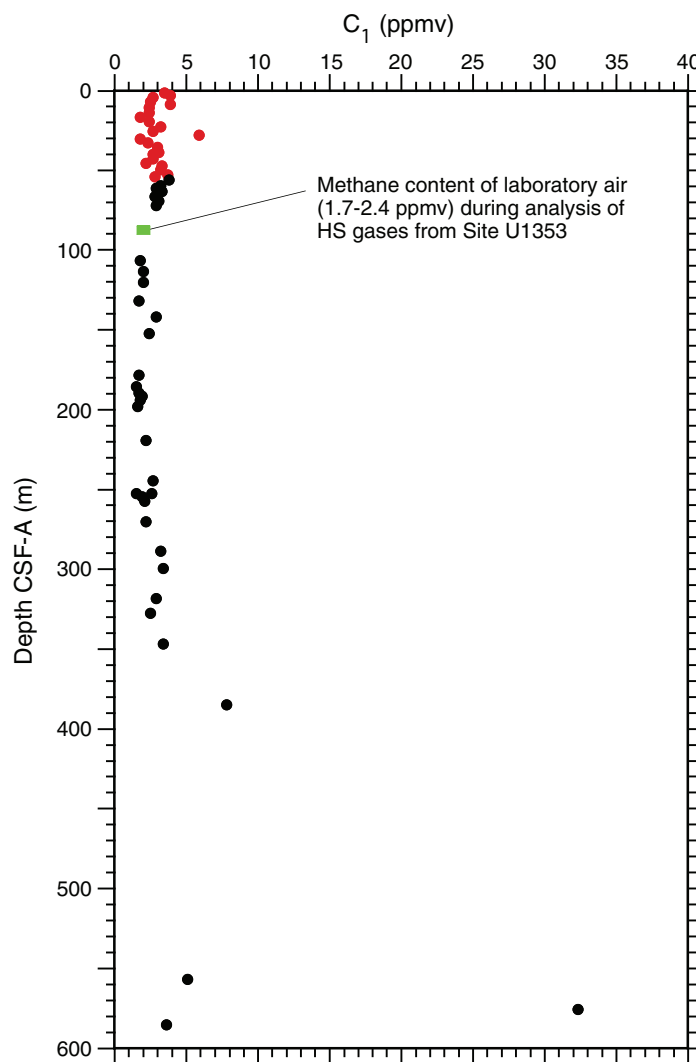


Figure F33. Plots of sediment elemental concentrations vs. depth, Hole U1353B. **A.** Carbonate carbon (as CaCO_3). **B.** Total carbon. **C.** Total nitrogen. **D.** Total organic carbon by difference (TOC_{DIFF}). **E.** Total organic carbon from the source rock analyzer (TOC_{SRA}). **F.** Ratio of TOC_{DIFF} to total nitrogen.

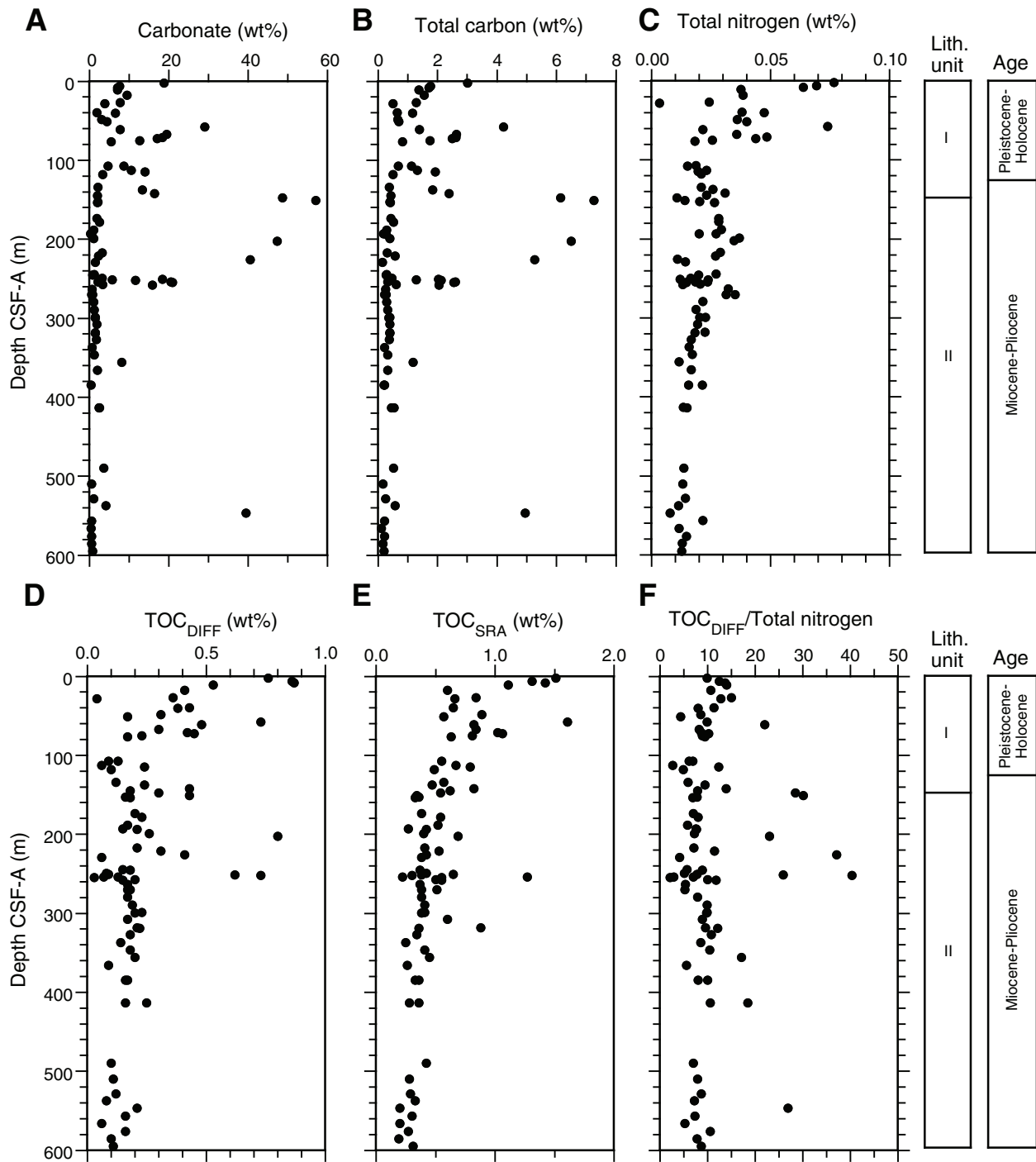


Figure F34. Cross-plot of total carbon measured using two approaches: (1) direct measurement with the CHNS elemental analyzer and (2) the sum of inorganic carbon measured by the coulometer (IC_{COUL}) and total organic carbon measured by the source rock analyzer (TOC_{SRA}). Black line = 1:1 line, dashed red line = correlation line for all data.

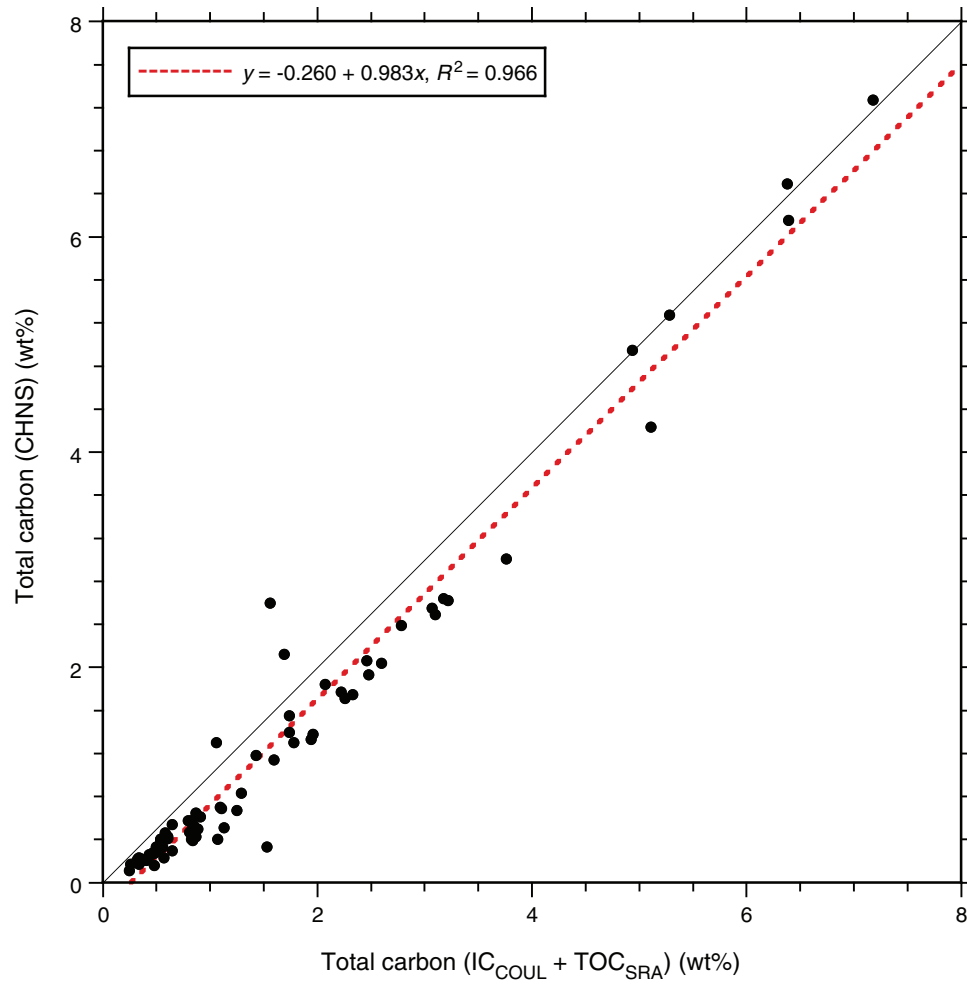


Figure F35. Plots of source rock analyzer data vs. depth, Hole U1353B. **A.** Volatile hydrocarbons (S_1). **B.** Pyrolyzable kerogen (S_2). **C.** Oxidized kerogen (S_3) at $<390^\circ\text{C}$. **D.** Pyrolysis carbon (PC).

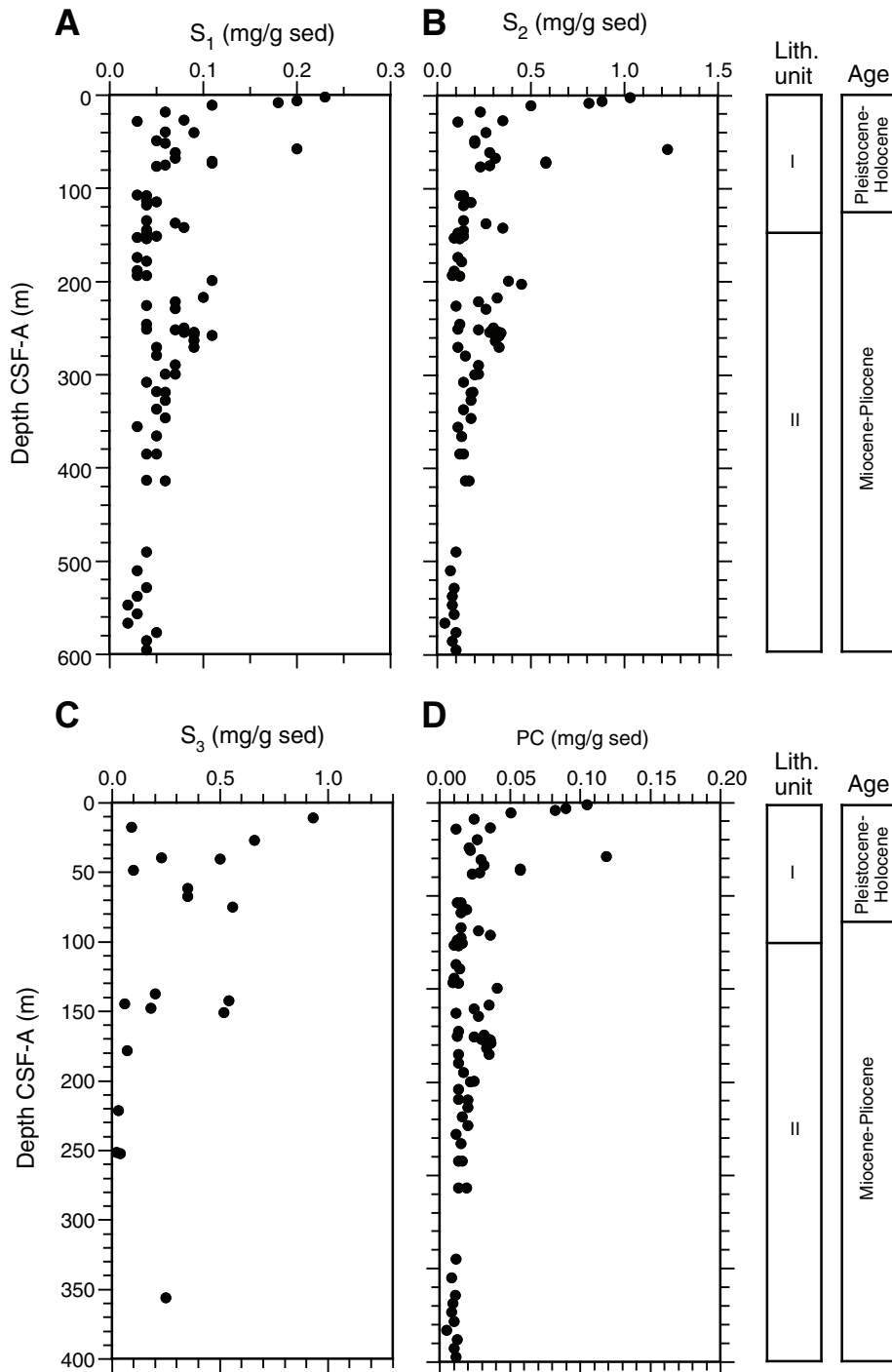


Figure F36. Plots of source rock analyzer parameters vs. depth, Hole U1353B. **A.** Hydrogen index. **B.** Oxygen index. **C.** T_{max} . **D.** Production index. HC = hydrocarbons, TOC = total organic carbon from SRA.

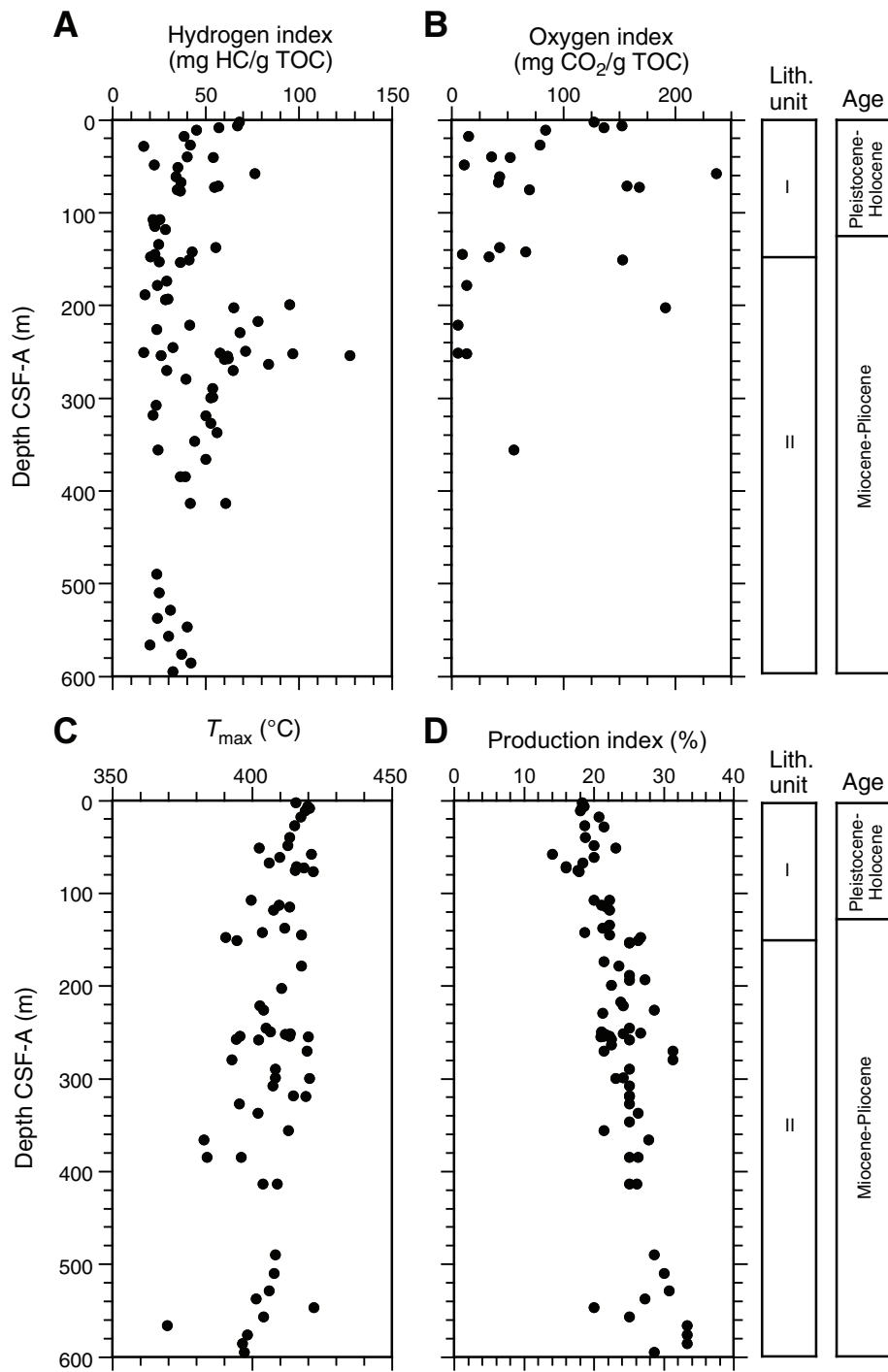


Figure F37. Modified and enlarged van Krevelen diagram based on a cross-plot of hydrogen index vs. oxygen index, showing trend lines for kerogen Types III and IV, Site U1353. Trend lines for kerogen Types I and II are not shown. Oxygen values for Sections 317-U1353B-9H-1 (57.55 m) and 41H-1 (202.20 m) are >170 and are not shown on this diagram. TOC = total organic carbon from SRA.

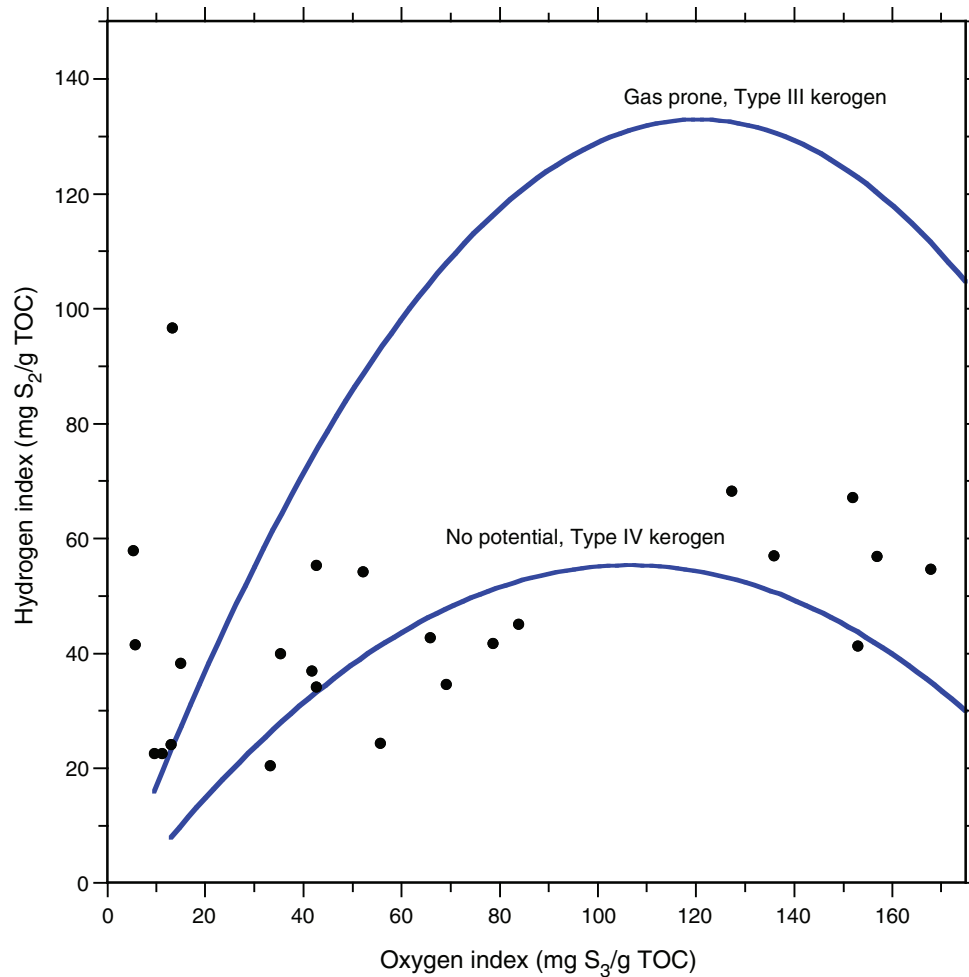


Figure F38. Plots of ionic constituents of interstitial water vs. depth, Holes U1353A (red) and U1353B (black). A. Salinity. B. Chloride. C. Sodium. D. pH. SW = IAPSO seawater values.

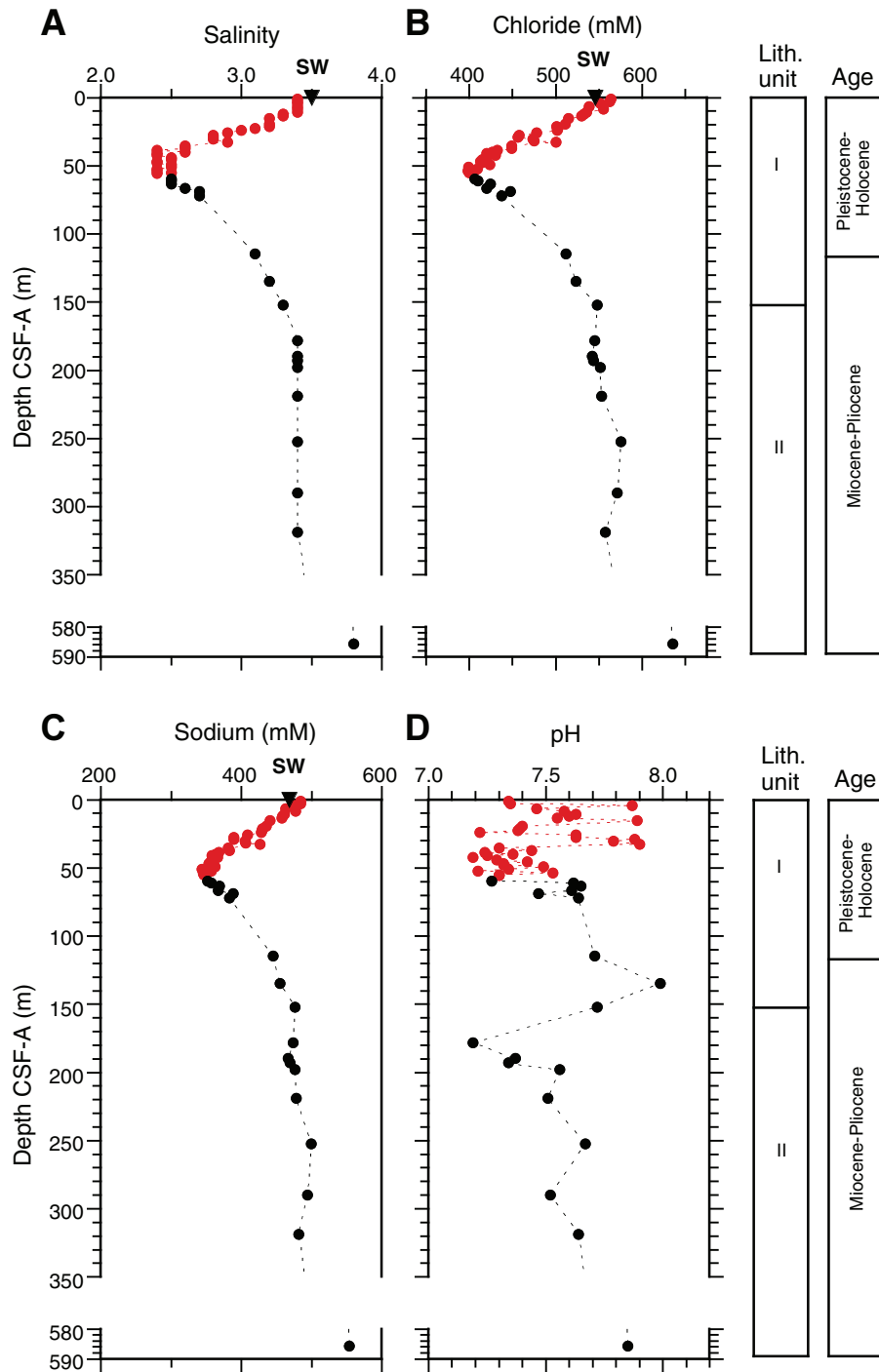


Figure F39. Plots of ionic constituents of interstitial water vs. depth, Holes U1353A (red) and U1353B (black). A. Calcium. B. Magnesium. C. Magnesium/calcium ratio. D. Strontium. E. Strontium/calcium ratio. F. Alkalinity. SW = IAPSO seawater values.

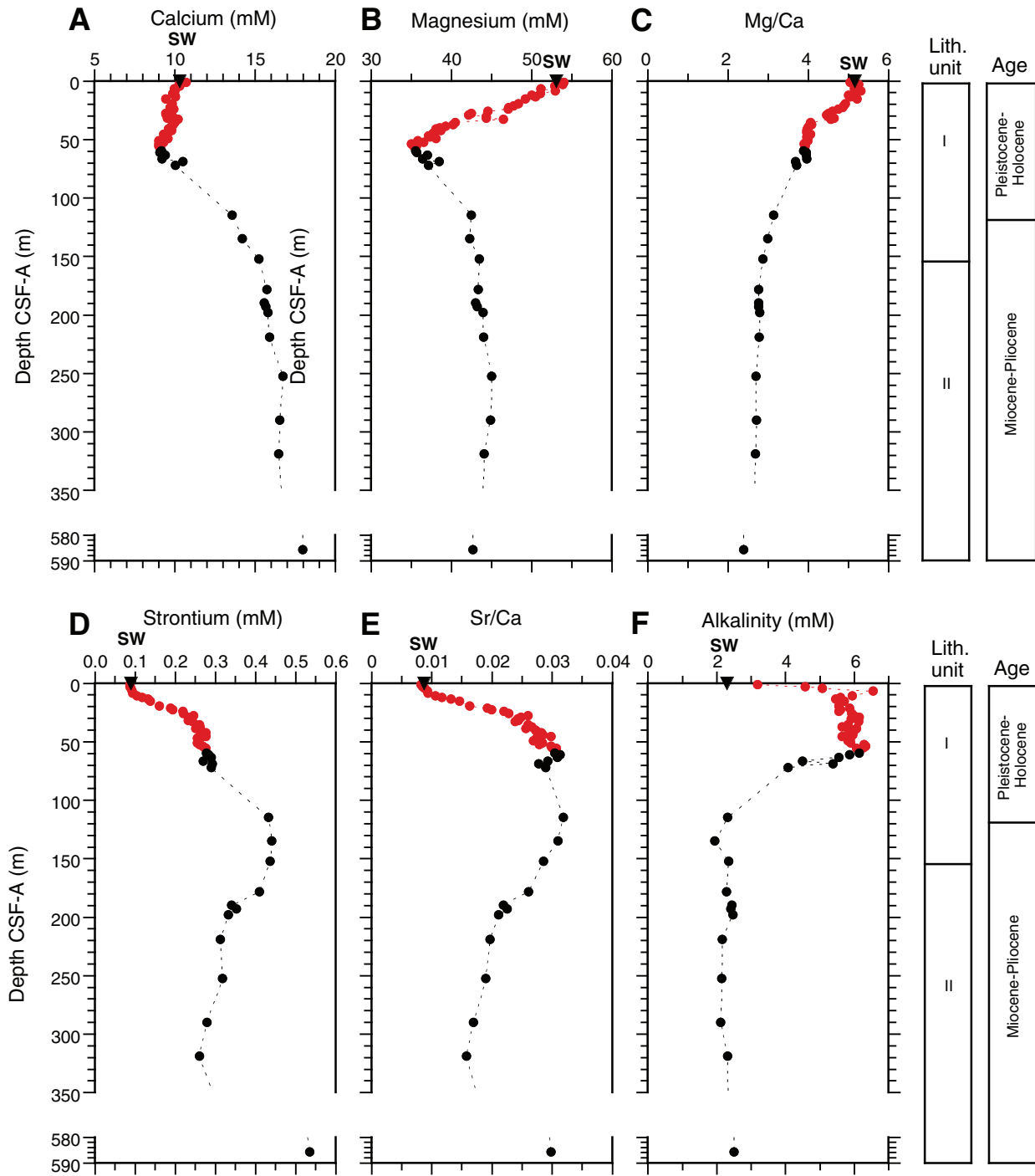


Figure F40. Plots of ionic constituents of interstitial water vs. depth, Holes U1353A (red) and U1353B (black). A. Sulfate. B. Ammonium. C. Phosphate. D. Dissolved silica. SW = IAPSO seawater values.

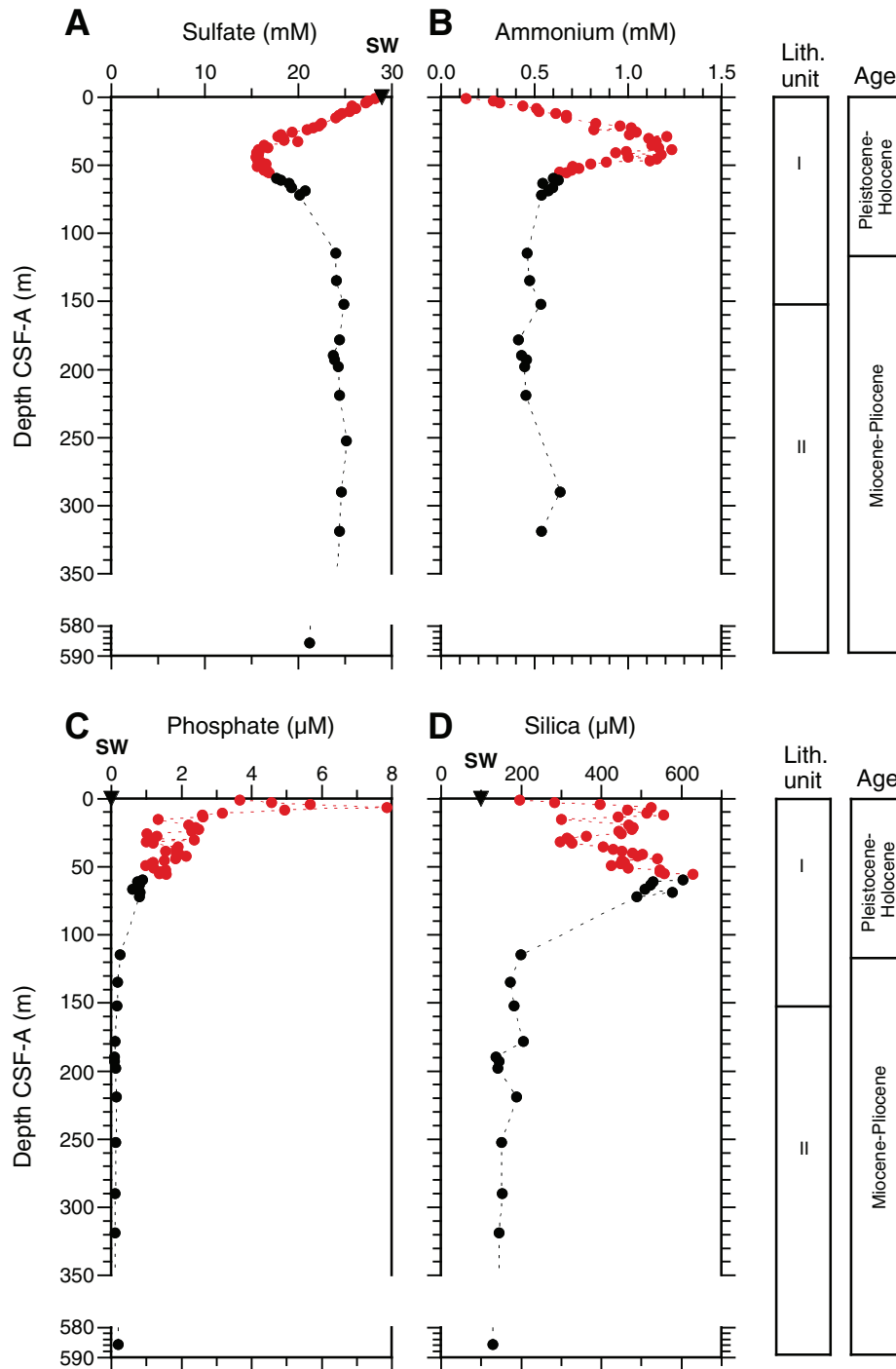


Figure F41. Ionic constituents of interstitial water vs. depth, Holes U1353A (red) and U1353B (black). A. Potassium. B. Barium. C. Lithium. D. Silicon from inductively coupled plasma spectroscopy (ICP). SW = IAPSO seawater values.

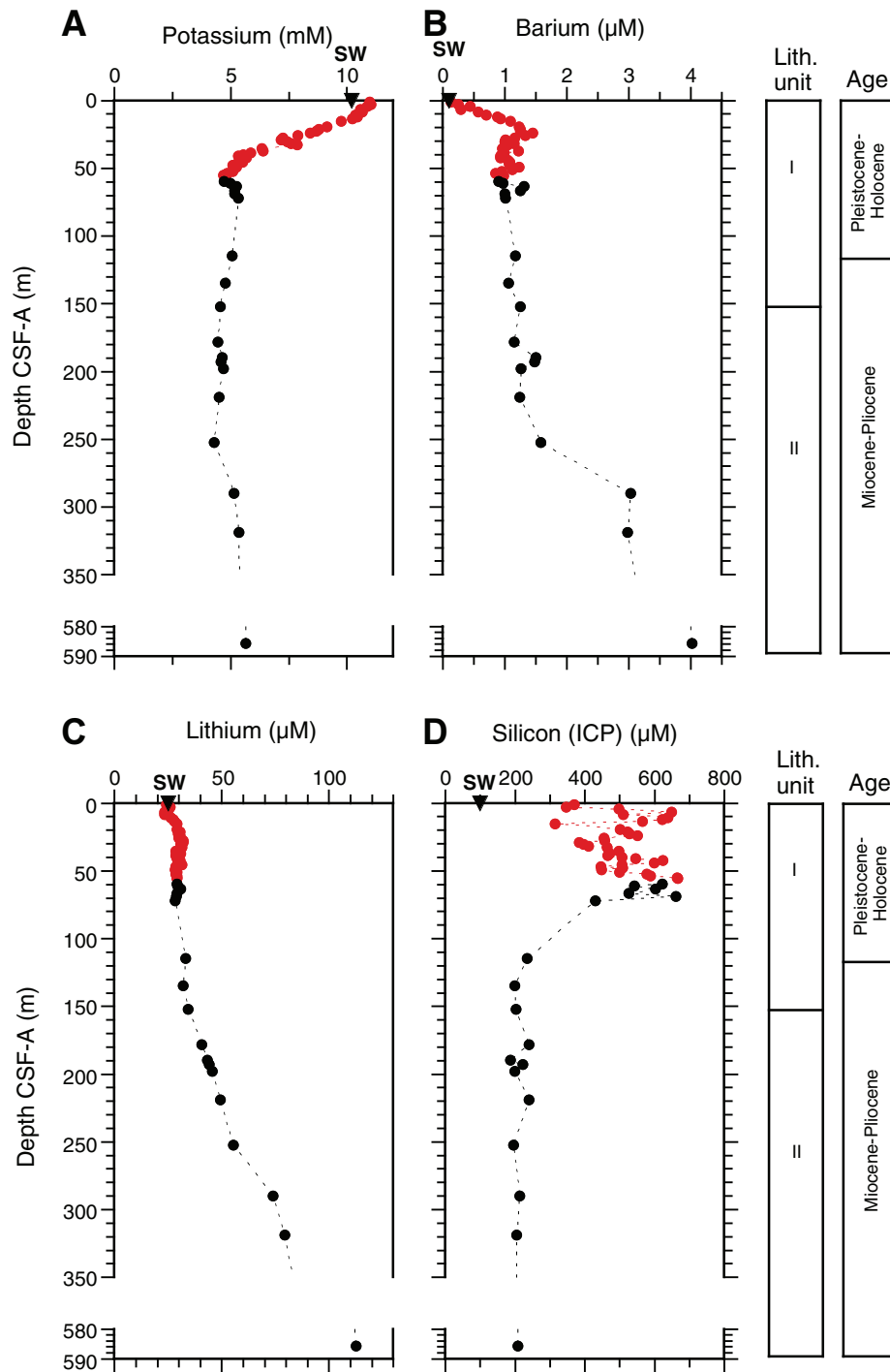


Figure F42. Plots of ionic constituents of interstitial water vs. depth, Holes U1353A (red) and U1353B (black). A. Boron. B. Iron. C. Manganese. SW = IAPSO seawater values.

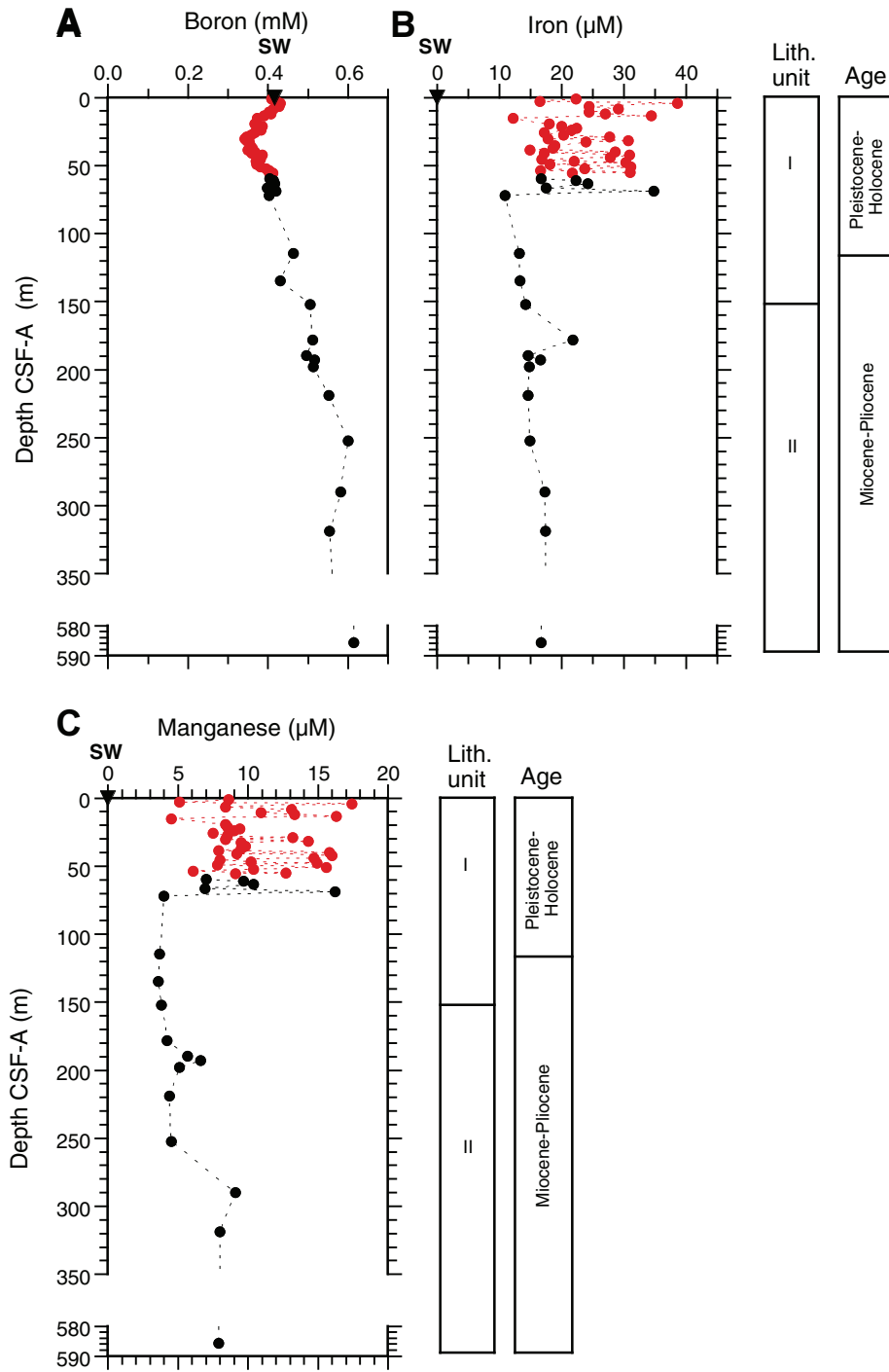


Figure F43. Uppermost 75 m depth profiles for Holes U1353A (open symbols) and U1353B (solid symbols). **A.** Methane, alkalinity, sulfate, calcium, and magnesium. **B.** Phosphate. **C.** Dissolved silica. **D.** Barium.

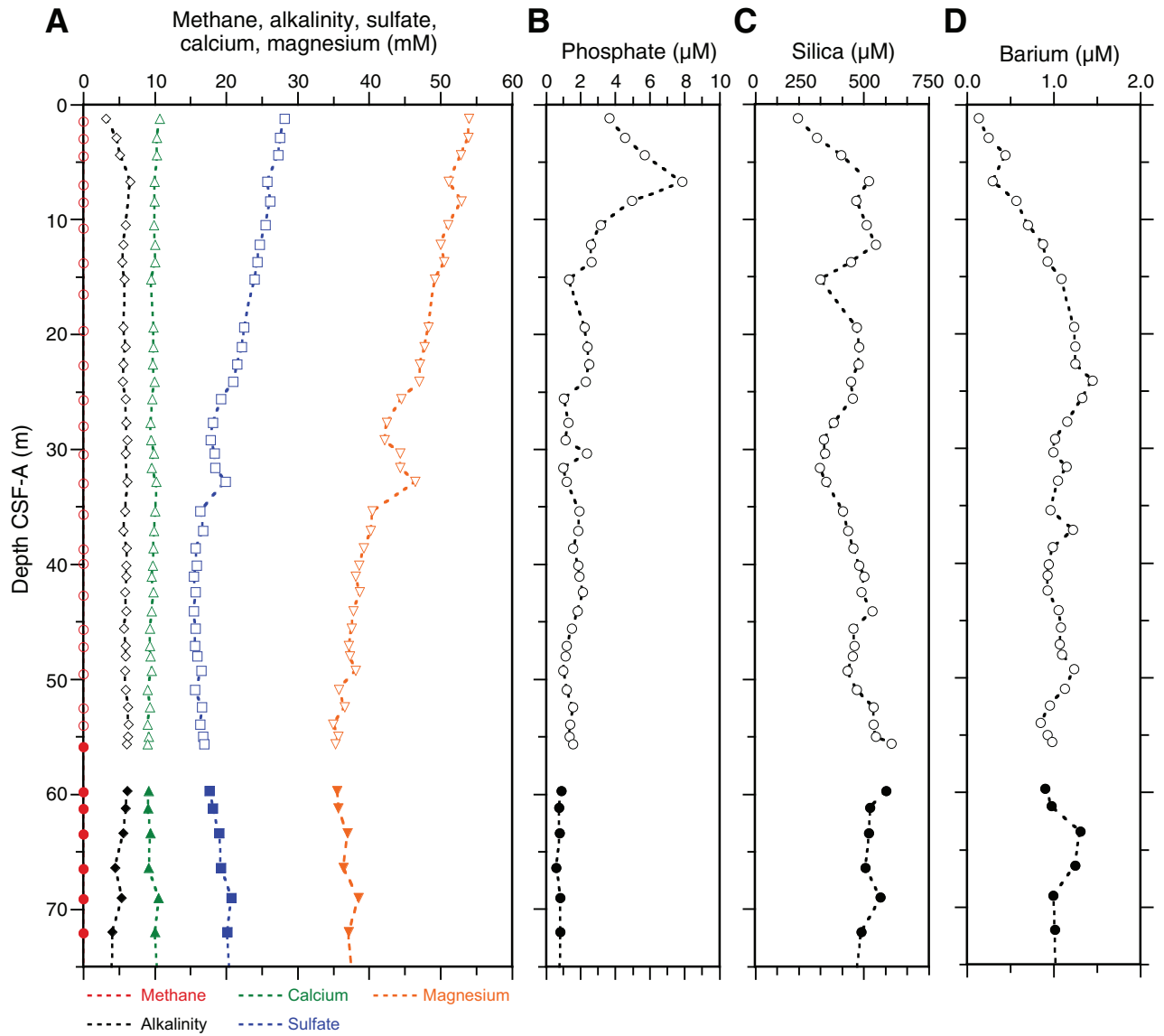


Figure F44. Uppermost 350 m depth profile of chlorinity-normalized (solid symbols) and observed (open symbols) values of alkalinity, calcium, sulfate, and magnesium for Holes U1353A (upward triangles, circles, and squares) and U1353B (downward triangles, diamonds, and squares with diagonal line).

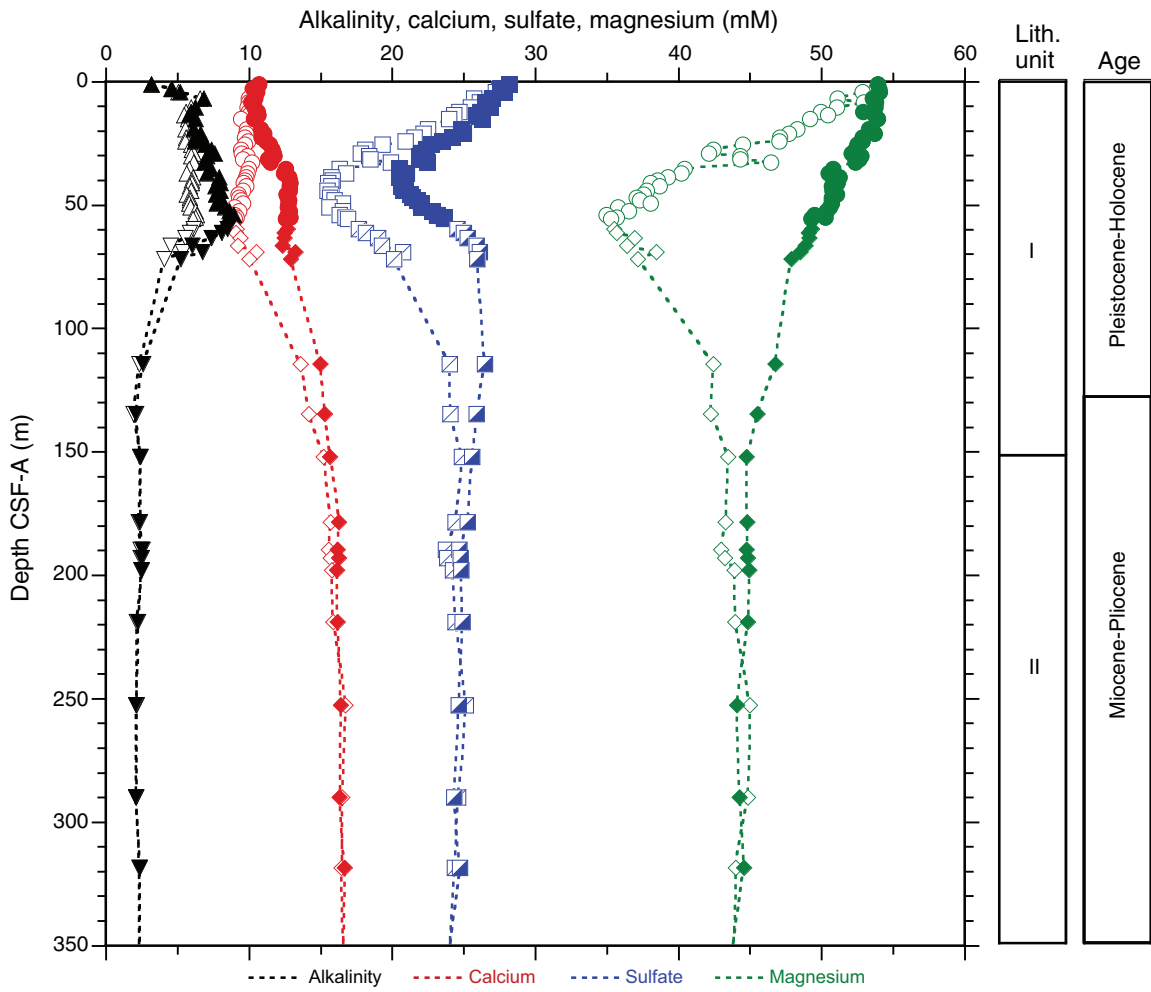


Figure F45. A. Temperature data for Site U1353. During the time interval t_i to t_f (open circles), an exponential decrease in temperature was expected and used to estimate ambient temperature. Unfortunately, only one temperature measurement was made (Core 317-U1353A-5H), and this measurement is unreliable because of the irregular curve. See Table T20 for value. APCT-3 = third-generation advanced piston corer temperature tool.

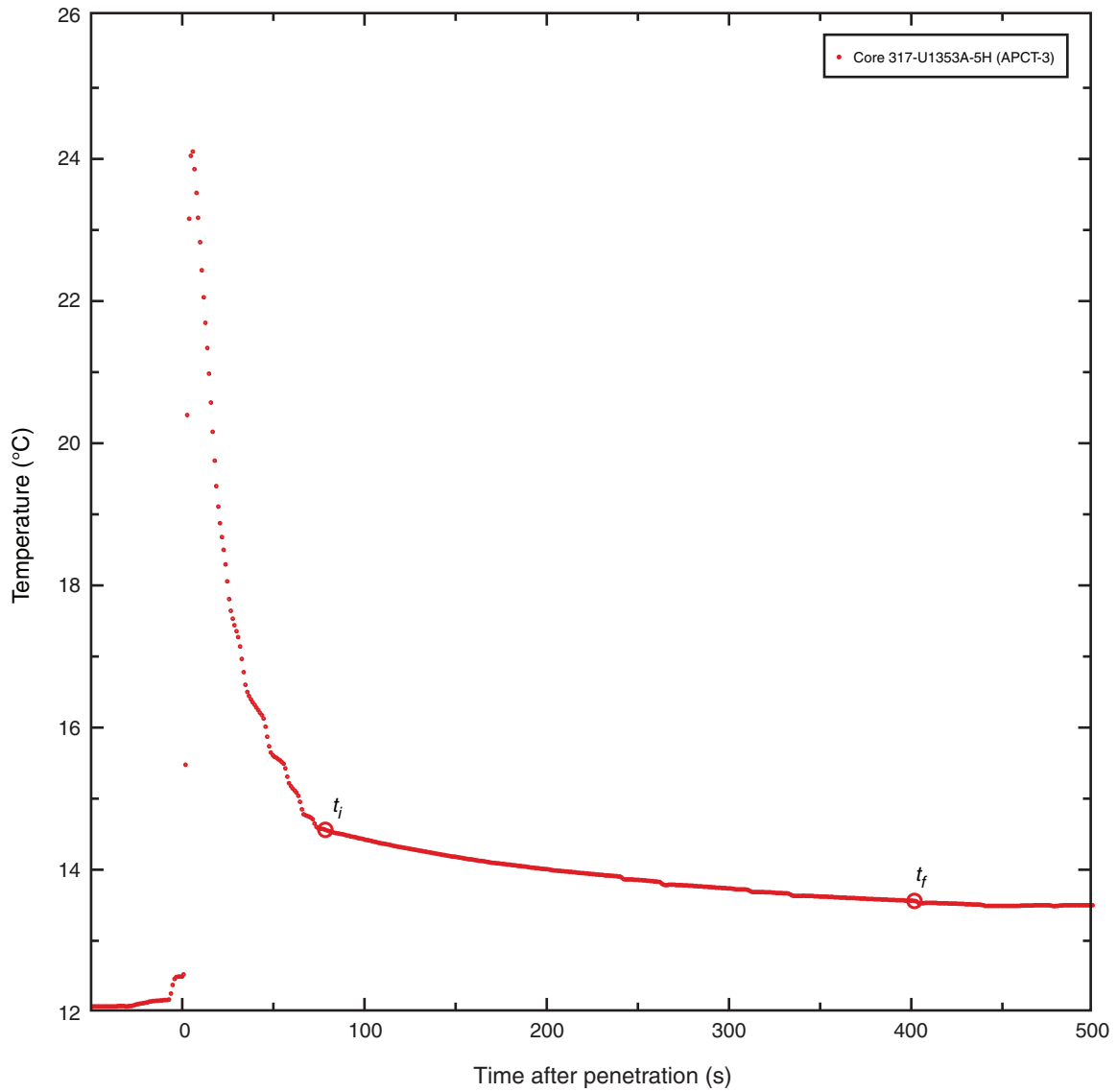


Figure F46. Thermal conductivity for Site U1353 vs. (A) depth, (B) porosity, and (C) bulk density. Thermal conductivity measurements from Holes U1353A and U1353B were used to determine the relationship between thermal conductivity and depth. The two linear fits (black lines) represent downhole increasing trends with a peak at ~30 m CSF-A, which was also observed at shelf Site U1351. Thermal conductivity correlates negatively with porosity and positively with bulk density. Variation with lithology is weak.

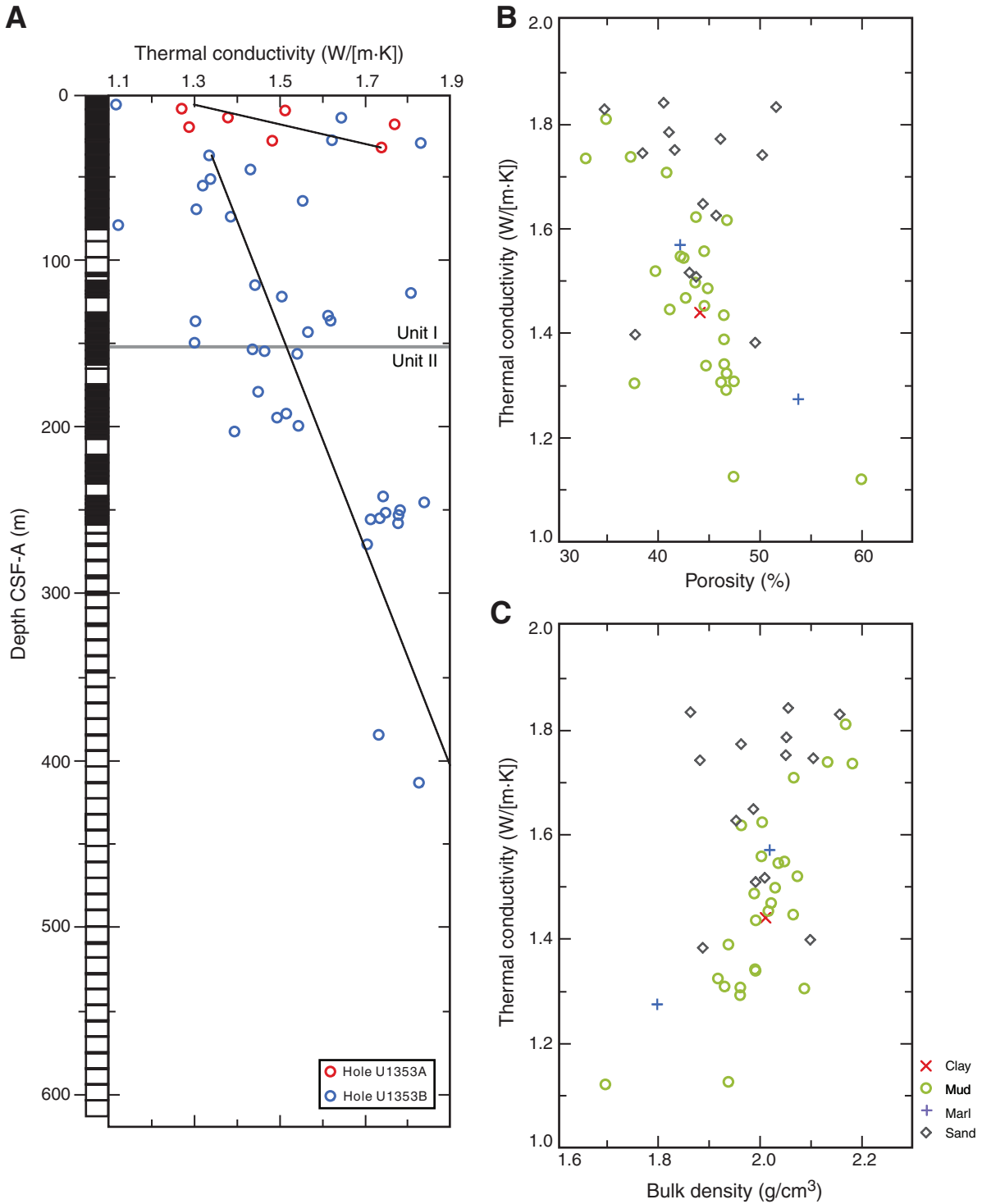


Figure F47. Summary of logs recorded by the triple combination tool string in Hole U1353C and comparison to physical property data measured on cores recovered from Hole U1353B. Resistivity-derived porosity and density were calculated from the phasor deep induction log (IDPH). HLDS = Hostile Environment Litho-Density Sonde, NGR = natural gamma radiation core data, IMPH = phasor medium induction log, MAD = moisture and density core data, GRA = gamma ray attenuation bulk density core measurements.

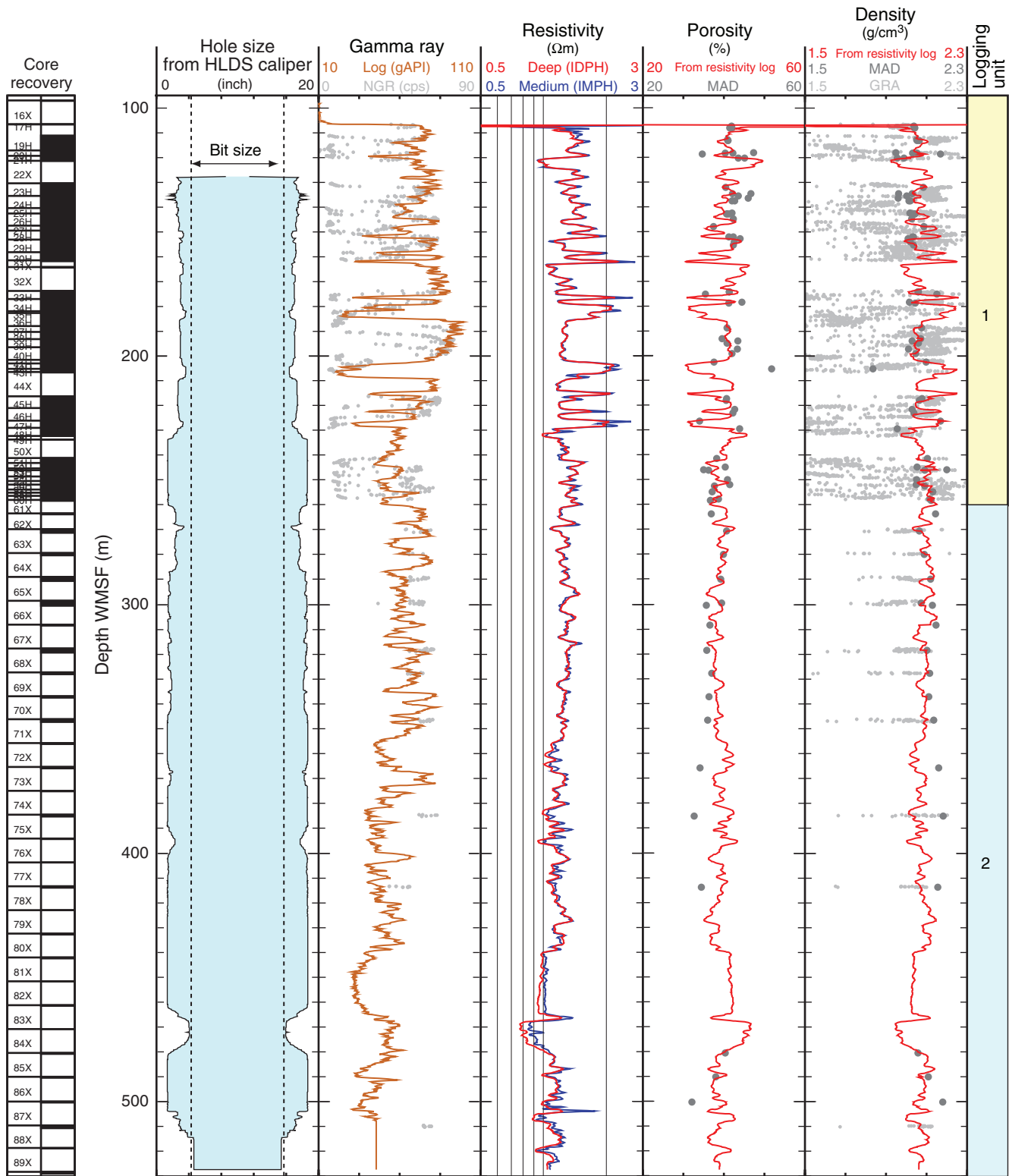


Figure F48. Summary of logs recorded by the Formation MicroScanner (FMS)-sonic tool string in Hole U1353C. Hole size was calculated by the two orthogonal calipers of the FMS (C1 and C2). In the gamma ray track, gamma ray recorded with the FMS-sonic tool string is compared to gamma ray recorded with the triple combination (TC) tool string in the same hole. Sonic waveform (WF) amplitude is shown as an indicator of the quality of the data. High waveform coherence, shown in red in the two velocity tracks, is a measure of the reliability of the slowness/time coherence algorithm used to derive compressional (V_p) and shear (V_s) velocities from the monopole and lower dipole sonic waveforms, respectively. (Figure shown on next page.)



Figure F48 (continued). (Caption shown on previous page.)

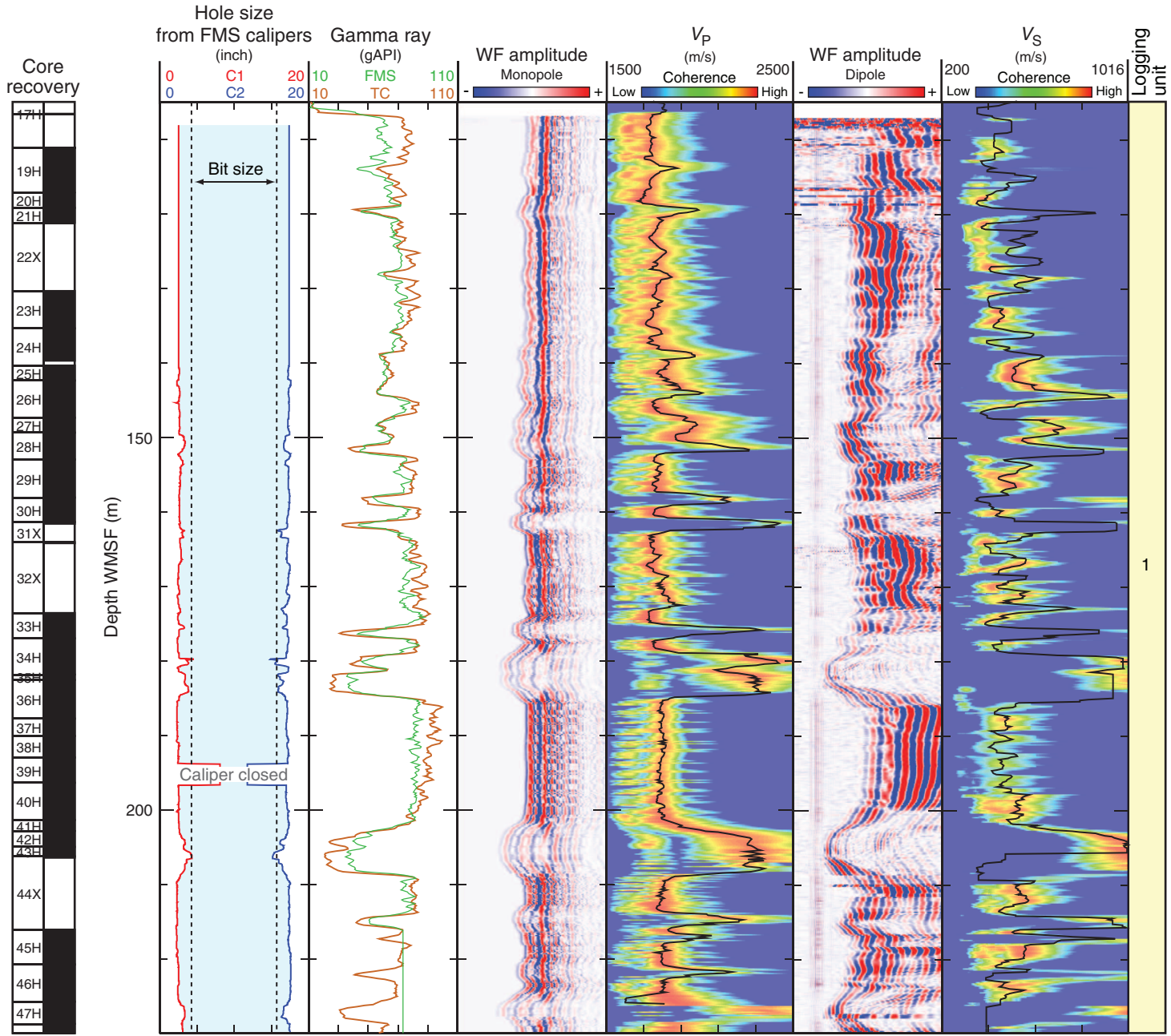


Figure F49. Summary of spectral natural gamma ray measurements in Hole U1353C. SGR = total gamma ray, CGR = computed gamma ray (gamma ray without uranium contribution). The CGR and SGR curves define an envelope (colored green), and the area between the two curves shows the contribution of uranium, a common indicator of organic content. Core recovery is shown for Hole U1353B.

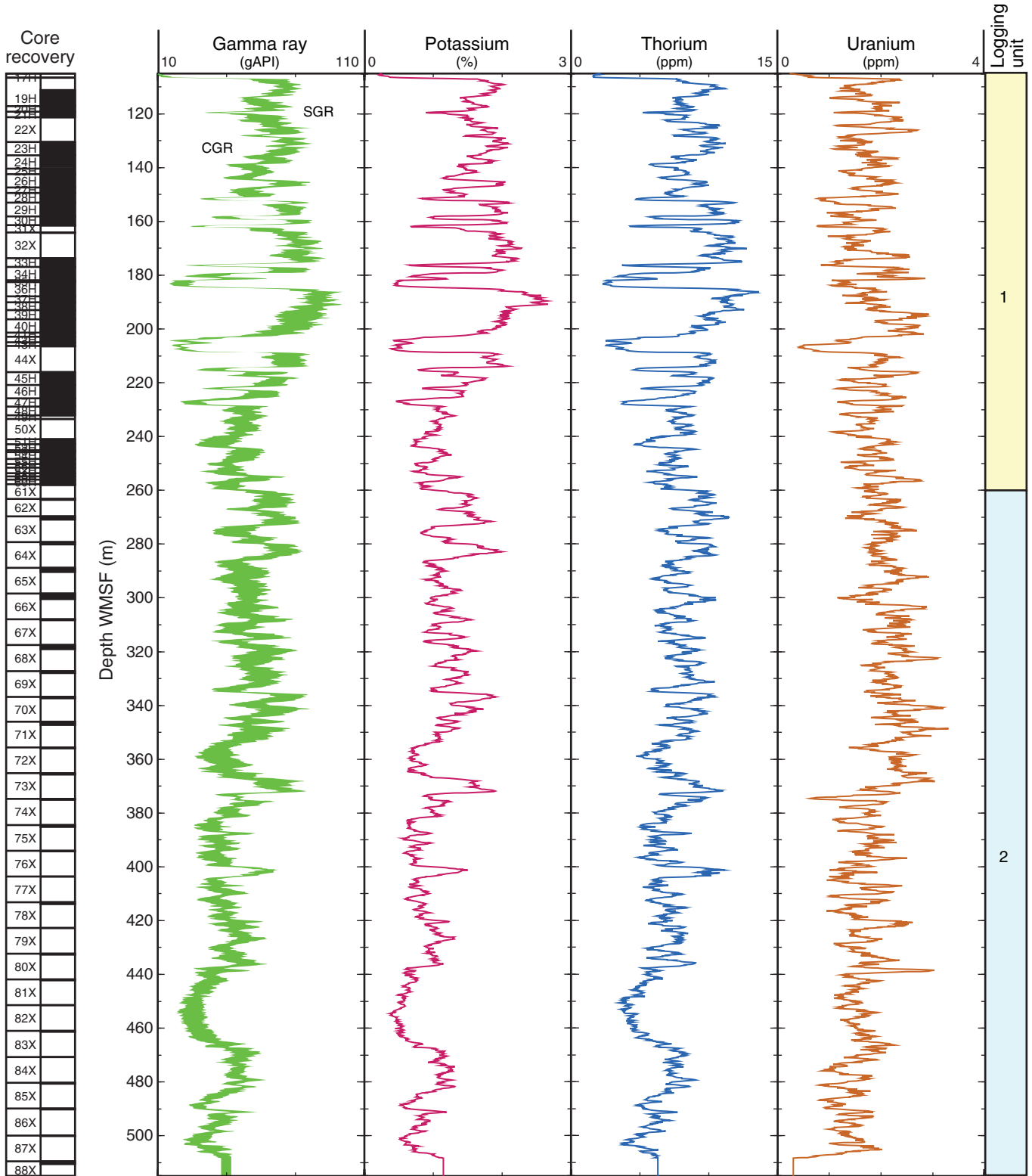


Figure F50. Formation MicroScanner (FMS) images showing the diversity of structures in Hole U1353C. Associated core photographs from Hole U1353B are also shown. **A.** Bottom of lithologic Unit I (Sections 317-U1353B-27H-3, 28H-1, and 28H-2). **B.** Gravels (Sections 317-U1353B-36H-2, 36H-3, and 36H-4). **C.** Fine layering where no core was recovered in Hole U1353B. High resistivity is apparent as brighter colors and high conductivity is apparent as darker colors in the FMS images. FMS images in A and B are dynamically normalized to enhance small-scale contrasts, and the colors are not representative of absolute formation resistivity. (Figure shown on next page.)

Figure F50 (continued). (Caption shown on previous page.)

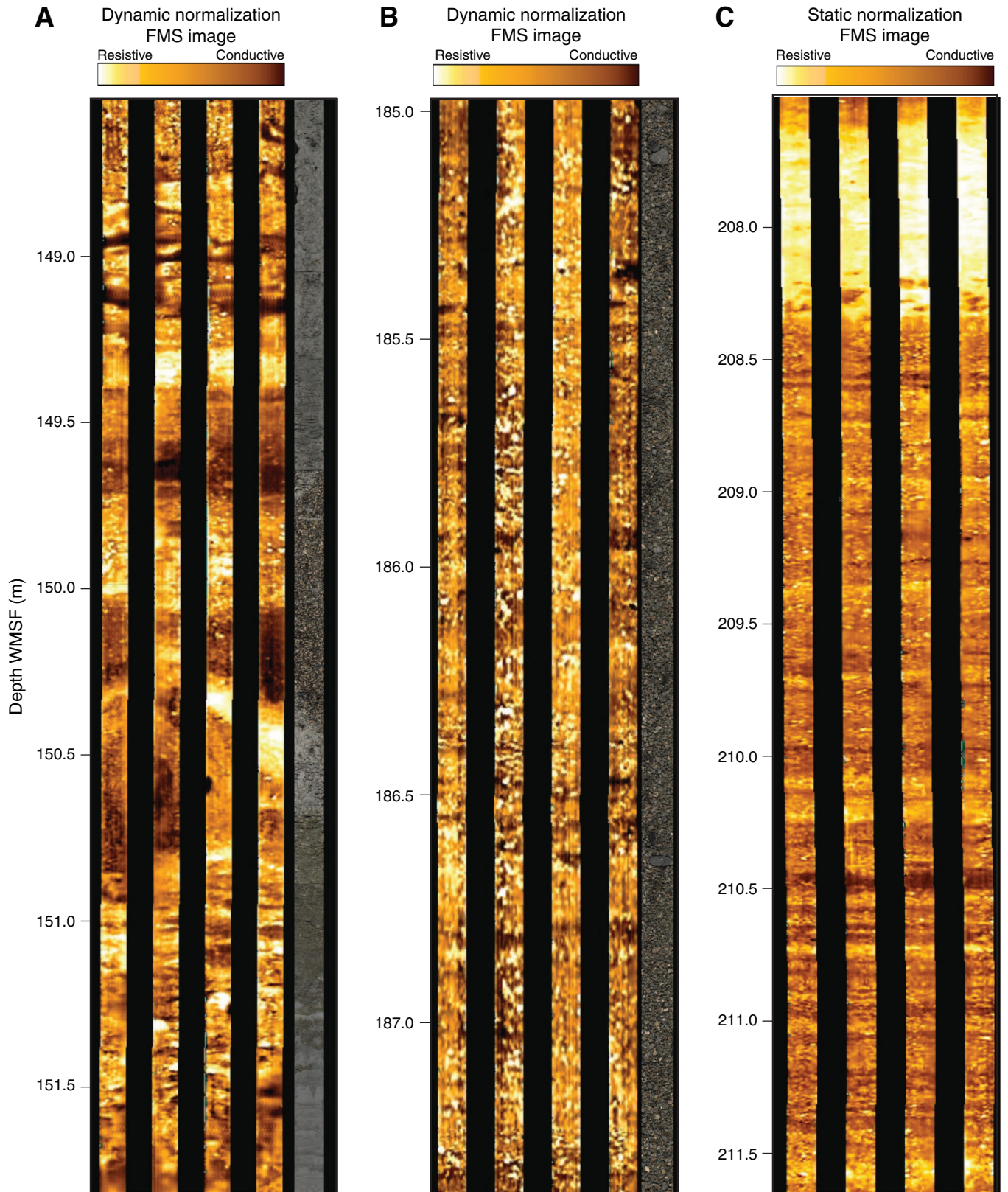


Figure F51. Comparison of synthetic seismogram calculated from density and V_p logs in Hole U1353C with EW00-01 Line 66 across Site U1353. The gamma ray log is shown as a reference to the other logs and the logging units at this site. Density was computed from the resistivity log using Archie's equation and MAD grain density. The V_p log used in this calculation was recorded during the downlog. Dashed lines in seismic panel indicate seismic sequence boundaries U10–U13. Core recovery is shown for Hole U1353B. See “[Downhole logging](#)” for details. TC = triple combination tool string, FMS = Formation MicroScanner-sonic tool string, IDPH = phasor deep induction log, CDP = common depth point. ([Figure shown on next page.](#))



Figure F51 (continued). (Caption shown on previous page.)

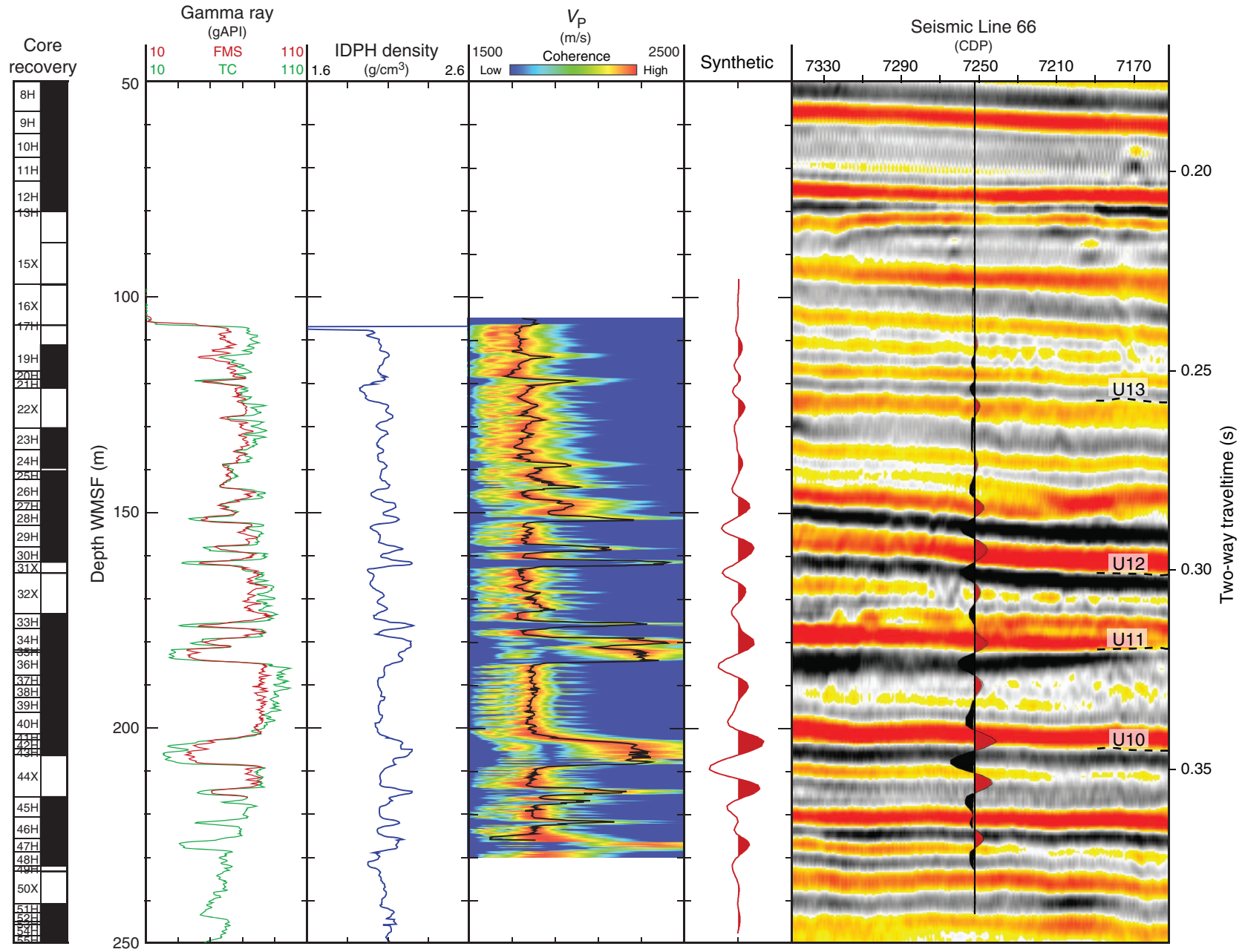


Figure F52. Depth-adjusted records of magnetic susceptibility and natural gamma radiation (NGR) data from Holes U1353A and U1353B. Gaps in the record represent positions where depth adjustments have been made to correlate key features. Dashed line = tentative correlation of the base of sand units, solid lines = key correlative horizons, shaded bars = sandy units (key correlative features present in both holes).

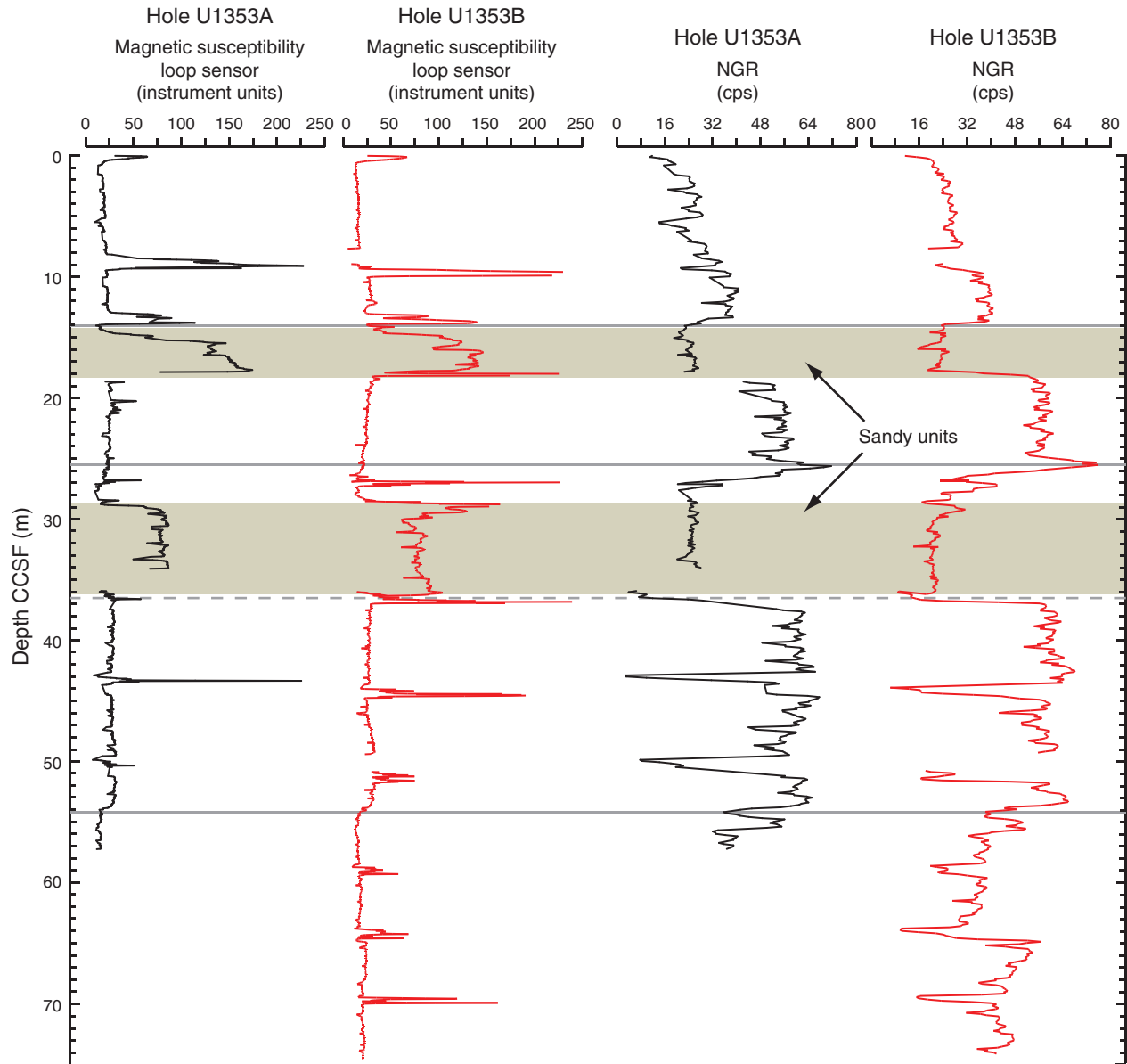


Table T1. Coring summary, Site U1353. (See table notes.) (Continued on next two pages.)

Hole U1353A

Latitude: 44°46.1079'S
 Longitude: 171°40.4368'E
 Time on hole (d): 0.36 (22 Dec, 0230 h–22 Dec, 1115 h)
 Seafloor (drill pipe measurement from rig floor, m DRF): 95.5 (APC mudline)
 Distance between rig floor and sea level (m): 11.3
 Water depth (drill pipe measurement from sea level, m): 84.2
 Total depth (drill pipe measurement from rig floor, m DRF): 151.5
 Total penetration (m DSF): 56.0
 Total length of cored section (m): 56.0
 Total core recovered (m): 56.38
 Core recovery (%): 101
 Total number of cores: 8

Hole U1353B

Latitude: 44°46.1203'S
 Longitude: 171°40.4407'E
 Time on hole (d): 4.40 (22 Dec, 1115 h–26 Dec, 2050 h)
 Seafloor (drill pipe measurement from rig floor, m DRF): 96.0 (APC mudline)
 Distance between rig floor and sea level (m): 11.3
 Water depth (drill pipe measurement from sea level, m): 84.7
 Total depth (drill pipe measurement from rig floor, m DRF): 710.3
 Total penetration (m DSF): 614.3
 Total length of cored section (m): 614.3
 Total core recovered (m): 211.48
 Core recovery (%): 34
 Total number of cores: 98

Hole U1353C

Latitude: 44°46.0982'S
 Longitude: 171°40.4380'E
 Time on hole (d): 2.01 (26 Dec, 2050 h–28 Dec, 2100 h)
 Seafloor (drill pipe measurement from rig floor, m DRF): 96.0 (by proxy, Hole U1353B)
 Distance between rig floor and sea level (m): 11.3
 Water depth (drill pipe measurement from sea level, m): 84.7
 Total depth (drill pipe measurement from rig floor, m DRF): 625.0
 Total penetration (m DSF): 529.0
 Total length of cored section (m): 0
 Total core recovered (m): 0
 Core recovery (%): 0
 Total number of cores: 0

Core	Date (2009)	UTC (h)	Top of cored interval (m DSF)	Bottom of cored interval (m DSF)	Interval advanced (m)	Top of recovered core (m CSF-A)	Bottom of recovered core (m CSF-A)	Length of core recovered (m)	Recovery (%)
317-U1353A-									
1H	21 Dec	1340	0.0	5.5	5.5	0.0	5.49	5.49	100
2H	21 Dec	1420	5.5	9.3	3.8	5.5	9.38	3.88	102
3H	21 Dec	1510	9.3	18.2	8.9	9.3	18.05	8.75	98
4H	21 Dec	1635	18.2	26.7	8.5	18.2	26.78	8.58	101
5H	21 Dec	1805	26.7	34.2	7.5	26.7	34.15	7.45	99
6H	21 Dec	1910	34.2	41.2	7.0	34.2	41.42	7.22	103
7H	21 Dec	2030	41.2	48.2	7.0	41.2	48.38	7.18	103
8H	21 Dec	2115	48.2	56.0	7.8	48.2	56.03	7.83	100
					Advanced total:	56.0			
					Total interval cored:	56.0			
317-U1353B-									
1H	21 Dec	2320	0.0	8.0	8.0	0.0	7.99	7.99	100
2H	22 Dec	0035	8.0	17.0	9.0	8.0	16.95	8.95	99
3H	22 Dec	0140	17.0	26.0	9.0	17.0	26.11	9.11	101
4H	22 Dec	0240	26.0	27.7	1.7	26.0	27.72	1.72	101
5H	22 Dec	0320	27.7	35.2	7.5	27.7	35.58	7.88	105
6H	22 Dec	0420	35.2	43.2	8.0	35.2	43.20	8.00	100
7H	22 Dec	0520	43.2	48.9	5.7	43.2	48.96	5.76	101
8H	22 Dec	0615	48.9	56.8	7.9	48.9	56.89	7.99	101
9H	22 Dec	0700	56.8	62.0	5.2	56.8	62.00	5.20	100
10H	22 Dec	0740	62.0	67.6	5.6	62.0	67.56	5.56	99
11H	22 Dec	0850	67.6	73.2	5.6	67.6	73.19	5.59	100
12H	22 Dec	1127	73.2	80.2	7.0	73.2	80.17	6.97	100
13H	22 Dec	1210	80.2	80.2	0.0	80.2	80.22	0.02	NA
14X	22 Dec	1315	80.2	87.4	7.2	80.2	80.71	0.00	0

Table T1 (continued). (Continued on next page.)

Core	Date (2009)	UTC (h)	Top of cored interval (m DSF)	Bottom of cored interval (m DSF)	Interval advanced (m)	Top of recovered core (m CSF-A)	Bottom of recovered core (m CSF-A)	Length of core recovered (m)	Recovery (%)
15X	22 Dec	1350	87.4	97.0	9.6	87.4	87.40	0.00	0
16X	22 Dec	1500	97.0	106.6	9.6	97.0	97.25	0.25	3
17H	22 Dec	1545	106.6	106.6	0.0	106.6	106.85	0.25	NA
18X	22 Dec	1710	106.6	111.2	4.6	106.6	108.49	1.89	41
19H	22 Dec	1745	111.2	117.2	6.0	111.2	117.09	5.89	98
20H	22 Dec	1855	117.2	119.2	2.0	117.2	119.21	2.01	100
21H	22 Dec	1930	119.2	121.2	2.0	119.2	121.21	2.01	100
22X	22 Dec	2025	121.2	130.4	9.2	121.2	121.20	0.00	0
23H	22 Dec	2115	130.4	135.4	5.0	130.4	135.76	5.36	107
24H	22 Dec	2210	135.4	140.4	5.0	135.4	139.72	4.32	86
25H	22 Dec	2325	140.4	142.4	2.0	140.4	142.91	2.51	125
26H	23 Dec	0010	142.4	147.4	5.0	142.4	147.44	5.04	101
27H	23 Dec	0140	147.4	149.4	2.0	147.4	149.73	2.33	116
28H	23 Dec	0255	149.4	153.0	3.6	149.4	153.00	3.60	100
29H	23 Dec	0350	153.0	158.1	5.1	153.0	158.11	5.11	100
30H	23 Dec	0545	158.1	161.4	3.3	158.1	161.41	3.31	100
31X	23 Dec	0715	161.4	164.1	2.7	161.4	161.62	0.22	8
32X	23 Dec	0805	164.1	173.6	9.5	164.1	164.20	0.10	1
33H	23 Dec	0845	173.6	177.0	3.4	173.6	177.05	3.45	101
34H	23 Dec	1035	177.0	181.9	4.9	177.0	181.84	4.84	99
35H	23 Dec	1140	181.9	182.6	0.7	181.9	182.55	0.65	93
36H	23 Dec	1255	182.6	187.8	5.2	182.6	187.84	5.24	101
37H	23 Dec	1350	187.8	190.1	2.3	187.8	190.11	2.31	100
38H	23 Dec	1525	190.1	193.0	2.9	190.1	193.01	2.91	100
39H	23 Dec	1630	193.0	196.4	3.4	193.0	196.43	3.43	101
40H	23 Dec	1735	196.4	201.4	5.0	196.4	201.45	5.05	101
41H	23 Dec	1930	201.4	202.9	1.5	201.4	202.84	1.44	96
42H	23 Dec	2030	202.9	205.0	2.1	202.9	205.03	2.13	101
43H	23 Dec	2125	205.0	206.3	1.3	205.0	206.32	1.32	102
44X	23 Dec	2225	206.3	216.1	9.8	206.3	206.47	0.17	2
45H	23 Dec	2325	216.1	220.8	4.7	216.1	220.85	4.75	101
46H	24 Dec	0010	220.8	225.8	5.0	220.8	225.81	5.01	100
47H	24 Dec	0210	225.8	228.7	3.0	225.8	228.73	2.93	98
48H	24 Dec	0320	228.8	232.1	3.3	228.8	232.13	3.33	101
49H	24 Dec	0430	232.1	233.4	1.3	232.1	232.10	0.00	0
50X	24 Dec	0530	233.4	240.9	7.5	233.4	233.71	0.00	0
51H	24 Dec	0610	240.9	242.9	2.0	240.9	242.95	2.05	102
52H	24 Dec	0700	242.9	245.1	2.2	242.9	245.11	2.21	100
53H	24 Dec	0735	245.1	245.8	0.7	245.1	245.88	0.78	111
54H	24 Dec	0805	245.8	248.3	2.5	245.8	248.36	2.56	102
55H	24 Dec	0945	248.3	250.2	1.9	248.3	250.19	1.89	99
56H	24 Dec	1220	250.2	251.6	1.4	250.2	251.68	1.48	106
57H	24 Dec	1320	251.6	253.6	2.0	251.6	253.55	1.95	98
58H	24 Dec	1415	253.6	254.9	1.3	253.6	254.88	1.28	98
59H	24 Dec	1535	254.9	256.1	1.2	254.9	256.09	1.19	99
60H	24 Dec	1655	256.1	257.7	1.6	256.1	257.74	1.64	102
61X	24 Dec	1805	257.7	263.2	5.5	257.7	258.12	0.42	8
62X	24 Dec	1905	263.2	269.6	6.4	263.2	263.49	0.29	5
63X	24 Dec	2000	269.6	279.2	9.6	269.6	270.96	1.36	14
64X	24 Dec	2150	279.2	288.8	9.6	279.2	280.13	0.93	10
65X	24 Dec	2230	288.8	298.4	9.6	288.8	290.43	1.63	17
66X	24 Dec	2315	298.4	308.0	9.6	298.4	300.38	1.98	21
67X	24 Dec	2355	308.0	317.6	9.6	308.0	308.32	0.32	3
68X	25 Dec	0035	317.6	327.2	9.6	317.6	319.12	1.52	16
69X	25 Dec	0130	327.2	336.8	9.6	327.2	327.86	0.66	7
70X	25 Dec	0215	336.8	346.0	9.2	336.8	337.38	0.58	6
71X	25 Dec	0255	346.0	355.6	9.6	346.0	347.16	1.16	12
72X	25 Dec	0400	355.6	365.2	9.6	355.6	355.99	0.39	4
73X	25 Dec	0445	365.2	374.8	9.6	365.2	365.74	0.54	6
74X	25 Dec	0540	374.8	384.4	9.6	374.8	375.04	0.24	2
75X	25 Dec	0630	384.4	394.0	9.6	384.4	385.17	0.77	8
76X	25 Dec	0735	394.0	403.6	9.6	394.0	394.28	0.28	3
77X	25 Dec	0845	403.6	413.2	9.6	403.6	403.60	0.00	0
78X	25 Dec	0955	413.2	422.8	9.6	413.2	413.82	0.62	6
79X	25 Dec	1100	422.8	432.3	9.5	422.8	432.29	0.00	0
80X	25 Dec	1145	432.3	441.9	9.6	432.3	432.68	0.38	4
81X	25 Dec	1235	441.9	451.5	9.6	441.9	442.27	0.37	4
82X	25 Dec	1400	451.5	461.1	9.6	451.5	451.50	0.00	0

Table T1 (continued).

Core	Date (2009)	UTC (h)	Top of cored interval (m DSF)	Bottom of cored interval (m DSF)	Interval advanced (m)	Top of recovered core (m CSF-A)	Bottom of recovered core (m CSF-A)	Length of core recovered (m)	Recovery (%)
83X	25 Dec	1440	461.1	470.7	9.6	461.1	461.30	0.20	2
84X	25 Dec	1535	470.7	480.3	9.6	470.7	470.70	0.00	0
85X	25 Dec	1625	480.3	489.9	9.6	480.3	480.69	0.39	4
86X	25 Dec	1720	489.9	500.0	10.1	489.9	490.26	0.36	4
87X	25 Dec	1900	500.0	509.6	9.6	500.0	500.21	0.21	2
88X	25 Dec	1940	509.6	518.6	9.0	509.6	510.57	0.97	11
89X	25 Dec	2020	518.6	528.2	9.6	518.6	518.71	0.11	1
90X	25 Dec	2110	528.2	537.5	9.3	528.2	528.92	0.72	8
91X	25 Dec	2150	537.5	547.1	9.6	537.5	537.88	0.38	4
92X	25 Dec	2235	547.1	556.6	9.5	547.1	547.33	0.23	2
93X	26 Dec	0005	556.6	566.2	9.6	556.6	557.30	0.70	7
94X	26 Dec	0120	566.2	575.8	9.6	566.2	566.46	0.26	3
95X	26 Dec	0220	575.8	585.4	9.6	575.8	576.52	0.72	8
96X	26 Dec	0310	585.4	595.0	9.6	585.4	585.96	0.56	6
97X	26 Dec	0400	595.0	604.6	9.6	595.0	595.25	0.25	3
98X	26 Dec	0445	604.6	614.3	9.7	604.6	604.65	0.05	1
				Advanced total:	614.3			211.98	34
				Total interval cored:	614.3				
317-U1353C-1D	27 Dec	1015							
					***** Drilled from 0.0 to 529.0 m *****				
				Advanced total:	529.0			0.00	0
				Total interval cored:	529.0				

Notes: APC = advanced piston corer. DRF = drilling depth below rig floor, DSF = drilling depth below seafloor, CSF-A = core depth below seafloor. UTC = Universal Time Coordinated. NA = not applicable.

Table T2. Lithologic surfaces and their interpretation, Site U1353. (See table note.)

Lithologic surface	Hole, core, section, interval (cm)	Depth CSF-A (m)	Overlying lithology	Nature of significant surface	Seismic sequence boundary	Predicted depth (m)	Preliminary biostratigraphy (Ma)
317-							
U1353A-S1	U1353A-3H-4, 1	13.80	Sand	Basal contact not recovered	U19	12	<0.29 (CN), possibly <0.1 (CN)
U1353B-S1	U1353B-2H-4, 45	13.00	Sand	Basal contact not recovered			
U1353A-S2	U1353A-5H-2, 1	27.97	Sand	Basal contact not recovered	U18	26	<0.29 (CN), possibly <0.1 (CN)
U1353B-S2	U1353B-4H-1, 95	26.95	Sand	Basal contact not recovered			
U1353B-S3	U1353B-9H-3, 88	60.68	Calcareous shelly mud	Sharp basal contact	U17	59	0.29–0.44 (CN)
U1353B-S6	U1353B-23H-2, 140	133.10	Calcareous muddy sand	Gradational upper and lower contacts	U13	112	1.69–1.73 (CN)
U1353B-S7	U1353B-28H-2, 40	151.30	Sandy marl	Sharp basal contact burrowed	U12	151	3.7 (CN)–4.3 (PF)
U1353B-S8	U1353B-34H-2, 50	179.00	Slump, shelly muddy sand	Upper sharp contacts	U10	192	3.7 (CN)–4.3 (PF)
U1353B-S9	U1353B-41H-CC, 33	202.83	Shelly muddy sand	Contacts not recovered	U9	241	3.7 (CN)–4.3 (PF)
U1353B-S10	U1353B-57H-1, 100	252.60	Shelly muddy sand	Gradational contacts	U8	290	3.7 (CN)–4.3 (PF)

Note: CN = calcareous nannofossil, PF = planktonic foraminifer.

Table T3. Microfossil bioevents, Site U1353. (See table notes.)

Core, section, interval (cm)		Microfossil	Bioevents, unconformities, and epoch boundaries	Age (Ma)	Depth CSF-A (m)				Comments
Top	Bottom				Top	Bottom	Midpoint	±	
317-U1353A-4H-CC	317-U1353A-5H-CC	CN	LO <i>Emiliana huxleyi</i> (NN21 base)	0.29 (± 0.03)	26.72	34.08	30.40	3.68	
317-U1353B-3H-CC	317-U1353B-4H-CC	CN	LO <i>Emiliana huxleyi</i> (NN21 base)	0.29 (± 0.03)	26.06	27.67	26.87	0.80	
4H-CC	4H-CC	PF	<i>Truncorotalia truncatulinoides</i>	<1.1	27.67	27.67	27.67	0.00	
8H-CC	9H-CC	BF	HO <i>Siphotexturalia wairoana</i>	0.34 (± 0.1)	56.84	61.90	59.37	2.53	
10H-CC	11H-CC	CN	HO <i>Pseudoemiliana lacunosa</i> (NN20 base)	0.44 (± 0.01)	67.50	73.19	70.35	2.84	
10H-CC	11H-CC	BF	HO <i>Bolivinita pliozea</i>	0.60 (± 0.2)	67.50	73.19	70.35	2.84	
12H-CC	14X-CC		Unconformity, ~0.8 m.y. missing		80.12	80.77	80.45	0.33	
12H-CC	14X-CC	CN	LO <i>Gephyrocapsa omega</i>	1.01 (± 0.2)	80.12	80.77	80.45	0.33	
12H-CC	14X-CC	CN	HO <i>Gephyrocapsa</i> >5.5 µm	1.26 (± 0.05)	80.12	80.77	80.45	0.33	
14X-CC	16X-CC	CN	HO <i>Helicosphaera sellii</i>	1.34 (± 0.01)	80.77	97.20	88.99	8.22	
16X-CC	18X-CC	CN	LO <i>Gephyrocapsa</i> >5.5 µm	1.56 (± 0.05)	97.20	108.44	102.82	5.62	
16X-CC	18X-CC	CN	LO <i>Gephyrocapsa</i> >4 µm	1.69 (± 0.05)	97.20	108.44	102.82	5.62	
20H-1, 107	21H-CC	CN	LO <i>Gephyrocapsa caribbeanica</i>	1.73 (± 0.01)	118.27	121.16	119.72	1.44	
21H-CC	23H-CC		Pliocene/Pleistocene boundary	1.81	121.16	135.71	128.44	7.28	
21H-CC	23H-CC		Unconformity, late Pliocene missing?		121.16	135.71	128.44	7.28	
21H-CC	23H-CC	CN	HO <i>Reticulofenestra ampla</i>	2.78 (± 0.1)	121.16	135.71	128.44	7.28	
24H-CC	25H-CC	PF	HO <i>Zeaglobigerina woodi</i>	2.7 (± 0.1)	139.67	142.86	141.27	1.60	
27H-CC	28H-1, 124	CN	HO <i>Reticulofenestra pseudoumbilicus</i>	3.70 (± 0.05)	149.68	150.64	150.16	0.48	
59H-CC	60H-CC	PF	LO <i>Globoconella inflata</i> s.s.	4.3 (± 0.3)	256.04	257.69	256.87	0.82	Poorly constrained
88X-CC	89X-CC	CN	HO <i>Cyclicargolithus floridanus</i>	12.04 (± 0.1)	510.52	518.66	514.59	4.07	Two specimens
98X-CC	98X-CC	CN	middle-early Miocene specimens of <i>Helicosphaera vedderi</i>		604.60	604.60	604.60		

Notes: CN = calcareous nannofossil, PF = planktonic foraminifer, BF = benthic foraminifer. LO = lowest occurrence, HO = highest occurrence. This table is also available in [ASCII](#).





Table T4. Calcareous nannofossil abundance, preservation, and distribution, Site U1353. This table is available in an [oversized format](#).

Table T5. Planktonic foraminiferal summary, Hole U1353A. (See table notes.)

Core, section, interval (cm)	Top depth CSF-A (m)	Interpreted age	NN zone	NZ stage correlation	NZ stage	Age (Ma)	Planktonic foraminifer (%)	Oceanicity	Key species and comments
317-U1353A-1H-1, 0	0.00	Holocene	NN21	Haweran (Wq)	Wq-uWo	0-4.3	4	Sheltered inner neritic	<i>Globoconella inflata</i>
1H-CC	5.44				Wq-uWo	0-4.3	4		<i>Globoconella inflata</i>
2H-CC	9.18				Wq-uWo	0-4.3	5		<i>Globoconella inflata</i> ; high-energy shallow inner shelf (inter-tidal) base of Holocene 12.94 m (from lithostratigraphy)
3H-CC	17.95	late Pleistocene	NN20	Castlecliffian (Wc)	Wq-uWo	0-4.3	2	Inner shelf	Shallow inner shelf
4H-CC	26.72				Wq-uWo	0-4.3	4		<i>Globoconella inflata</i>
5H-CC	34.08				Wq-uWc	0-1.1	7		<i>Truncorotalia truncatulinoides</i> , <i>Globoconella inflata</i> [abundant ostracods]
6H-CC	41.37				Wq-uWo	0-4.3	8		<i>Globoconella inflata</i>
7H-CC	48.33				15	ND			
8H-CC	55.97	Wq-uWo	0-4.3	8	<i>Globoconella inflata</i>				

Notes: ND = not determined. This table is also available in [ASCII](#).



Table T6. Planktonic foraminiferal summary, Hole U1353B. (See table notes.) (Continued on next two pages.)

Core, section, interval (cm)	Top depth CSF-A (m)	Interpreted age	NN zone	NZ stage correlation	NZ stage	Age (Ma)	Planktonic foraminifer (%)	Oceanicity	Key species and comments			
317-U1353B-												
1H-1, 0	0.00	Holocene	NN21		Wq	0–0.34	9	Inner neritic	Haweran benthic foraminifer <i>Loxostomum karrerianum</i>			
1H-CC	7.94							1		ND [NN21B <i>Emiliana huxleyi</i> acme zone]		
2H-CC	16.90	Pleistocene	NN20	Haweran to upper Mangapanian (Wq–uWm)			0	Sheltered inner neritic	Base of Holocene is at 12.94 m (from lithostratigraphy)			
3H-CC	26.06				Wq–uWo	0–4.3	2			<i>Globoconella inflata</i>		
4H-CC	27.67				Wq–uWc	0–1.1	1		<i>Truncorotalia truncatulinoides</i> , <i>Globoconella inflata</i>			
5H-CC	35.53						3		ND			
6H-CC	43.15				Wq–uWo	0–4.3	10	Inner neritic	<i>Globoconella inflata</i>			
7H-CC	48.91				Wq–uWo	0–4.3	31	Extraneritic	<i>Globoconella inflata</i>			
8H-CC	56.84				Wq–uWo	0–4.3	11	Inner neritic	<i>Globoconella inflata</i>			
9H-CC	61.90				Wq–uWo	0–4.3	1	Sheltered inner neritic	<i>Globoconella inflata</i>			
10H-CC	67.50				Wq–uWo	0–4.3	5		<i>Globoconella inflata</i>			
11H-CC	73.19						4		<i>Globoconella inflata</i>			
12H-CC	80.12			7	Inner neritic	<i>Globoconella inflata</i>						
13H-CC	80.20			1		[Nannofossil <i>Emiliana huxleyi</i> (common); suggests cave-in]						
14X-CC	80.77			1		<i>Globoconella inflata</i>						
16X-CC	97.20	NN19			Wq–uWo	0–4.3	2		<i>Globoconella inflata</i>			
17H-CC	106.80								Not examined; nannofossils indicate cave-in/flow-in			
18X-CC	108.44				Wq–uWo	0–4.3	5		<i>Globoconella inflata</i>			
19H-CC	117.04				Wq–uWo	0–4.3	2		<i>Globoconella inflata</i> ; nannofossils indicate cave-in/flow-in			
20H-CC	119.16						0		Not examined; nannofossils indicate cave-in/flow-in			
21H-CC	121.16				Wq–uWo	0–4.3	2		<i>Globoconella inflata</i>			
23H-CC	135.71						2		[Nannofossil datum <i>Reticulofenestra ampla</i> >2.7 Ma; HO possibly in Sample 21H-CC?]			
24H-CC	139.67				NN16				>2.7	0		ND; [macrofossil <i>Pellicaria convexa</i> (late Wn; 1.63–2.0 Ma in Hawkes Bay)]
25H-CC	142.86							IWm–uWo	2.7–4.3	3		HO <i>Zeaglobigerina woodi</i> , <i>Globoconella inflata</i>
26H-CC	147.39									1		ND
27H-CC	149.68	?IWm	>2.7?	1					<i>Zeaglobigerina</i> cf. <i>woodi</i> ?			
28H-CC	152.95	IWm–uWo	2.7–4.3	6					<i>Zeaglobigerina woodi</i> , <i>Globoconella inflata</i>			
29H-CC	158.06			1					ND, <i>Turborotalita quinqueloba</i> , <i>Globigerina</i> sp.			
30H-CC	161.36			1					ND, <i>Neogloboquadrina incompta</i> , <i>Globigerina</i> sp.			
31X-CC	161.67			0				Sheltered inner neritic	ND, no planktonics			
32X-CC	164.10			1					ND, <i>Globigerina</i> sp.			
33H-CC	177.00			0					ND, no planktonics [<i>Astrononion parki</i> ?, <i>Notorotalia hurupiensis</i> ?]			
34H-CC	181.79	Pliocene	NN15–NN12	lower Mangapanian to upper Opoitian (IWm–uWo)			0		Not examined; cave-in/flow-in?			
35H-CC	182.50						0		Not examined; nannofossils indicate cave-in/flow-in?			
36H-CC	187.79						0		Not examined; nannofossils indicate cave-in/flow-in?			
37H-CC	190.06						0		ND, no planktonics; cave-in/flow-in?			
38H-CC	192.96						0		ND, no planktonics; in situ firm sticky mud [<i>Nonionella flemingi</i> (dominant), <i>Notorotalia hurupiensis</i> , <i>A. parki</i>]			
39H-CC	196.38						0		ND, no planktonics			
40H-CC	201.40						0		ND, no planktonics			
41H-CC	202.79						1		ND, <i>Neogloboquadrina pachyderma</i> , <i>Neogloboquadrina incompta</i> , <i>Globigerina bulloides</i> , <i>Globigerina</i> sp.			
42H-CC	204.98						1		<i>Globoconella punctuloides</i>			
43H-CC	206.27						0		ND, no planktonics			
44X-CC	206.42			0		ND, no planktonics						
45H-CC	220.75			0		ND, no planktonics						
46H-CC	225.76			1		ND, <i>Neogloboquadrina pachyderma</i>						
47H-CC	228.68					Not examined						
48H-CC	232.08					0	ND, no planktonics					



Table T6 (continued). (Continued on next page.)

Core, section, interval (cm)	Top depth CSF-A (m)	Interpreted age	NN zone	NZ stage correlation	NZ stage	Age (Ma)	Planktonic foraminifer (%)	Oceanicity	Key species and comments	
49H-CC	—	Pliocene	NN15– NN12	lower Mangapanian to upper Opoitian (IWm–uWo)	IWm–uWo	2.7–4.3	0		No core catcher sample	
50X-CC	233.66								0	ND, no planktonics
51H-CC	242.90								0	ND, no planktonics
52H-CC	245.06								0	ND, no planktonics
53H-CC	245.83								0	ND, no planktonics
54H-CC	248.31								0	ND, no planktonics
55H-CC	250.14								<1	ND, <i>Turborotalita quinqueloba</i> , <i>Globigerina</i> sp.
56H-CC	251.63								2	<i>Globoconella inflata</i> , <i>Zeaglobigerina woodi</i> , <i>Neogloboquadrina pachyderma</i> , <i>Neogloboquadrina incompta</i> [coincides with a peak in nannofossil abundance]
57H-CC	253.50								<1	ND, <i>Globigerina</i> sp.
58H-CC	254.83								<1	ND, <i>Globigerina</i> sp.
59H-CC	256.04	<1	LO <i>Globoconella inflata</i> , <i>Turborotalita</i> cf. <i>quinqueloba</i> , <i>Globigerina</i> sp.; lowest planktonic assemblage							
60H-CC	257.69	early Pliocene to Miocene	NN15– NN11	ND				Sheltered inner neritic	ND, no planktonics	
61X-CC	258.07								0	ND, no planktonics
62X-CC	263.44								0	ND, no planktonics
63X-CC	270.91								0	ND, no planktonics
64X-CC	280.08								0	ND, no planktonics
65X-CC	290.38								<1	ND, <i>Globigerina bulloides</i>
66X-CC	300.33								<1	ND, <i>Globigerina</i> sp.
67X-CC	308.27								0	ND, no planktonics
68X-CC	319.07								0	ND, no planktonics
69X-CC	327.80								0	ND, no planktonics
70X-CC	337.33								0	ND, no planktonics
71X-CC	347.11								0	ND, no planktonics
72X-CC	355.94								0	ND, no planktonics
73X-CC	365.69								0	ND, no planktonics
74X-CC	374.99								0	ND, no planktonics
75X-CC	385.12								0	ND, no planktonics
76X-CC	394.23								0	ND, no planktonics
78X-CC	413.77								0	ND, no planktonics
79X-CC	423.24								0	ND, no planktonics
80X-CC	432.63								0	ND, no planktonics
81X-CC	444.22	0	ND, no planktonics							
83X-CC	461.26	0	ND, no planktonics							
85X-CC	480.64	0	ND, no planktonics							
86X-CC	490.21	0	ND, no planktonics							
87X-CC	500.16	0	ND, no planktonics							
88X-CC	510.52	0	ND, no planktonics							
89X-CC	518.66	0	ND, no planktonics [nannofossil marker >12.03 Ma; same species occurs at Site U1351 with ITt planktonic foraminifers]							
90X-CC	528.87	0	ND, no planktonics [nannofossil marker >12.03 Ma; same species occurs at Site U1351 with ITt planktonic foraminifers]							
91X-CC	537.83	0	ND, no planktonics [nannofossils virtually absent between Samples 91X-CC and 97X-CC; very poor benthic assemblage]							
92X-CC	547.28	middle Miocene?	NN6?	ND					ND, no planktonics	
93X-CC	557.25								1	ND, <i>Globigerina</i> sp. (11 benthics and 1 planktonic)
94X-CC	566.41								0	ND, no planktonics
95X-CC	576.47								0	ND, no planktonics
96X-CC	585.91								0	ND, no planktonics
97X-CC	595.20								0	ND, no planktonics

Table T8 (continued).

Core, section, interval (cm)	Top depth CSF-A (m)	Foraminiferal abundance	Foraminiferal preservation	Planktonic foraminifer (%)	Planktonic foraminifers										Miscellaneous					Comments									
					<i>Globigerina bulloides</i>	<i>Globigerina falconensis</i>	<i>Globigerina</i> spp.	<i>Globigerinella aequilateralis</i>	<i>Globigerinita glutinata</i>	<i>Globigerinopsis obesa</i>	<i>Globoconella inflata</i>	<i>Globoconella punctuloides</i>	<i>Hirsutella scitula</i>	<i>Neogloboquadrina dutertrei</i>	<i>Neogloboquadrina incompta</i>	<i>Neogloboquadrina pachyderma</i>	<i>Orbulina universa</i>	<i>Turborotalita quinqueloba</i>	<i>Turborotalita</i> sp.		<i>Truncotalia truncatulinoides</i>	<i>Zeaglobierina woodi</i>	Bryozoa fragments	Echinoid plate fragments	Echinoid spines	Fish teeth	Ostracods	Otoliths	Radiolarians
59H-CC	256.04	A	G	0		X				X											F		F				F	A	
60H-CC	257.69	A	G	<1		X						X	X															A	
61X-CC	258.07	A	G	<1		X															R		R					A	
62X-CC	263.44	A	G	0																	F		R	F				D	
63X-CC	270.91	C	G	0																								A	
64X-CC	280.08	F	G	0																	C								
65X-CC	290.38	A	G	<1	X																							A	
66X-CC	300.33	A	G	<1		X																						A	
67X-CC	308.27	A	G	0																								A	
68X-CC	319.07	A	G	0																								A	
69X-CC	327.80	C	M	0																								D	
70X-CC	337.33	A	M	0																								A	
71X-CC	347.11	F	G	0																								A	
72X-CC	355.94	R	P	0																								C	
73X-CC	365.69	A	M	0																								A	
74X-CC	374.99	C	G	0																	R							A	
75X-CC	385.12	R	G	0																								D	
76X-CC	394.23	F	G	0																								A	
78X-CC	413.77	A	G	0																								A	
79X-CC	423.24	C	G	0																								A	
80X-CC	432.63	C	G	0																			R					A	
81X-CC	442.22	C	M	0																								A	
83X-CC	461.26	F	M	0																								C	
85X-CC	480.64	F	G	0																								A	
86X-CC	490.21	A	G	0																								A	
87X-CC	500.16	C	M	0																								C	
88X-CC	510.52	C	G	0																			R	R				C	
89X-CC	518.66	A	G	0																			R					D	
90X-CC	528.87	A	G	0																								C	
91X-CC	537.83	F	M	0																			R					A	
92X-CC	547.28	R	M	0																								F	
93X-CC	557.25	R	G	9		X																	F					F	
50X-CC	566.41	R	M	0																								R	
95X-CC	576.47	C	G	0																								A	
96X-CC	585.91	—	—	—																								R	
97X-CC	595.20	R	M	0																								A	Barren
98X-CC	604.60	F	G	0																								R	

Notes: Abundance: D = dominant, A = abundant, C = common, F = few, R = rare, X = present, ? = questionable presence. Preservation: G = good, M = moderate, P = poor. — = no data. This table is also available in [ASCII](#).

Table T9. Benthic foraminifer abundance, preservation, and distribution, Site U1353. This table is available in an [oversized format](#).



Table T10. Diatom abundance, preservation, and distribution, Site U1353. (See table notes.) (Continued on next page.)

Core, section	Top depth CSF-A (m)	Abundance		Preservation	Marine					Coastal upwelling		Coastal		Fresh or brackish water		Comments
		C	M		<i>Coccolodiscus marginatus</i>	<i>Grammatophora</i> sp.	<i>Hyalodiscus</i> sp.	<i>Thalassiosira oestrupii</i>	<i>Thalassiosira</i> spp.	Resting spores of <i>Chaetoceros</i>	<i>Paralia sulcata</i>	<i>Thalassionema nitzschoides</i>	Gen. et sp. indet.			
317-U1353A-																
1H-CC	5.44	C	M			X	X		X		C		X			
2H-CC	9.33	B	—													
3H-CC	17.95	B	—													
4H-CC	26.72	B	—													
5H-CC	34.08	B	—													
6H-CC	41.37	B	—													
7H-CC	48.33	B	—													
8H-CC	55.97	X	P													
317-U1353B-																
1H-CC	7.94	C	M		X	X	X	X	R		C	X				
2H-CC	16.90	B	—													
3H-CC	26.06	B	—													
4H-CC	27.67	B	—													
5H-CC	35.53	B	—													
6H-CC	43.15	B	—													
7H-CC	48.91	B	—													
8H-CC	56.84	B	—													
9H-CC	61.90	B	—													
10H-CC	67.50	B	—													
11H-CC	73.19	B	—													
12H-CC	80.12	X	P								X					Caved
13H-CC	80.20	B	—								X	X				
14X-CC	80.77	B	—													
16X-CC	97.20	B	—													
17H-CC	106.80	B	—													
18X-CC	108.44	B	—													
19H-CC	117.04	X	P								X					Caved
20H-CC	119.16	B	—													
21H-CC	121.16	B	—													
23H-CC	135.71	B	—													
24H-CC	139.67	B	—													
25H-CC	142.86	B	—													
26H-CC	147.39	B	—													
27H-CC	149.68	B	—													
28H-CC	152.95	B	—													
29H-CC	158.06	B	—													
30H-CC	161.36	B	—													
31X-CC	161.67	B	—													
32X-CC	164.10	B	—													
33H-CC	177.00	B	—													
34H-CC	181.79	B	—													
35H-CC	182.50	B	—													
36H-CC	187.79	B	—													
37H-CC	190.06	B	—													
38H-CC	192.96	B	—													
39H-CC	196.38	B	—													
40H-CC	201.40	B	—													
41H-CC	202.79	B	—													
42H-CC	204.98	B	—													
43H-CC	206.27	B	—													
44X-CC	206.42	B	—													
45H-CC	220.75	B	—													
46H-CC	225.76	B	—													
47H-CC	228.68	B	—													
48H-CC	232.08	B	—													
50X-CC	233.66	B	—													
51H-CC	242.90	B	—													

All samples barren from Sections 20H-CC through 98X-CC



Table T10 (continued).

Core, section	Top depth CSF-A (m)	Abundance	Preservation	Marine <i>Coscinodiscus marginatus</i> <i>Grammatophora</i> sp. <i>Hyalodiscus</i> sp. <i>Thalassiosira oestrupii</i> <i>Thalassiosira</i> spp.	Coastal upwelling Resting spores of <i>Chaetoceros</i>	Coastal <i>Paralia sulcata</i> <i>Thalassionema nitzschioides</i>	Fresh or brackish water Gen. et sp. indet.	Comments
52H-CC	245.06	B	—					
53H-CC	245.83	B	—					
54H-CC	248.31	B	—					
55H-CC	250.14	B	—					
56H-CC	251.63	B	—					
57H-CC	253.50	B	—					
58H-CC	254.83	B	—					
59H-CC	256.04	B	—					
60H-CC	257.69	B	—					
61X-CC	258.07	B	—					
62X-CC	263.44	B	—					
63X-CC	270.91	B	—					
64X-CC	280.08	B	—					
65X-CC	290.38	B	—					
66X-CC	300.33	B	—					
67X-CC	308.27	B	—					
68X-CC	319.07	B	—					
69X-CC	327.80	B	—					
70X-CC	337.33	B	—					
71X-CC	347.11	B	—					
72X-CC	355.94	B	—					
73X-CC	365.69	B	—					
74X-CC	374.99	B	—					
75X-CC	385.12	B	—					
76X-CC	394.23	B	—					
78X-CC	413.77	B	—					
79X-CC	423.24	B	—					
80X-CC	432.63	B	—					
81X-CC	442.22	B	—					
83X-CC	461.26	B	—					
85X-CC	480.64	B	—					
86X-CC	490.21	B	—					
87X-CC	500.16	B	—					
88X-CC	510.52	B	—					
89X-CC	518.66	B	—					
90X-CC	528.87	B	—					
91X-CC	537.83	B	—					
92X-CC	547.28	B	—					
93X-CC	557.25	B	—					
94X-CC	566.41	B	—					
96X-CC	585.91	B	—					
97X-CC	595.20	B	—					
98X-CC	604.60	B	—					

All samples barren from
Sections 20H-CC through
98X-CC

Notes: Abundance: C = common, B = barren, R = rare, X = present. Preservation: M = moderate, P = poor, — = no data. This table is also available in [ASCII](#).

Table T11. Invertebrate macrofossils. This table is available in an [oversized format](#).

Table T12. Headspace gas composition from sediments, Site U1353. (See table note.)

Core, section, interval (cm)	Depth CSF-A (m)	C ₁ (ppmv)	C ₁ (mM)
317-U1353A-			
1H-2, 0	1.50	3.5	0.00104
1H-3, 0	3.00	3.9	0.00116
1H-4, 0	4.50	2.7	0.00080
2H-2, 0	7.00	2.5	0.00074
2H-3, 0	8.50	3.9	0.00118
3H-2, 0	10.80	2.4	0.00073
3H-4, 0	13.80	2.4	0.00073
3H-6, 0	16.51	1.8	0.00054
4H-2, 0	19.70	2.4	0.00073
4H-4, 0	22.70	3.2	0.00096
4H-6, 0	25.70	2.7	0.00080
5H-2, 0	27.97	5.9	0.00176
5H-4, 0	30.44	1.8	0.00055
5H-6, 0	32.93	2.3	0.00068
6H-2, 0	35.70	3.0	0.00091
6H-4, 125	38.70	3.1	0.00092
6H-4, 0	39.95	2.7	0.00082
7H-2, 0	42.70	2.7	0.00080
7H-4, 0	45.70	2.2	0.00065
7H-5, 0	47.20	3.3	0.00100
8H-2, 0	49.54	3.2	0.00097
8H-4, 0	52.54	3.7	0.00112
8H-5, 0	54.04	2.8	0.00084
317-U1353B-			
8H-6, 0	55.90	3.8	0.00113
9H-3, 0	59.80	3.2	0.00097
9H-4, 0	61.30	2.9	0.00088
10H-2, 0	63.50	3.3	0.00099
10H-4, 0	66.50	2.8	0.00084
11H-2, 0	69.10	3.1	0.00092
11H-4, 0	72.10	2.9	0.00087
18X-1, 0	106.60	1.8	ND
19H-3, 0	113.18	2.0	ND
21H-1, 96	120.16	2.0	ND
23H-2, 0	131.70	1.7	ND
25H-2, 0	141.70	2.9	ND
28H-3, 0	152.20	2.4	ND
34H-2, 0	178.50	1.7	ND
36H-2, 145	185.55	1.5	ND
37H-2, 130	189.63	1.7	ND
38H-2, 0	191.55	1.9	ND
39H-2, 0	194.06	1.8	ND
40H-1, 138	197.78	1.6	ND
45H-3, 0	219.10	2.2	ND
52H-2, 0	244.40	2.7	ND
57H-2, 0	252.7	1.5	ND
57H-2, 0	252.7	2.6	ND
58H-1, 105	254.65	1.9	ND
60H-1, 138	257.48	2.1	ND
63X-1, 80	270.4	2.2	ND
65X-1, 0	288.8	3.2	ND
66X-2, 0	299.5	3.4	ND
68X-1, 89	318.49	2.9	ND
69X-1, 42	327.62	2.5	ND
71X-1, 71	346.71	3.4	ND
75X-1, 41	384.81	7.8	ND
93X-1, 38	556.98	5.1	ND
95X-1, 22	576.02	32.3	ND
96X-1, 14	585.54	3.6	ND

Note: ND = not determined.

Table T13. Core void gas composition, Site U1353. (See table notes.)

Core, section, interval (cm)	Depth CSF-A (m)	C ₁ (ppmv)	C ₂ (ppmv)	C ₃ (ppmv)	n-C ₄ (ppmv)	i-C ₄ (ppmv)	CO ₂ (ppmv)	C ₁ /C ₂	n-C ₄ /(i-C ₄ + n-C ₄) (%)
U1353A-5H-5, 122	32.93	717	2.5	0.42	0.16	0.31	1352.2	284	34
U1353B-9H-4, 45	61.75	4	0.0	0.0	0.0	0.0	144.5	ND	ND
10H-3, 87	65.87	311	1.9	0.0	0.0	0.0	159.4	163	ND
10H-4, 85	67.35	4	0.0	0.0	0.0	0.0	93.8	ND	ND

Notes: C₁–C₂ analyzed on GC3. C₃–C₆ analyzed on natural gas analyzer (NGA) and normalized to methane in GC3 analysis. CO₂ analyzed by thermal conductivity detector on NGA. ND = not determined.

Table T14. Carbon and nitrogen analyses of sediments, Hole U1353B. (See table notes.) (Continued on next page.)

Core, section, interval (cm)	Depth CSF-A (m)	IC (wt%)	CaCO ₃ (wt%)	TC (wt%)	TN (wt%)	TOC _{DIFF} (wt%)	TOC _{SRA} (wt%)	TOC _{DIFF} /TN
317-U1353B-1H-2, 67	2.17	2.25	18.75	3.01	0.077	0.76	1.51	9.9
1H-5, 26	6.26	0.91	7.60	1.77	0.069	0.86	1.31	12.4
2H-1, 20	8.20	0.84	7.01	1.71	0.064	0.87	1.42	13.6
2H-2, 141	10.91	0.85	7.09	1.38	0.038	0.53	1.11	14.0
3H-1, 79	17.79	1.14	9.51	1.55	0.039	0.41	0.60	10.6
4H-1, 92	26.92	0.94	7.79	1.30	0.024	0.36	0.84	15.0
5H-1, 72	28.42	0.47	3.89	0.51	0.003	0.04	0.66	12.8
6H-3, 145	39.65	0.22	1.82	0.65	0.038	0.43	0.65	11.3
6H-4, 70	40.40	0.78	6.50	1.16	0.048	0.38	ND	8.0
7H-4, 89	48.59	0.36	3.01	0.67	0.036	0.31	0.89	8.5
8H-2, 88	51.28	0.53	4.40	0.70	0.040	0.17	0.57	4.3
9H-1, 75	57.55	3.50	29.12	4.23	0.074	0.73	1.61	9.9
9H-4, 13	61.43	0.92	7.69	1.40	0.022	0.48	0.82	22.0
10H-4, 96	67.46	2.34	19.53	2.64	0.036	0.30	0.84	8.2
11H-3, 53	71.13	2.20	18.36	2.62	0.049	0.42	1.02	8.6
11H-4, 72	72.82	2.04	17.01	2.49	0.044	0.45	1.06	10.2
12H-3, 2	75.20	1.52	12.69	1.75	0.026	0.23	0.81	8.8
12H-3, 123	76.41	0.66	5.49	0.83	0.018	0.17	0.63	9.4
18X-1, 73	107.33	0.56	4.68	0.69	0.019	0.13	0.55	6.9
18X-1, 105	107.65	1.05	8.71	1.14	0.015	0.09	0.55	6.1
19H-2, 72	112.75	1.27	10.57	1.33	0.023	0.06	0.67	2.6
19H-3, 132	114.50	1.69	14.05	1.93	0.020	0.24	0.79	12.3
20H-1, 82	118.02	0.40	3.31	0.50	0.021	0.10	0.49	4.9
23H-3, 131	134.51	0.27	2.22	0.39	0.021	0.12	0.57	5.9
24H-3, 7	137.43	1.60	13.29	1.84	0.026	0.24	0.47	9.4
25H-2, 54	142.24	1.96	16.35	2.39	0.031	0.43	0.82	13.8
26H-2, 78	144.68	0.25	2.04	0.43	0.023	0.18	0.62	7.9
27H-1, 37	147.77	5.85	48.70	6.15	0.011	0.30	0.54	28.4
28H-2, 13	151.03	6.84	57.00	7.27	0.014	0.43	0.34	30.1
28H-3, 48	152.68	0.25	2.10	0.41	0.020	0.16	0.36	7.7
29H-1, 81	153.81	0.24	1.97	0.42	0.027	0.18	0.33	6.9
33H-1, 39	173.99	0.23	1.94	0.43	0.028	0.20	0.38	7.0
34H-1, 126	178.26	0.30	2.52	0.53	0.028	0.23	0.54	8.0
37H-2, 14	188.47	0.13	1.10	0.3	0.030	0.17	0.52	5.7
39H-1, 53	193.53	0.04	0.32	0.19	0.020	0.15	0.27	7.5
39H-1, 72	193.72	0.06	0.51	0.27	0.027	0.21	0.42	7.6
40H-2, 102	198.95	0.14	1.13	0.4	0.037	0.26	0.40	7.2
41H-1, 80	202.20	5.69	47.41	6.49	0.035	0.80	0.69	23.0
45H-1, 96	217.06	0.11	0.94	0.32	0.029	0.21	0.41	7.1
46H-2, 28	221.34	0.27	2.27	0.58	0.027	0.31	0.53	11.4
47H-1, 24	226.04	4.86	40.50	5.27	0.011	0.41	0.42	37.1
48H-1, 49	229.29	0.10	0.84	0.16	0.014	0.06	0.38	4.1
52H-2, 7	244.47	0.14	1.14	0.29	0.027	0.15	ND	5.6
53H-1, 59	245.69	0.10	0.87	0.28	0.020	0.18	0.37	8.8
55H-2, 99	249.63	0.39	3.22	0.47	0.017	0.08	0.42	5.1
56H-1, 93	251.13	1.95	16.22	2.04	0.012	0.09	0.65	7.7
56H-1, 136	251.56	0.68	5.69	1.3	0.024	0.62	0.38	25.9
57H-1, 58	252.18	1.39	11.58	2.12	0.018	0.73	0.30	40.3

Table T14 (continued).

Core, section, interval (cm)	Depth CSF-A (m)	IC (wt%)	CaCO ₃ (wt%)	TC (wt%)	TN (wt%)	TOC _{DIFF} (wt%)	TOC _{SRA} (wt%)	TOC _{DIFF} /TN
58H-1, 59	254.19	2.47	20.58	2.6	0.019	0.13	0.22	7.0
58H-1, 86	254.46	0.26	2.17	0.33	0.024	0.07	1.27	2.9
59H-1, 11	255.01	2.52	20.98	2.55	0.015	0.03	0.55	2.1
60H-1, 124	257.34	0.41	3.38	0.61	0.021	0.20	0.50	10.0
61X-CC, 25	257.95	1.91	15.87	2.06	0.013	0.15	0.55	11.7
62X-CC, 17	263.37	0.09	0.74	0.26	0.032	0.17	0.37	5.3
63X-1, 59	270.19	0.06	0.54	0.23	0.032	0.17	0.51	5.2
63X-CC, 10	270.55	0.10	0.82	0.28	0.035	0.18	0.38	5.2
64X-1, 41	279.61	0.13	1.07	0.30	0.022	0.17	0.38	7.9
65X-1, 84	289.64	0.14	1.20	0.33	0.019	0.19	0.41	9.9
66X-1, 81	299.21	0.17	1.45	0.40	0.023	0.23	0.41	9.9
66X-1, 103	299.43	0.17	1.43	0.37	0.020	0.20	0.38	9.7
67X-CC, 9	308.09	0.23	1.88	0.40	0.020	0.17	0.60	8.9
68X-1, 65	318.25	0.19	1.55	0.40	0.023	0.21	0.88	9.5
68X-CC, 26	318.90	0.18	1.49	0.40	0.018	0.22	0.36	12.1
69X-1, 28	327.48	0.20	1.67	0.38	0.017	0.18	0.34	10.7
70X-CC, 15	336.95	0.08	0.70	0.22	0.016	0.14	0.25	8.5
71X-1, 39	346.39	0.15	1.26	0.33	0.017	0.18	0.41	10.4
72X-CC, 25	355.85	0.98	8.16	1.18	0.012	0.20	0.45	17.1
73X-1, 47	365.67	0.24	1.98	0.33	0.017	0.09	0.26	5.5
75X-1, 43	384.83	0.05	0.41	0.22	0.021	0.17	0.36	8.0
75X-1, 61	385.01	0.04	0.36	0.20	0.016	0.16	0.33	10.0
78X-1, 35	413.55	0.29	2.44	0.54	0.013	0.25	0.36	18.4
78X-1, 50	413.70	0.30	2.52	0.46	0.015	0.16	0.28	10.5
86X-CC, 11	490.01	0.43	3.61	0.53	0.014	0.10	0.42	7.0
88X-1, 49	510.09	0.06	0.54	0.17	0.013	0.11	0.28	7.9
90X-CC, 12	528.66	0.14	1.13	0.26	0.014	0.12	0.29	8.7
91X-CC, 13	537.63	0.50	4.15	0.58	0.011	0.08	0.33	7.2
92X-CC, 0	547.10	4.74	39.49	4.95	0.008	0.21	0.20	26.9
93X-1, 22	556.82	0.06	0.51	0.22	0.022	0.16	0.30	7.3
94X-CC, 17	566.37	0.05	0.41	0.11	0.012	0.06	0.20	5.2
95X-1, 48	576.28	0.07	0.61	0.23	0.015	0.16	0.27	10.5
96X-1, 17	585.57	0.07	0.56	0.17	0.013	0.10	0.19	7.8
97X-CC, 13	595.13	0.10	0.83	0.21	0.013	0.11	0.31	8.7

Notes: Inorganic carbon (IC) is from coulometric measurement of acid-evolved CO₂. CaCO₃ is calculated from IC × 8.33. Total carbon (TC) and total nitrogen (TN) are from elemental analysis of sediments. TOC_{DIFF} = total organic carbon from difference of TC and IC. TOC_{SRA} = total organic carbon from source rock analyzer pyrolysis (see Table T15).



Table T15. Source rock analyzer pyrolysis evaluation of organic matter in sediments, Site U1353. (See table notes.) (Continued on next page.)

Core, section, interval (cm)	Depth CSF-A (m)	S ₁ (mg HC/g rock)	S ₂ (mg HC/g rock)	S ₃ (mg CO ₂ /g rock)	T _{max} (°C)	TOC _{SRA} (wt%)	Hydrogen index (mg S ₂ /g TOC)	Oxygen index (mg S ₃ /g TOC)	Pyrolysis carbon	Production index
317-U1353B-										
1H-2, 67	2.17	0.23	1.03	1.92	415.7	1.51	68.2	127.2	0.105	18.3
1H-5, 26	6.26	0.20	0.88	1.99	419.9	1.31	67.2	151.9	0.090	18.5
2H-1, 20	8.20	0.18	0.81	1.93	420.6	1.42	57.0	135.9	0.082	18.2
2H-2, 141	10.91	0.11	0.50	0.93	419.0	1.11	45.0	83.8	0.051	18.0
3H-1, 79	17.79	0.06	0.23	0.09	417.3	0.60	38.3	15.0	0.024	20.7
4H-1, 92	26.92	0.08	0.35	0.66	415.1	0.84	41.7	78.6	0.036	18.6
5H-1, 72	28.42	0.03	0.11	ND	ND	0.66	16.7	ND	0.017	21.4
6H-3, 145	39.65	0.06	0.26	0.23	413.3	0.65	40.0	35.4	0.027	18.8
6H-4, 70	40.40	0.09	ND	0.50	ND	ND	54.2	52.1	ND	ND
7H-4, 89	48.59	0.05	0.20	0.10	412.8	0.89	22.5	11.2	0.021	20.0
8H-2, 88	51.28	0.06	0.20	ND	402.5	0.57	35.1	ND	0.022	23.1
9H-1, 75	57.55	0.20	1.23	3.81	421.2	1.61	76.4	236.6	0.119	14.0
9H-4, 13	61.43	0.07	0.28	0.35	409.9	0.82	34.1	42.7	0.029	20.0
10H-4, 96	67.46	0.07	0.31	0.35	406.1	0.84	36.9	41.7	0.032	18.4
11H-3, 53	71.13	0.11	0.58	1.60	415.9	1.02	56.9	156.9	0.057	15.9
11H-4, 72	72.82	0.11	0.58	1.78	418.4	1.06	54.7	167.9	0.057	15.9
12H-3, 2	75.20	0.06	0.28	0.56	415.5	0.81	34.6	69.1	0.028	17.7
12H-3, 123	76.41	0.05	0.23	ND	421.8	0.63	36.5	ND	0.023	17.9
18X-1, 73	107.33	0.03	0.12	ND	ND	0.55	21.8	ND	0.013	20.0
18X-1, 105	107.65	0.04	0.14	ND	399.7	0.55	25.5	ND	0.015	22.2
19H-2, 72	112.75	0.04	0.15	ND	409.7	0.67	22.4	ND	0.016	21.1
19H-3, 132	114.50	0.05	0.18	ND	413.4	0.79	22.8	ND	0.019	21.7
20H-1, 82	118.02	0.04	0.14	ND	407.7	0.49	28.6	ND	0.015	22.2
23H-3, 131	134.51	0.04	0.14	ND	ND	0.57	24.6	ND	0.015	22.2
24H-3, 7	137.43	0.07	0.26	0.20	411.7	0.47	55.3	42.6	0.027	21.2
25H-2, 54	142.24	0.08	0.35	0.54	403.6	0.82	42.7	65.9	0.036	18.6
26H-2, 78	144.68	0.04	0.14	0.06	417.5	0.62	22.6	9.7	0.015	22.2
27H-1, 37	147.77	0.04	0.11	0.18	390.4	0.54	20.4	33.3	0.013	26.7
28H-2, 13	151.03	0.05	0.14	0.52	394.6	0.34	41.2	152.9	0.016	26.3
28H-3, 48	152.68	0.03	0.09	ND	ND	0.36	25.0	ND	0.010	25.0
29H-1, 81	153.81	0.04	0.12	ND	ND	0.33	36.4	ND	0.013	25.0
33H-1, 39	173.99	0.03	0.11	ND	ND	0.38	28.9	ND	0.012	21.4
34H-1, 126	178.26	0.04	0.13	0.07	417.5	0.54	24.1	13.0	0.014	23.5
37H-2, 14	188.47	0.03	0.09	ND	ND	0.52	17.3	ND	0.010	25.0
39H-1, 53	193.53	0.03	0.08	ND	ND	0.27	29.6	ND	0.009	27.3
39H-1, 72	193.72	0.04	0.12	ND	ND	0.42	28.6	ND	0.013	25.0
40H-2, 102	198.95	0.11	0.38	ND	ND	0.40	95.0	ND	0.041	22.5
41H-1, 80	202.20	ND	0.45	1.32	410.5	0.69	65.2	191.3	ND	ND
45H-1, 96	217.06	0.10	0.32	ND	ND	0.41	78.0	ND	0.035	23.8
46H-2, 28	221.34	0.07	0.22	0.03	402.7	0.53	41.5	5.7	0.024	24.1
47H-1, 24	226.04	0.04	0.10	ND	404.1	0.42	23.8	ND	0.012	28.6
48H-1, 49	229.29	0.07	0.26	ND	ND	0.38	68.4	ND	0.027	21.2
52H-2, 7	244.47	ND	ND	ND	ND	ND	ND	ND	ND	ND
53H-1, 59	245.69	0.04	0.12	ND	405.0	0.37	32.4	ND	0.013	25.0
55H-2, 99	249.63	0.08	0.30	ND	406.4	0.42	71.4	ND	0.032	21.1
56H-1, 93	251.13	0.04	0.11	ND	ND	0.65	16.9	ND	0.013	26.7
56H-1, 136	251.56	0.07	0.22	0.02	413.7	0.38	57.9	5.3	0.024	24.1
57H-1, 58	252.18	0.08	0.29	0.04	411.9	0.30	96.7	13.3	0.031	21.6
58H-1, 59	254.19	0.08	0.28	ND	395.6	0.22	127.3	ND	0.030	22.2
58H-1, 86	254.46	0.09	0.33	ND	413.3	1.27	26.0	ND	0.035	21.4



Table T15 (continued).

Core, section, interval (cm)	Depth CSF-A (m)	S ₁ (mg HC/g rock)	S ₂ (mg HC/g rock)	S ₃ (mg CO ₂ /g rock)	T _{max} (°C)	TOC _{SRA} (wt%)	Hydrogen index (mg S ₂ /g TOC)	Oxygen index (mg S ₃ /g TOC)	Pyrolysis carbon	Production index
59H-1, 11	255.01	0.09	0.34	ND	420.0	0.55	61.8	ND	0.036	20.9
60H-1, 124	257.34	0.09	0.31	ND	394.2	0.50	62.0	ND	0.033	22.5
61X-CC, 25	257.95	0.11	0.33	ND	402.2	0.55	60.0	ND	0.037	25.0
62X-CC, 17	263.37	0.09	0.31	ND	ND	0.37	83.8	ND	0.033	22.5
63X-1, 59	270.19	0.09	0.33	ND	419.5	0.51	64.7	ND	0.035	21.4
63X-CC, 10	270.55	0.05	0.11	ND	ND	0.38	28.9	ND	0.013	31.3
64X-1, 41	279.61	0.05	0.15	ND	392.7	0.38	39.5	ND	0.013	31.3
65X-1, 84	289.64	0.07	0.22	ND	408.2	0.41	53.7	ND	0.017	25.0
66X-1, 81	299.21	0.07	0.22	ND	408.2	0.41	53.7	ND	0.024	24.1
66X-1, 103	299.43	0.06	0.20	ND	420.5	0.38	52.6	ND	0.022	23.1
67X-CC, 9	308.09	0.04	0.14	ND	407.4	0.60	23.3	ND	0.013	25.0
68X-1, 65	318.25	0.05	0.19	ND	414.8	0.88	21.6	ND	0.013	25.0
68X-CC, 26	318.90	0.06	0.18	ND	419.1	0.36	50.0	ND	0.020	25.0
69X-1, 28	327.48	0.06	0.18	ND	395.3	0.34	52.9	ND	0.020	25.0
70X-CC, 15	336.95	0.05	0.14	ND	402.0	0.25	56.0	ND	0.016	26.3
71X-1, 39	346.39	0.06	0.18	ND	ND	0.41	43.9	ND	0.020	25.0
72X-CC, 25	355.85	0.03	0.11	0.25	412.9	0.45	24.4	55.6	0.012	21.4
73X-1, 47	365.67	0.05	0.13	ND	382.8	0.26	50.0	ND	0.015	27.8
75X-1, 43	384.83	0.05	0.14	ND	396.1	0.36	38.9	ND	0.016	26.3
75X-1, 61	385.01	0.04	0.12	ND	383.9	0.33	36.4	ND	0.013	25.0
78X-1, 35	413.55	0.04	0.15	ND	403.9	0.36	41.7	ND	0.013	25.0
78X-1, 50	413.70	0.06	0.17	ND	408.9	0.28	60.7	ND	0.019	26.1
86X-CC, 11	490.01	0.04	0.10	ND	408.2	0.42	23.8	ND	0.012	28.6
88X-1, 49	510.09	0.03	0.07	ND	407.8	0.28	25.0	ND	0.008	30.0
90X-CC, 12	528.66	0.04	0.09	ND	406.1	0.29	31.0	ND	0.011	30.8
91X-CC, 13	537.63	0.03	0.08	ND	401.3	0.33	24.2	ND	0.009	27.3
92X-CC, 0	547.10	0.02	0.08	ND	422.0	0.20	40.0	ND	0.008	20.0
93X-1, 22	556.82	0.03	0.09	ND	404.0	0.30	30.0	ND	0.010	25.0
94X-CC, 17	566.37	0.02	0.04	ND	369.5	0.20	20.0	ND	0.005	33.3
95X-1, 48	576.28	0.05	0.10	ND	398.2	0.27	37.0	ND	0.013	33.3
96X-1, 17	585.57	0.04	0.08	ND	396.5	0.19	42.1	ND	0.010	33.3
97X-CC, 13	595.13	0.04	0.10	ND	397.2	0.31	32.3	ND	0.012	28.6

Notes: T_{max} is the pyrolysis temperature at which the evolution rate of S₂ is at a maximum. TOC_{SRA} = total organic carbon from source rock analyzer pyrolysis. Pyrolysis carbon = [0.83 × (S₁ + S₂)/10], production index = [S₁/(S₁ + S₂)] × 100. ND = not determined.

Table T16. Composition of interstitial waters, Site U1353. (See table note.)

Core, section, interval (cm)	Depth CSF-A (m)	Salinity	pH	Alkalinity (mM)	Ion chromatograph data (mM)						Mg/Ca
					Cl ⁻	SO ₄ ²⁻	Mg ²⁺	Ca ²⁺	Na ⁺	K ⁺	
317-U1353A-											
1H-1, 120	1.20	3.4	7.34	3.18	564	28.2	54.0	10.7	485	11.0	5.04
1H-2, 140	2.90	3.4	7.35	4.57	562	27.5	53.9	10.3	484	11.0	5.25
1H-3, 140	4.40	3.4	7.87	5.06	552	27.2	52.9	10.3	476	10.9	5.14
2H-1, 120	6.70	3.4	7.46	6.54	538	25.7	51.1	10.0	464	10.6	5.14
2H-2, 140	8.40	3.4	7.58	ND	555	26.1	52.9	10.0	477	10.7	5.30
3H-1, 120	10.50	3.4	7.63	5.94	536	25.5	51.1	9.9	462	10.4	5.18
3H-2, 140	12.20	3.3	7.60	5.60	533	24.7	50.0	10.0	459	10.4	5.00
3H-3, 140	13.70	3.3	7.55	5.45	530	24.3	50.5	10.0	458	10.2	5.04
3H-4, 140	15.20	3.2	7.89	5.71	515	24.0	49.2	9.4	441	9.7	5.21
4H-1, 120	19.40	3.2	7.40	5.55	511	22.5	48.3	9.8	435	9.1	4.92
4H-2, 140	21.10	3.2	7.39	5.87	501	22.2	47.7	9.8	430	8.8	4.87
4H-3, 140	22.60	3.1	7.38	5.60	503	21.6	47.1	9.7	429	8.7	4.85
4H-4, 140	24.10	3.0	7.22	5.54	502	20.9	47.0	9.9	429	8.4	4.74
4H-5, 140	25.60	2.9	7.63	5.92	478	19.3	44.5	9.7	409	7.9	4.59
5H-1, 120	27.67	2.8	7.63	5.99	458	18.1	42.5	9.4	390	7.2	4.50
5H-2, 120	29.17	2.8	7.88	6.15	4568	17.8	42.1	9.5	389	7.2	4.45
5H-3, 107	30.34	2.8	7.79	5.91	474	18.4	44.3	9.9	406	7.4	4.49
5H-4, 117	31.61	ND	ND	ND	475	18.5	44.3	9.5	407	7.6	4.64
5H-5, 112	32.83	2.9	7.90	6.13	500	19.9	46.5	10.2	427	7.9	4.56
6H-1, 120	35.40	2.6	7.30	5.82	449	16.3	40.5	10.0	381	6.3	4.05
6H-2, 140	37.10	2.6	7.44	5.64	449	16.7	40.2	9.9	383	6.4	4.07
6H-3, 140	38.60	2.4	7.24	6.06	432	15.7	39.3	9.8	368	5.9	4.01
6H-4, 140	40.10	2.6	7.36	5.99	427	15.8	38.6	9.7	363	5.5	3.98
6H-5, 87	41.07	2.4	7.25	5.98	420	15.5	38.1	9.6	358	5.3	3.97
7H-1, 120	42.40	2.4	7.19	5.84	430	15.7	38.7	9.8	366	5.7	3.95
7H-2, 140	44.10	2.5	7.29	5.95	420	15.5	37.8	9.6	358	5.4	3.96
7H-3, 140	45.60	2.5	7.42	5.64	415	15.7	37.6	9.3	357	5.5	4.05
7H-4, 140	47.10	2.4	7.32	5.86	413	15.7	37.1	9.3	353	5.3	3.98
7H-5, 80	48.00	2.4	7.32	5.87	415	16.0	37.3	9.4	355	5.1	3.96
8H-1, 104	49.24	2.5	7.49	5.81	424	16.5	38.1	9.6	363	5.3	3.98
8H-2, 140	50.94	2.5	7.34	5.89	399	15.6	35.8	9.0	344	5.1	3.98
8H-3, 140	52.44	2.4	7.21	6.28	409	16.6	36.5	9.3	357	5.1	3.93
8H-4, 140	53.94	2.4	7.53	6.33	399	16.3	35.0	9.0	345	4.8	3.89
8H-5, 95	54.99	2.5	7.30	6.27	400	16.7	35.7	9.1	347	4.7	3.91
8H-6, 53	55.62	2.4	7.30	6.06	404	16.9	35.3	9.0	349	4.8	3.92
317-U1353B-											
9H-2, 140	59.70	2.5	7.27	6.14	406	17.7	35.5	9.1	352	4.7	3.88
9H-3, 140	61.20	2.5	7.62	5.86	410	18.2	35.7	9.1	357	5.0	3.94
10H-1, 140	63.40	2.5	7.65	5.55	424	19.0	37.0	9.4	369	5.3	3.94
10H-3, 140	66.40	2.6	7.61	4.49	420	19.3	36.4	9.2	367	5.2	3.96
11H-1, 140	69.00	2.7	7.47	5.37	447	20.7	38.5	10.5	389	5.2	3.67
11H3, 140	72.00	2.7	7.64	4.07	437	20.1	37.1	10.0	383	5.3	3.71
19H-3, 140	114.58	3.1	7.71	2.32	512	24.0	42.4	13.6	446	5.1	3.13
23H-3, 140	134.60	3.2	7.99	1.94	524	24.0	42.3	14.2	455	4.8	2.98
28H-2, 120	152.10	3.3	7.72	2.34	548	24.9	43.5	15.2	476	4.6	2.86
34H-1, 140	178.40	3.4	7.19	2.29	545	24.4	43.3	15.7	474	4.5	2.76
37H-2, 135	189.68	3.4	7.37	2.44	542	23.7	43.0	15.6	467	4.6	2.76
38H-2, 140	192.95	3.4	7.34	2.41	544	23.9	43.2	15.7	470	4.6	2.76
40H-1, 143	197.83	3.4	7.56	2.47	552	24.3	43.9	15.8	477	4.7	2.78
45H-2, 140	219.00	3.4	7.51	2.16	553	24.4	44.0	15.9	478	4.5	2.77
57H-1, 100	252.60	3.4	7.67	2.14	576	25.1	45.0	16.7	499	4.3	2.69
65X-1, 106	289.86	3.4	7.52	2.11	571	24.6	44.8	16.5	495	5.2	2.71
68X-1, 94	318.54	3.4	7.64	2.32	557	24.4	44.0	16.5	482	5.4	2.68
96X-1, 39	585.79	3.8	7.85	2.49	635	21.2	42.7	18.0	554	5.7	2.38

Note: ND = not determined.

Table T17. Composition of interstitial waters, Site U1353. (See table notes.)

Core, section, interval (cm)	Depth CSF-A (m)	Spectrophotometry data			ICP-AES data							
		NH ₄ ⁺ (mM)	HPO ₄ ²⁻ (μM)	HSiO ₄ (μM)	Mn (μM)	Fe (μM)	B (mM)	Sr ²⁺ (mM)	Ba (μM)	Si (μM)	Li ⁺ (μM)	Sr/Ca*
317-U1353A-												
1H-1, 120	1.20	0.13	3.67	196	8.6	22.3	0.41	0.087	0.13	370	24	0.008
1H-2, 140	2.90	0.28	4.57	283	5.1	16.5	0.42	0.087	0.25	346	26	0.009
1H-3, 140	4.40	0.31	5.68	396	17.4	38.6	0.43	0.090	0.44	497	26	0.009
2H-1, 120	6.70	0.44	7.87	524	8.4	24.4	0.43	0.093	0.29	648	23	0.009
2H-2, 140	8.40	0.51	4.94	465	13.1	29.1	0.41	0.094	0.57	509	23	0.009
3H-1, 120	10.50	0.52	3.16	513	10.9	24.4	0.40	0.105	0.70	639	26	0.011
3H-2, 140	12.20	0.61	2.60	555	13.3	27.0	0.41	0.117	0.88	622	27	0.012
3H-3, 140	13.70	0.67	2.61	442	16.3	34.4	0.39	0.132	0.93	566	28	0.013
3H-4, 140	15.20	0.67	1.32	300	4.5	12.2	0.37	0.138	1.08	314	29	0.015
4H-1, 120	19.40	0.83	2.20	468	8.4	18.0	0.37	0.160	1.23	502	29	0.016
4H-2, 140	21.10	0.96	2.39	479	8.5	20.0	0.39	0.188	1.24	523	30	0.019
4H-3, 140	22.60	1.02	2.49	476	9.4	22.4	0.37	0.194	1.25	529	30	0.020
4H-4, 140	24.10	0.82	2.29	442	9.0	21.6	0.38	0.219	1.45	551	31	0.022
4H-5, 140	25.60	1.04	1.02	450	7.5	17.2	0.37	0.221	1.33	456	30	0.023
5H-1, 120	27.67	1.01	1.29	362	8.5	20.3	0.36	0.245	1.16	457	32	0.026
5H-2, 120	29.17	1.21	1.11	315	13.2	27.7	0.35	0.234	1.01	383	32	0.025
5H-3, 107	30.34	1.11	2.36	320	8.4	17.8	0.34	0.240	1.00	396	31	0.024
5H-4, 117	31.61	ND	ND	ND	14.3	30.7	0.35	0.233	1.15	411	31	0.024
5H-5, 112	32.83	1.15	1.19	326	9.5	23.9	0.35	0.243	1.05	465	31	0.024
6H-1, 120	35.40	1.13	1.90	404	9.8	18.9	0.36	0.260	0.96	498	29	0.026
6H-2, 140	37.10	1.16	1.84	429	9.5	18.6	0.36	0.262	1.22	470	31	0.027
6H-3, 140	38.60	1.23	1.55	451	7.9	14.9	0.35	0.251	0.99	467	29	0.026
6H-4, 140	40.10	0.99	1.84	477	15.8	28.6	0.37	0.263	0.94	507	29	0.027
6H-5, 87	41.07	0.93	1.93	502	9.2	17.2	0.36	0.263	0.93	546	29	0.027
7H-1, 120	42.40	1.18	2.12	490	16.0	30.9	0.39	0.276	0.93	625	31	0.028
7H-2, 140	44.10	1.00	1.82	540	14.7	27.8	0.38	0.272	1.05	600	30	0.029
7H-3, 140	45.60	1.15	1.51	451	8.0	16.8	0.38	0.276	1.08	506	31	0.030
7H-4, 140	47.10	1.12	1.19	457	10.2	22.0	0.37	0.255	1.06	446	29	0.027
7H-5, 80	48.00	0.88	1.13	448	14.9	30.3	0.37	0.261	1.09	509	29	0.028
8H-1, 104	49.24	0.80	1.98	424	7.8	18.1	0.37	0.257	1.23	447	28	0.027
8H-2, 140	50.94	0.70	1.21	467	15.6	31.1	0.38	0.255	1.12	500	29	0.028
8H-3, 140	52.44	0.74	1.54	547	10.4	23.7	0.40	0.260	0.95	577	29	0.028
8H-4, 140	53.94	0.10	1.39	546	6.1	16.6	0.40	0.228	0.84	589	29	0.030
8H-5, 95	54.99	0.63	1.37	556	12.7	31.0	0.40	0.274	0.92	664	29	0.030
8H-6, 53	55.62	0.67	1.56	629	9.1	21.7	0.41	0.276	0.98	667	29	0.031
317-U1353B-												
9H-2, 140	59.70	0.60	0.89	604	7.0	16.7	0.40	0.278	0.90	623	29	0.030
9H-3, 140	61.20	0.63	0.74	529	9.7	22.3	0.41	0.283	0.97	541	29	0.031
10H-1, 140	63.40	0.54	0.79	523	10.4	24.2	0.42	0.290	1.31	603	31	0.031
10H-3, 140	66.40	0.60	0.60	508	6.9	17.5	0.40	0.270	1.24	525	29	0.029
11H-1, 140	69.00	0.58	0.82	578	16.2	34.8	0.42	0.292	0.99	661	29	0.028
11H3, 140	72.00	0.54	0.80	489	4.0	10.9	0.40	0.290	1.01	429	28	0.029
19H-3, 140	114.58	0.46	0.25	199	3.7	13.2	0.46	0.433	1.16	235	33	0.032
23H-3, 140	134.60	0.47	0.18	172	3.6	13.3	0.43	0.440	1.06	200	32	0.031
28H-2, 120	152.10	0.53	0.17	182	3.8	14.2	0.51	0.436	1.24	202	34	0.029
34H-1, 140	178.40	0.41	0.10	205	4.2	21.8	0.51	0.410	1.15	239	41	0.026
37H-2, 135	189.68	0.43	0.08	137	5.7	14.6	0.50	0.340	1.50	186	43	0.022
38H-2, 140	192.95	0.46	0.08	145	6.6	16.6	0.52	0.353	1.48	223	44	0.023
40H-1, 143	197.83	0.45	0.12	141	5.1	14.8	0.51	0.333	1.26	199	46	0.021
45H-2, 140	219.00	0.45	0.14	188	4.4	14.6	0.55	0.313	1.24	240	49	0.020
57H-1, 100	252.60	ND	0.13	151	4.5	14.9	0.60	0.317	1.58	195	56	0.019
65X-1, 106	289.86	0.64	0.10	152	9.1	17.3	0.58	0.279	3.03	214	74	0.017
68X-1, 94	318.54	0.54	0.11	144	8.0	17.4	0.55	0.260	2.97	205	79	0.016
96X-1, 39	585.79	ND	0.19	129	7.9	16.7	0.61	0.535	4.02	207	113	0.030

Notes: * = Ca²⁺ data from ion chromatography (see Table T16). ICP-AES = inductively coupled plasma-atomic emission spectroscopy. ND = not determined. Mn and Fe concentrations may have been affected by oxidation prior to analysis, as these are redox-sensitive trace elements.

Table T18. Composition of interstitial waters normalized to chlorinity, Site U1353. (See table notes.)

Core, section, interval (cm)	Depth CSF-A (m)	Alkalinity (mM)	Ion chromatograph data (mM)		
			SO ₄ ²⁻	Mg ²⁺	Ca ²⁺
317-U1353A-					
1H-1, 120	1.20	3.18	28.2	54.0	10.7
1H-2, 140	2.90	4.58	27.5	54.0	10.3
1H-3, 140	4.40	5.18	27.8	54.0	10.5
2H-1, 120	6.70	6.86	27.0	53.6	10.4
2H-2, 140	8.40	ND	26.5	53.8	10.2
3H-1, 120	10.50	6.26	26.8	53.8	10.4
3H-2, 140	12.20	5.94	26.2	52.9	10.6
3H-3, 140	13.70	5.80	25.9	53.7	10.7
3H-4, 140	15.20	6.25	26.3	53.9	10.3
4H-1, 120	19.40	6.13	24.8	53.3	10.8
4H-2, 140	21.10	6.61	25.0	53.7	11.0
4H-3, 140	22.60	6.28	24.2	52.8	10.9
4H-4, 140	24.10	6.23	23.5	52.9	11.2
4H-5, 140	25.60	6.99	22.8	52.5	11.4
5H-1, 120	27.67	7.39	22.4	52.4	11.6
5H-2, 120	29.17	7.60	22.0	52.1	11.7
5H-3, 107	30.34	7.04	22.0	52.8	11.7
5H-4, 117	31.61	ND	21.9	52.6	11.3
5H-5, 112	32.83	6.91	22.4	52.4	11.5
6H-1, 120	35.40	7.31	20.5	50.8	12.6
6H-2, 140	37.10	7.08	21.0	50.5	12.4
6H-3, 140	38.60	7.91	20.5	51.3	12.8
6H-4, 140	40.10	7.92	20.9	51.0	12.8
6H-5, 87	41.07	8.02	20.8	51.1	12.9
7H-1, 120	42.40	7.65	20.6	50.7	12.9
7H-2, 140	44.10	7.99	20.8	50.8	12.8
7H-3, 140	45.60	7.67	21.3	51.0	12.6
7H-4, 140	47.10	8.01	21.4	50.7	12.7
7H-5, 80	48.00	7.99	21.7	50.7	12.8
8H-1, 104	49.24	7.74	22.0	50.7	12.7
8H-2, 140	50.94	8.33	22.1	50.6	12.7
8H-3, 140	52.44	8.65	22.8	50.4	12.8
8H-4, 140	53.94	8.96	23.1	49.5	12.7
8H-5, 95	54.99	8.84	23.6	50.3	12.9
8H-6, 53	55.62	8.47	23.6	49.3	12.6
317-U1353B-					
9H-2, 140	59.70	8.52	24.5	49.3	12.7
9H-3, 140	61.20	8.07	25.0	49.1	12.5
10H-1, 140	63.40	7.38	25.3	49.1	12.5
10H-3, 140	66.40	6.03	25.9	48.9	12.3
11H-1, 140	69.00	6.77	26.1	48.5	13.2
11H3, 140	72.00	5.25	25.9	47.9	12.9
19H-3, 140	114.58	2.56	26.5	46.8	15.0
23H-3, 140	134.60	2.09	25.9	45.5	15.3
28H-2, 120	152.10	2.41	25.6	44.8	15.7
34H-1, 140	178.40	2.37	25.3	44.8	16.3
37H-2, 135	189.68	2.53	24.7	44.8	16.2
38H-2, 140	192.95	2.51	24.8	44.9	16.3
40H-1, 143	197.83	2.52	24.8	44.9	16.2
45H-2, 140	219.00	2.21	24.9	44.8	16.2
57H-1, 100	252.60	2.10	24.6	44.1	16.4
65X-1, 106	289.86	2.09	24.3	44.3	16.3
68X-1, 94	318.54	2.35	24.7	44.6	16.7
96X-1, 39	585.79	2.22	18.8	37.9	15.9

Notes: Chlorinity-normalized data (mM) were calculated by multiplying original data (Table T16) at depth *x* with [564/chloride (mM) at depth *x*]. ND = not determined.

Table T19. Degree of sediment sample contamination (particulate tracer), Site U1353. (See table note.)

Core, section	Depth CSF-A (m)	Microsphere count (beads/cm ³ sediment)		Delivery confirmed
		Inner	Outer	
317-U1353A-				
1H-1	0.8	0	4,018	Yes
2H-1	6.3	4,179	3,656,380	Yes
3H-1	10.1	4,339	38,573	Yes
4H-1	19.0	482	12,054	Yes
5H-1	27.27	482	16,072	Yes
6H-1	35.0	5,786	75,538	Yes
7H-1	42.0	0	30,537	Yes
8H-1	48.84	0	85,985	Yes

Note: Inner = center part of core, outer = part of core in contact with core liner.

Table T20. Temperature data, Site U1353. (See table notes.)

Core	Tool	Depth CSF-A (m)	Temperature (°C)	t_i (s)	t_f (s)	$t_f - t_i$ (s)	Reliability
317-U1353A-5H	APCT-3	34.2	11.9	78	402	324	Poor

Notes: Times t_i and t_f are the initial and final times of the interval, respectively, picked to estimate asymptotic temperature for each data set. Estimated temperatures are considered reliable when the picked interval, $t_f - t_i$, is >300 s. APCT-3 = third-generation advanced piston corer temperature tool. Measurement depth is the bottom of the cored interval.

Table T21. Thermal conductivity data, Site U1353. (See table notes.)

Hole	Measurement (N)		Depth CSF-A (m)		Lab-measured thermal conductivity [†] (harmonic mean/range; W/[m·K])	
	Good*	Total	Good*	Total	Hole	Site
317-						
U1353A	7	21	7.7–31.1	0.4–53.2	1.414/1.275–1.771	1.546/1.122–1.840
U1353B	39	75	5.2–413.5	0.7–585.5	1.549/1.122–1.840	

Notes: * = thermal conductivity data were discarded when (1) contact between the probe and sediment was poor, (2) thermal conductivity was close to that of water (0.6 W/[m·K]) because of sediment dilution during coring, or (3) measurements were taken in caved-in layers such as shell hash. † = good measurements.

Table T22. Cumulative depth adjustments, Site U1353.

Core	Cumulative depth adjustment (m)
317-U1353A-	
1H	0
2H	0
3H	0
4H	0.53
5H	0.53
6H	1.88
7H	1.88
8H	1.88
317-U1353B-	
1H	0
2H	0.98
3H	0.98
4H	0.98
5H	0.98
6H	0.98
7H	0.98
8H through 96X	2.18